NUMERICAL INVESTIGATION OF A FRACTURED RESERVOIR RESPONSE

TO INJECTION/EXTRACTION USING A FULLY COUPLED

DISPLACEMENT DISCONTINUITY METHOD

A Thesis

by

BYUNGTARK LEE

Numerical Investigation of a Fractured Reservoir Response to Injection/Extraction Using

a Fully Coupled Displacement Discontinuity Method

NUMERICAL INVESTIGATION OF A FRACTURED RESERVOIR RESPONSE

TO INJECTION/EXTRACTION USING A FULLY COUPLED

DISPLACEMENT DISCONTINUITY METHOD

A Thesis

by

BYUNGTARK LEE

Submitted to the Office of Graduate Studies of
Texas A&M University
in partial fulfillment of the requirements for the degree of

MASTER OF SCIENCE

Approved by:

Chair of Committee,	Ahmad Ghassemi
Committee Members,	Stephen A. Holditch
	Benchun Duan
Head of Department,	Stephen A. Holditch

August 2011

Major Subject: Petroleum Engineering

ABSTRACT

Numerical Investigation of Fractured Reservoir Response to Injection/Extraction Using a

Fully Coupled Displacement Discontinuity Method. (August 2011)

Byungtark Lee, B.S., Korea Aerospace University

Chair of Advisory Committee: Dr. Ahmad Ghassemi

In geothermal reservoirs and unconventional gas reservoirs with very low matrix permeability, fractures are the main routes of fluid flow and heat transport, so the fracture permeability change is important. In fact, reservoir development under this circumstance relies on generation and stimulation of a fracture network. This thesis presents numerical simulation of the response of a fractured rock to injection and extraction considering the role of poro-thermoelasticity and joint deformation. Fluid flow and heat transport in the fracture are treated using a finite difference method while the fracture and rock matrix deformation are determined using the displacement discontinuity method (DDM).

The fractures response to fluid injection and extraction is affected both by the induced stresses as well as by the initial far-field stress. The latter is accounted for using the non-equilibrium condition, i.e., relaxing the assumption that the rock joints are in equilibrium with the in-situ stress state.

The fully coupled DDM simulation has been used to carry out several case studies to model the fracture response under different injection/extractions, in-situ

stresses, joint geometries and properties, for both equilibrium and non-equilibrium conditions. The following observations are made: i) Fluid injection increases the pressure causing the joint to open. For non-isothermal injection, cooling increases the fracture aperture drastically by inducing tensile stresses. Higher fracture aperture means higher conductivity. ii) In a single fracture under constant anisotropic in-situ stress (non-equilibrium condition), permanent shear slip is encountered on all fracture segments when the shear strength is overcome by shear stress in response to fluid injection. With cooling operation, the fracture segments in the vicinity of the injection point are opened due to cooling-induced tensile stress and injection pressure, and all the fracture segments experience slip. iii) Fluid pressure in fractures increases in response to compression. The fluid compressibility and joint stiffness play a role. iv) When there are injection and extraction in fractured reservoirs, the cooler fluid flows through the fracture channels from the injection point to extraction well extracting heat from the warmer reservoir matrix. As the matrix cools, the resulting thermal stress increases the fracture apertures and thus increases the fracture conductivity. v) Injection decreases the amount of effective stress due to pressure increase in fracture and matrix near a well. In contrast, extraction increases the amount of effective stress due to pressure drop in fracture and matrix.

DEDICATION

To my family and friends in South Korea

ACKNOWLEDGEMENTS

TABLE OF CONTENTS

LIST OF FIGURES

Page

LIST OF TABLES

1. INTRODUCTION

A significant portion of worldwide petroleum and geothermal reservoirs are discovered in naturally fractured systems or low permeability reservoirs that need be fractured (Van Golf-Racht, 1982). The interest in behavior of fractured systems has increased in light of recent increase in petroleum production from unconventional reservoirs such as Marcellus, Haynesville and Bakken. From a geomechanical point of view, a fracture is a surface on which a loss of cohesion has occurred, creating a surface of rupture (Fig. 1.1). A fracture with relative displacement of its sides is called a fault, while a fracture in which no noticeable displacement has occurred can be defined as a joint (Van Golf-Racht, 1982). More generally, a fracture can be defined as a surface of discontinuity in displacements, where rock breaks into blocks along cracks, fissures, joints.

_____

This thesis follows the style of Geothermics.
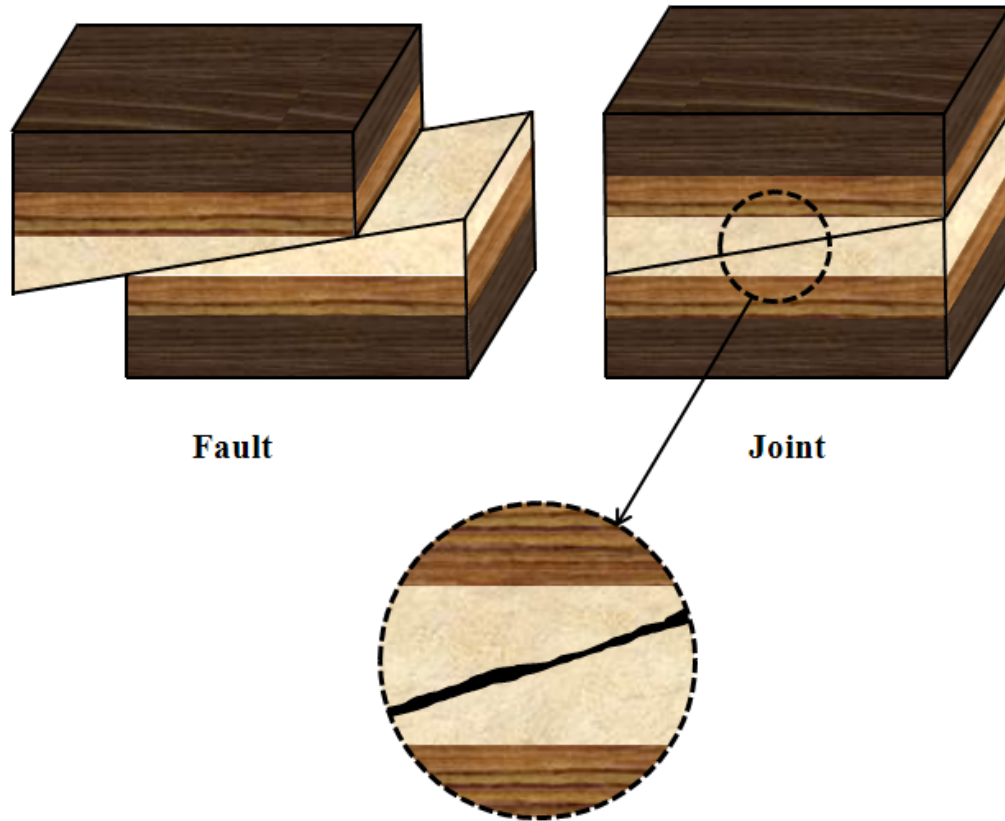
Fig. 1.1 An illustration of fault and joint (Van Golf-Racht, 1982).

Natural or man-made fractures are the main channel for reservoir fluid as they often have significantly higher porosity and permeability than the reservoir matrix. Fracture permeability is critical to the hydrocarbon production and effective geothermal reservoir development. This section starts with a brief introduction on the history of naturally fractured reservoir modeling and the numerical methods used. Then, the objectives of this research are described and a summary of thesis is presented.

1.1 Modeling of Naturally Fractured Reservoir

Modeling of naturally fracture reservoir to investigate the fracture aperture, stress change, flow channel and other related factors has been the subject of research for long time. Warren and Root (1963) introduced a model with dual-porosity to illustrate naturally fractured reservoirs (Fig. 1.2). The reservoir is simplified as a homogeneous system with rigid fractures and matrix. Both the matrix and the fractures were assigned porosity and permeability. Pseudo steady state flow was assumed in the matrix, as well as for flow between matrix and the fractures.
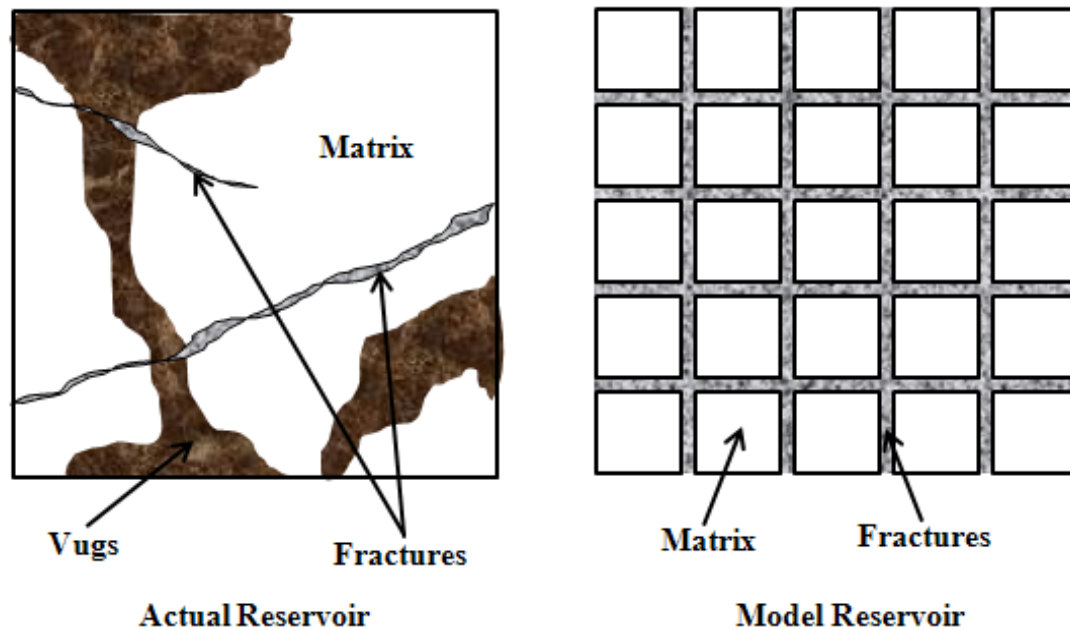
Fig. 1.2 An actual reservoir and model reservoir with matrix and fracture in two-dimensional (unit height, 1m).

However, the fractures and matrix do deform when the effective stress is increased by production or decreased by injection.

Goodman (1976) and Bandis et al. (1981, 1983) investigated the fracture aperture and permeability change by stress change through laboratory experiments. Generally, in a naturally fractured reservoir, fractures are more dependent on stress and pressure change than the matrix as the fractures are more deformable than the matrix. Fracture deformation pattern between normal and shear deformation is different. According to Bandis et al. (1983), the closure of joints varies non-linearly (hyperbolic behavior) with normal stress change while the shear deformation of joints shows an almost linear behavior before yielding and shows complicated (unpredictable) behavior after yielding.

Considering an elastic impermeable porous medium, Crouch and Starfield (1983) developed the elastic displacement discontinuity method (DDM) to models the interactions not only between fractures but also the influence caused by fracture deformation. DDM is one of boundary element methods which can be used to solve time dependent boundary value problems such as dynamic elasticity. Asgian (1988, 1989) used the elastic DDM to study the fracture aperture changes in a naturally fractured reservoir subjected to isothermal injection (Fig. 1.3).
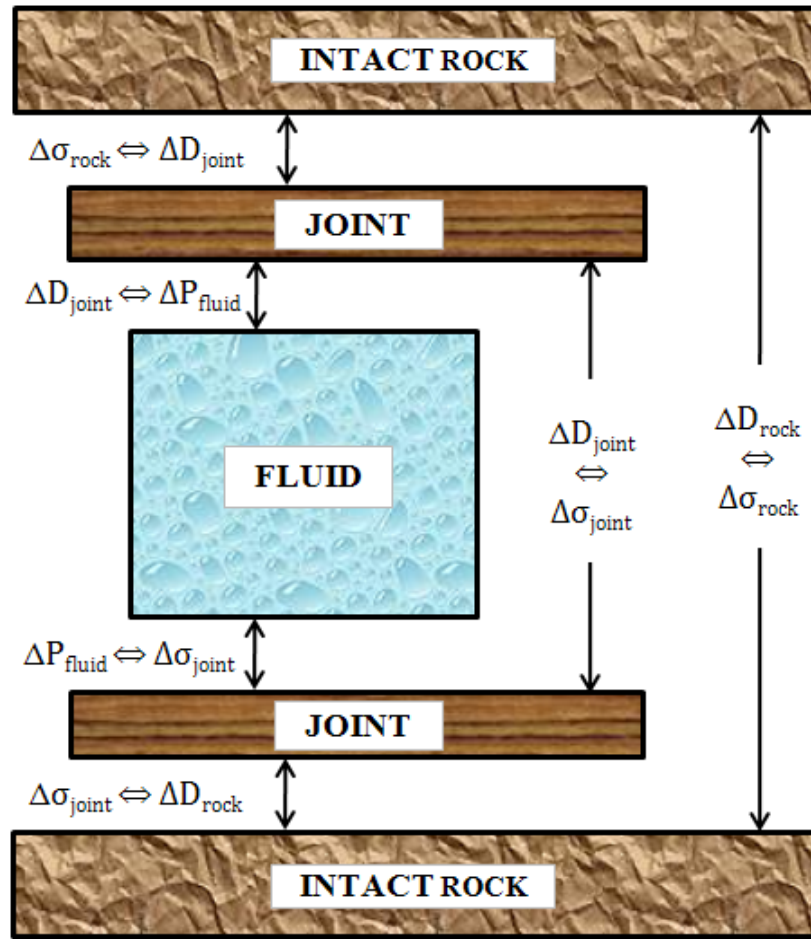
Fig. 1.3 Fluid-rock interactions in a deformable naturally fractured reservoir, $\Delta\sigma$, Δp, ΔD denote change in stress, pressure and deformation (Asgian, 1988, 1989).

Generally, the fractured reservoirs, there is communication between the fractures and the matrix, including fluid and heat as well as chemical species. Biot (1941) introduced the theory of poroelasticity to consider the interactions between fluid diffusion and rock deformation in the elastic regime. Rice and Cleary (1976) further developed the theory of poroelasticity by expressing it material parameters in more explicit form.

The DDM also has been extended to poroelasticity by Curran and Carvalho (1987) and also applied to fracture and wellbore problems (Carvalho, 1990).

The poroelastic DDM was then used by Tao (2010) and Tao et al. (2011) to investigate production and well testing in fractured reservoirs. The model fully coupled the fracture aperture change with stress and pore pressure in fractures and in matrix.
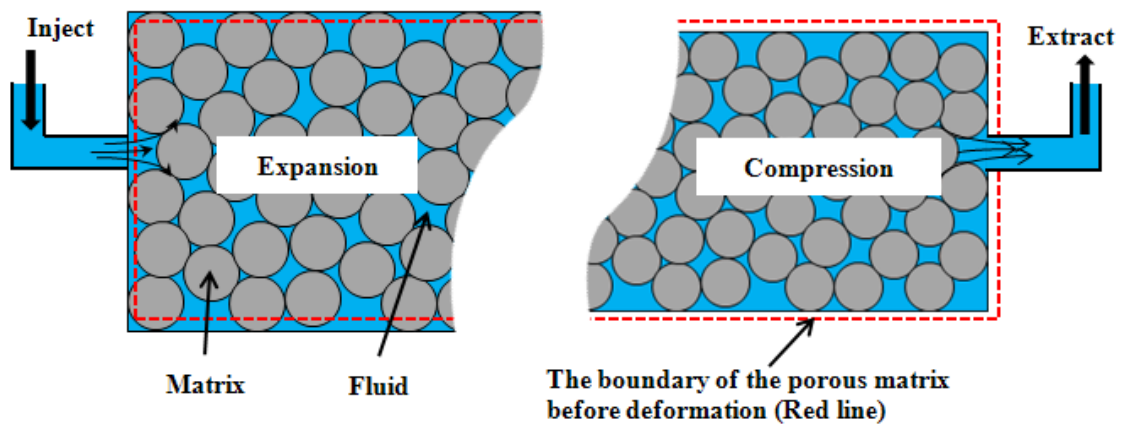
Fig. 1.4 Figure of the induced deformation of porous medium by the fluid flow in the interconnected pores in a porous matrix (left) and figure of the induced pore pressure change by compression of a continuum porous matrix and fluid flow in the interconnected pores (right) (Tao, 2010).

According to Fig. 1.4, there is a matrix deformation caused by fluid diffusion and an induced fluid flow caused by porous medium deformation. So, if there were natural fracture in reservoir, the fracture aperture would change by expansion and compression related to injection and/or production.

Also, a three-dimensional DD-based numerical model for poroelasticity has been developed to simulate the fluid injection/extraction process and investigate fracture aperture changes by Zhou and Ghassemi (2011).

McTigue (1986) introduce the theory of poro-thermoelasticity to consider thermoelastic response of fluid-saturated porous rock. This theory contains thermal expansion of the fluid and also solid constituents and fluid compressibility. According to McTigue, in certain cases, convective heat transfer can be neglected and the temperature can be independently determined. In the context of DDM, this means that the thermal source term can be substituted in the pore pressure and stress equation as a known value. This procedure is specified in Section 2.6.3.

Ghassemi and Zhang (2006) developed the transient poro-thermoelastic DDM. They examined the fracture response in poro-thermoelastic reservoir caused by stress, pressure and temperature changes. It was shown that the thermal effect causes pore pressure variations and connect between thermal and poro-mechanical processes. Also, the cooling of the fracture surfaces increases the fracture aperture drastically due to the temperature change and thermal and elastic rock properties. This DD formulation was used by Tao and Ghassemi (2010) to develop a poro-thermoelastic model for fluid flow and heat transport in fractured reservoirs. However, the fracture shear slip was not considered and the fracture system was assumed to be in equilibrium with the initial in-situ stress field.

In naturally fractured reservoirs, the fracture aperture are changed by shear slip and opening, which in turns influences fluid and heat flow. Therefore, investigating the fracture network response is directly related to effective design of an enhanced geothermal system (EGS) and its efficient operation.

1.2 Objective of Research

The objectives of the research are:

- To study the theory of poro-thermoelsticity and understand the fully coupled poro-thermoelastic displacement discontinuity method (DDM) with fluid and heat transport in naturally fracture

- To develop a joint model for the fully coupled DDM under non-equilibrium condition to investigate permanent shear slip caused by injection in anisotropic stress condition

- To observe the induced pressure, temperature and stress in field by fluid injection or production in isothermal or cooling case with simple, regular and irregular fracture network cases

- To investigate the fluid flow channels and temperature channels and distribution in irregular fracture network

- To compare the fracture pressure, fracture aperture and temperature results in both with far field stress (non-equilibrium) and without far field stress

1.3 Summary of Thesis

This thesis consists of six sections. Section 1 describes the objective of this research with introduction of previous development of modeling of naturally fractured reservoir. In addition, the development history of elasticity, poroelasticity and poro-thermoelasticity theory and the displacement discontinuity method (DDM) are reviewed.

Section 2 introduces the theory and derivation of equations used in this research. First, the elastic DDM in an infinite nonporous media which is developed by Crouch and Starfield (1983) is introduced. And this section introduces a brief derivation of equations of poroelasticity DDM which is developed by Biot (1941) and Carvalho (1990) in an infinite porous media and also introduce a brief derivation of poro-thermoelasticity DDM. After describing poro-thermoelastic DDM, the fluid transport equation and the heat transport equations are introduced (developed by Tao and Ghassemi, 2010). Also, Section 2.5 describes the concept of normal and shear fracture deformation. After completing the introduction, these equations are coupled and detail solving procedure are explained with the fully coupled poro-thermoelastic DDM.

Section 3 reviews the elastic joint and failure mode. An elastic joint is permanently deformed when the joint is fully opened or slipped. Mohr-Coulomb failure criterion is introduced for this purpose. Section 3.3 introduces the non-equilibrium condition which means that the in-situ stresses affects the joint initially. Especially, the far-field stresses play a key role to permit the permanent shear slip caused by injection which decreases the amount of effective stress in the fracture.

In Section 4, we generate the permanent shear slip caused by constant injection at the center of the fracture under non-equilibrium condition. And, using DD method, draw the field (matrix) distribution graphs of the induced pressure, temperature, normal and shear stress. Actually, under equilibrium condition, there is no significant shear displacement in a single fracture. So, the shear deformation mechanism in the simple fracture network cases will be investigated. In addition, at the beginning of this section,

an injecting well case is investigated to verify a fully coupled DDM comparing the results of pressure, temperature, tangential and radial stresses to analytical solution.

Section 5 contains the simulation in regular and irregular fracture network with injection and extraction under equilibrium and non-equilibrium conditions. Also in this section, the fluid flow channel and the flow mechanism in irregular fracture network will be investigated. In addition, using DD method, find the induced pressure, temperature and stress distribution graphs in field (matrix).

Finally, in Section 6, the thesis will be concluded with conclusion and future work. This research examines the results under restricted condition. The fluid is only one phase, water and the reservoir is two-dimensional. Therefore, several future studies will be recommended.

2. FULLY COUPLED DISPLACEMENT DISCONTINUITY METHOD

In this section, the derivation of the equations used in numerical simulation will be introduced briefly. First, the elastic displacement discontinuity method (DDM) is described, and then the major features of the poro-thermoelastic DDM are explained. Second, the heat transport and fluid transport equations are derived to illustrate the basic concept of flow in fractures. Third, joint deformation in shear and normal mode is described. And finally, the fully coupled DDM for heat transport, fluid transport and joint deformation equations as developed by Tao and Ghassemi (2010) are presented.

2.1 Overview of Elastic DDM

The elastic displacement discontinuity method (DDM) is mainly developed by Crouch and Starfield (1983) with applications in mining. In elastic DDM, it is assumed that the rock matrix is impermeable.
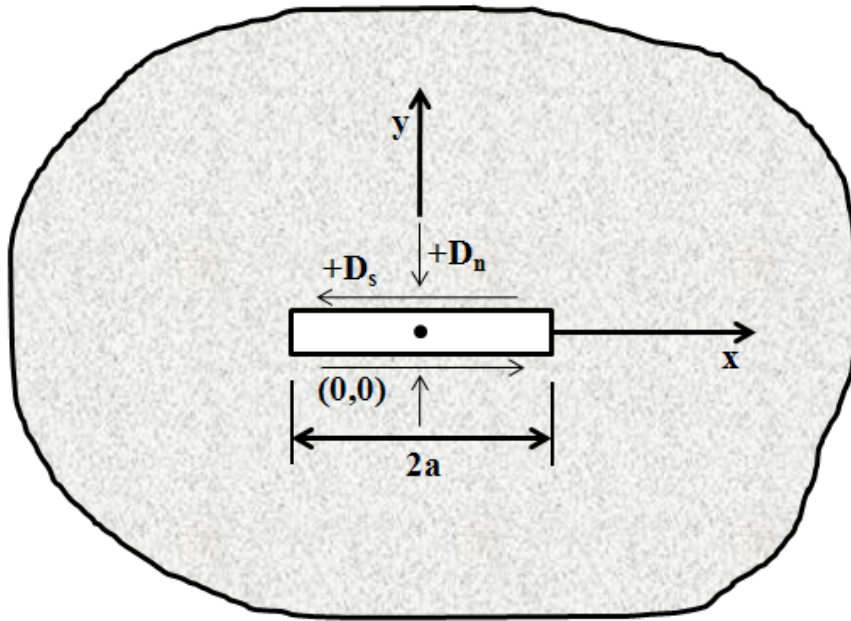
Fig. 2.1 A small thin fracture segment in a two-dimensional infinite nonporous medium (Crouch and Starfield, 1983).

The DD method is constructed by considering a line segment with its center at a point (x,y) (Fig. 2.1), that is located in an infinite two-dimensional isotropic and homogeneous elastic rock. The line segment represents a surface of displacement discontinuity or a finite thin fracture. Both x- and y-components of displacement can be discontinuous, representing shear and normal DD, respectively. By considering the center of the fracture to be located at (0,0), and the length of the fracture to be 2a. Crouch and Starfield (1983) developed equations for the stresses caused by the DD over the line segment. These equations (Eq. 2.1) are called fundamental solutions and provide expression for the induced stress (σ_{xx}, σ_{yy}, σ_{xy}) at a point (x,y) due to the normal displacement discontinuity (D_n) and the shear displacement discontinuity (D_s) with its center at the origin.

$$\sigma_{xx} = 2GD_n\left(\frac{\partial^2 F}{\partial y^2} + y\frac{\partial^3 F}{\partial y^3}\right) + 2GD_s\left(2\frac{\partial^2 F}{\partial x \partial y} + y\frac{\partial^3 F}{\partial x \partial y^2}\right)$$

$$\sigma_{yy} = 2GD_n\left(\frac{\partial^2 F}{\partial y^2} + y\frac{\partial^3 F}{\partial y^3}\right) - 2GD_s\, y\frac{\partial^3 F}{\partial x \partial y^2} \qquad\qquad \text{.......................} \qquad (2.1)$$

$$\sigma_{xy} = -2GD_n\, y\frac{\partial^3 F}{\partial x \partial y^2} + 2GD_s\left(\frac{\partial^2 F}{\partial y^2} + y\frac{\partial^3 F}{\partial y^3}\right)$$

G is the shear modulus of the rock, and F is the relative position function at the point (x,y) from center point $(0,0)$. And the function, F is described below.

$$F(x,y) = -\frac{1}{4\pi(1-\upsilon)}\left[y\left(\arctan\frac{y}{x-a} - \arctan\frac{y}{x+a}\right)\right.$$
$$\left. -(x-a)\ln\sqrt{(x-a)^2 + y^2} + (x+a)\ln\sqrt{(x+a)^2 + y^2}\right] \qquad \text{........................} \qquad (2.2)$$

υ is the Poisson's ratio, respectively.
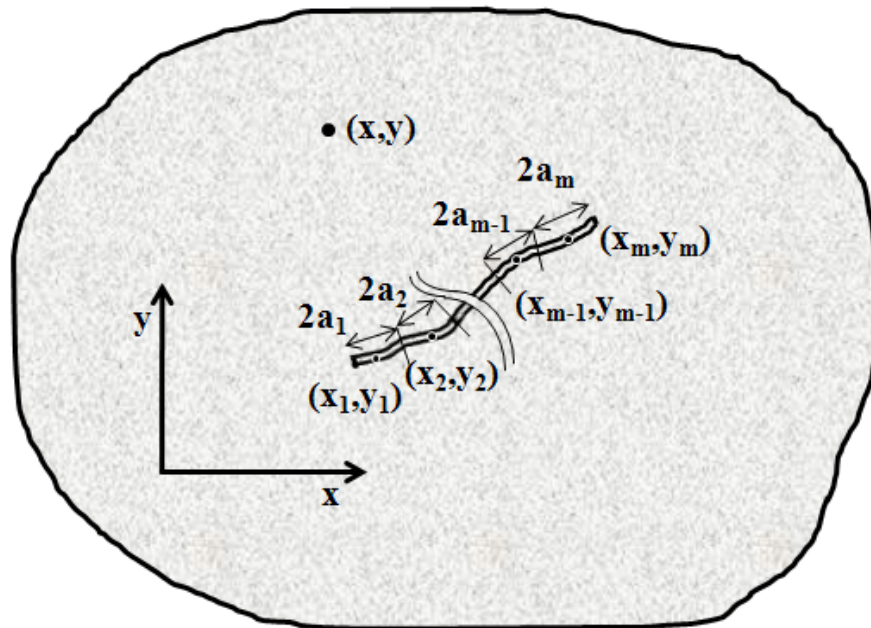
Fig. 2.2 A curvy fracture divided by m fracture segments in a two-dimensional infinite nonporous medium.

The DD is used to describe fractures of any shape. A curved fracture (Fig. 2.2), e.g., is divided into *m* straight fracture segments, and the effect of all segments are added to find the stresses caused by the entire crack at point (x,y). So, by superposition, the induced stress components are simply:

$$\sigma_{xx} = \sum_{j=1}^{m} \overset{j}{\sigma}_{xx}$$

$$\sigma_{yy} = \sum_{j=1}^{m} \overset{j}{\sigma}_{yy} \quad \text{...} \quad (2.3)$$

$$\sigma_{xy} = \sum_{j=1}^{m} \overset{j}{\sigma}_{xy}$$

If the arbitrary point of interest, (x,y), were located at the center point of the *ith* fracture segment, the induced stresses on the *ith* fracture segment caused by the *jth* fracture segment are described by $\overset{ij}{A}$, $\overset{ij}{B}$, $\overset{ij}{E}$ and $\overset{ij}{F}$ and:

$$\overset{ij}{\sigma}_n = \overset{ij}{A}\overset{j}{D}_n + \overset{ij}{B}\overset{j}{D}_s$$

$$\overset{ij}{\sigma}_s = \overset{ij}{E}\overset{j}{D}_n + \overset{ij}{F}\overset{j}{D}_s \quad \text{..} \quad (2.4)$$

$$\overset{ij}{A} = 2G\left[\frac{\partial^2 \overline{F}}{\partial \overline{y}^2} + \left(\cos^2 \overset{ij}{\gamma} - \sin^2 \overset{ij}{\gamma}\right)\overline{y}\frac{\partial^3 \overline{F}}{\partial \overline{y}^3} - \sin 2\overset{ij}{\gamma}\,\overline{y}\frac{\partial^3 \overline{F}}{\partial \overline{x}\partial \overline{y}^2}\right]$$

$$\overset{ij}{B} = 2G\left[\cos^2 \overset{ij}{\gamma}\left(2\frac{\partial^2 \overline{F}}{\partial \overline{x}\partial \overline{y}} + \overline{y}\frac{\partial^3 \overline{F}}{\partial \overline{x}\partial \overline{y}^2}\right) - \sin^2 \overset{ij}{\gamma}\,\overline{y}\frac{\partial^3 \overline{F}}{\partial \overline{x}\partial \overline{y}^2} + \sin 2\overset{ij}{\gamma}\left(\frac{\partial^2 \overline{F}}{\partial \overline{y}^2} + \overline{y}\frac{\partial^3 \overline{F}}{\partial \overline{y}^3}\right)\right]$$

$$\overset{ij}{E} = 2G\overline{y}\left[\sin 2\overset{ij}{\gamma}\frac{\partial^3 \overline{F}}{\partial \overline{y}^3} + \left(\cos^2 \overset{ij}{\gamma} - \sin^2 \overset{ij}{\gamma}\right)\frac{\partial^3 \overline{F}}{\partial \overline{x}\partial \overline{y}^2}\right]$$

$$\overset{ij}{F} = 2G\left[\sin 2\overset{ij}{\gamma}\left(\frac{\partial^2 \overline{F}}{\partial \overline{x}\partial \overline{y}} + \overline{y}\frac{\partial^3 \overline{F}}{\partial \overline{x}\partial \overline{y}^2}\right) - \left(\cos^2 \overset{ij}{\gamma} - \sin^2 \overset{ij}{\gamma}\right)\left(\frac{\partial^2 \overline{F}}{\partial \overline{y}^2} + \overline{y}\frac{\partial^3 \overline{F}}{\partial \overline{y}^3}\right)\right]$$

$$\text{...} \quad (2.5)$$

$\overset{ij}{\sigma}_n$ and $\overset{ij}{\sigma}_s$ are the induced normal and shear stresses (on the *i*th segment caused

by the *jth* segment). $\overset{ij}{\gamma} = \dfrac{\pi}{2} + \beta_i - \beta_j$ and β denotes the angle (counter clockwise) of

the fracture segments from the *x-axis*. And upper bar above *x, y* and the position function

$\overline{F}$ means the local co-ordinate system of the influenced element.

So, for the curvy fracture which is divided into *m* constant DD segments, the

superposition of the influence of *m* DD segments for the normal and shear stress are:

$$\overset{i}{\sigma}_n = \sum_{j=1}^{m} \overset{ij}{A} \overset{j}{D_n} + \sum_{j=1}^{m} \overset{ij}{B} \overset{j}{D_s}$$

$$\overset{i}{\sigma}_s = \sum_{j=1}^{m} \overset{ij}{E} \overset{j}{D_n} + \sum_{j=1}^{m} \overset{ij}{F} \overset{j}{D_s} \quad \text{..} \quad (2.6)$$

So, if there were 4 fractures in the medium, the matrix form of the expression

relating DD's and to normal and shear stress vectors on the elements is:

$$
\begin{pmatrix}
A^{11} & B^{11} & A^{12} & B^{12} & A^{13} & B^{13} & A^{14} & B^{14} \\
E^{11} & F^{11} & E^{12} & F^{12} & E^{13} & F^{13} & E^{14} & F^{14} \\
A^{21} & B^{21} & A^{22} & B^{22} & A^{23} & B^{23} & A^{24} & B^{24} \\
E^{21} & F^{21} & E^{22} & F^{22} & E^{23} & F^{23} & E^{24} & F^{24} \\
A^{31} & B^{31} & A^{32} & B^{32} & A^{33} & B^{33} & A^{34} & B^{34} \\
E^{31} & F^{31} & E^{32} & F^{32} & E^{33} & F^{33} & E^{34} & F^{34} \\
A^{41} & B^{41} & A^{42} & B^{42} & A^{43} & B^{43} & A^{44} & B^{44} \\
E^{41} & F^{41} & E^{42} & F^{42} & E^{43} & F^{43} & E^{44} & F^{44}
\end{pmatrix}
\times
\begin{pmatrix}
D_n^{1} \\ D_s^{1} \\ D_n^{2} \\ D_s^{2} \\ D_n^{3} \\ D_s^{3} \\ D_n^{4} \\ D_s^{4}
\end{pmatrix}
=
\begin{pmatrix}
\sigma_n^{1} \\ \sigma_s^{1} \\ \sigma_n^{2} \\ \sigma_s^{2} \\ \sigma_n^{3} \\ \sigma_s^{3} \\ \sigma_n^{4} \\ \sigma_s^{4}
\end{pmatrix}
\quad \text{.................................} \quad (2.7)
$$

If the values of the DDs are known, Eq. (2.7) can be used to the normal and shear

discontinuity, D_n and D_s. In the following section, we review the poro-thermoelastic

DDM.

2.2 DD in Poro-thermoelasticity

The elastic DD was extended to poroelasticity by Curran and Carvalho (1987) within the framework of Biot's theory. Using the linear theory of poro-thermoelasticity (McTigue, 1986), Ghassemi and Zhang (2006) developed the poro-thermoelastic DDM which is used recently for developing the fully coupled poro-thermoelastic DD by Tao and Ghassemi (2010) (Fig. 2.3).
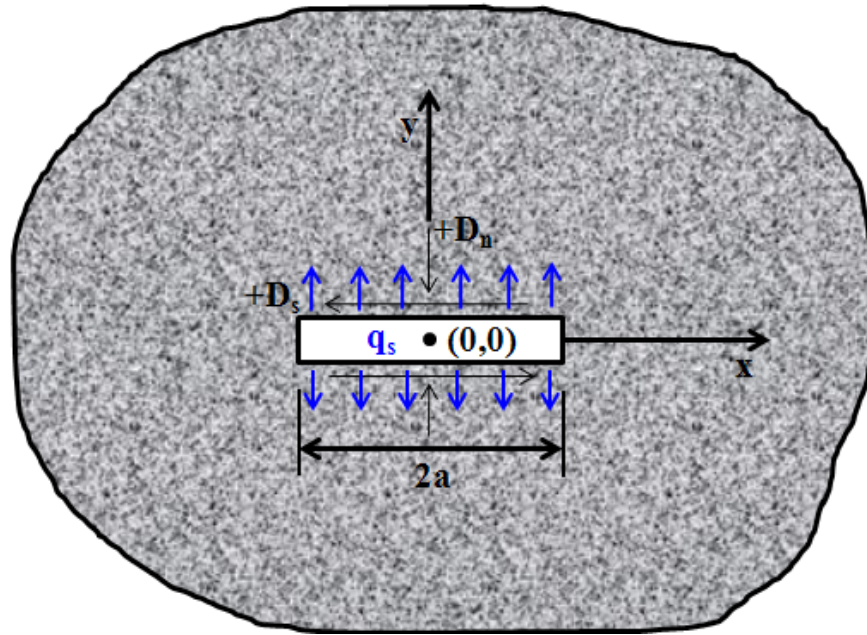
Fig. 2.3 A small thin fracture segment in a two-dimensional infinite porous medium.

Biot (1941) theory of poroelasticity explains the relation of stress to strain and pore pressure in an isotropic poroelastic medium:

$$\sigma_{ij} = 2G\left[e_{ij} + \delta_{ij} \frac{\upsilon}{1-2\upsilon} e_{kk} \right] - \delta_{ij}\alpha p \quad \text{...} \quad (2.8)$$

e is the strain, e_{kk} is the volumetric strain and δ_{ij} is the Kronecker delta.

When rewriting this equation for strains:

$$\varepsilon_{ij} = \frac{1}{2G}\left[\sigma_{ij} - \frac{\upsilon}{1+\upsilon}\sigma_{kk}\delta_{ij}\right] + \frac{\alpha(1-2\upsilon)}{2G(1+\upsilon)}\delta_{ij}\,p \quad\text{..}\quad (2.9)$$

ε_{ij} is change of strain of the rock, σ_{ij} is the change of stress of the rock, p, T and ζ are the change of pore pressure, temperature, and increment of fluid content, respectively. α is Biot's coefficient, υ and υ_u are the drained and undrained Poisson's ratios, G is the bulk shear modulus.

According to Eq. (2.9), only a pore pressure term needs be added to the elastic equation, Eq. (2.1). Carvalho (1990) developed the following equations for the induced normal and shear stresses and pore pressure on the *ith* fracture segment caused by a constant fluid injection, normal and shear displacement discontinuities of *m* constant DD segments (A curvy fracture is divided *m* segments).

$$\overset{i}{\sigma_n} = \sum_{j=1}^{m}\overset{ij}{A}\overset{j}{D_n} + \sum_{j=1}^{m}\overset{ij}{B}\overset{j}{D_s} + \sum_{j=1}^{m}\overset{ij}{C}\overset{j}{q}_{\text{int}}$$

$$\overset{i}{\sigma_s} = \sum_{j=1}^{m}\overset{ij}{E}\overset{j}{D_n} + \sum_{j=1}^{m}\overset{ij}{F}\overset{j}{D_s} + \sum_{j=1}^{m}\overset{ij}{K}\overset{j}{q}_{\text{int}} \quad\text{...}\quad (2.10)$$

$$\overset{i}{p} = \sum_{j=1}^{m}\overset{ij}{L}\overset{j}{D_n} + \sum_{j=1}^{m}\overset{ij}{H}\overset{j}{D_s} + \sum_{j=1}^{m}\overset{ij}{M}\overset{j}{q}_{\text{int}}$$

$\overset{ij}{A}$, $\overset{ij}{B}$, $\overset{ij}{C}$, $\overset{ij}{E}$, $\overset{ij}{F}$, $\overset{ij}{K}$, $\overset{ij}{L}$, $\overset{ij}{H}$ and $\overset{ij}{M}$ denote the *jth* DD element influence coefficients on the *ith* DD segment. So, the induced normal and shear stresses, and pore pressure as time (*t*).

$$\Delta \overset{i}{\sigma}_n(t) = \sum_{j=1}^{m} \overset{ij}{\sigma}_n^{dn}(t) \Delta \overset{j}{D}_n + \sum_{j=1}^{m} \overset{ij}{\sigma}_n^{ds}(t) \Delta \overset{j}{D}_s + \sum_{j=1}^{m} \overset{ij}{\sigma}_n^{q}(t) \Delta \overset{j}{q}_{\text{int}}$$

$$\Delta \overset{i}{\sigma}_s(t) = \sum_{j=1}^{m} \overset{ij}{\sigma}_s^{dn}(t) \Delta \overset{j}{D}_n + \sum_{j=1}^{m} \overset{ij}{\sigma}_s^{ds}(t) \Delta \overset{j}{D}_s + \sum_{j=1}^{m} \overset{ij}{\sigma}_s^{q}(t) \Delta \overset{j}{q}_{\text{int}} \quad \text{.................. (2.11)}$$

$$\Delta \overset{i}{p}(t) = \sum_{j=1}^{m} \overset{ij}{p}^{dn}(t) \Delta \overset{j}{D}_n + \sum_{j=1}^{m} \overset{ij}{p}^{ds}(t) \Delta \overset{j}{D}_s + \sum_{j=1}^{m} \overset{ij}{p}^{q}(t) \Delta \overset{j}{q}_{\text{int}}$$

$$\overset{ij}{\sigma}_n^{dn}(t) \; , \; \overset{ij}{\sigma}_n^{ds}(t) \; , \; \overset{ij}{\sigma}_n^{q}(t) \; , \; \overset{ij}{\sigma}_s^{dn}(t) \; , \; \overset{ij}{\sigma}_s^{ds}(t) \; , \; \overset{ij}{\sigma}_s^{q}(t) \; , \; \overset{ij}{p}^{dn}(t) \; , \; \overset{ij}{p}^{ds}(t) \; \text{and} \; \overset{ij}{p}^{q}(t)$$

denote the *jth* fracture element influence coefficients on the *ith* fracture segment at given time (*t*). In Eq. (2.11), these equations show the induced pore pressure, normal and shear stresses with time (*t*) dependent for poroelasticity without temperature effect.

For the poro-thermoelasticity, McTigue (1986) introduced the constitutive equations of the linear theory of poro-thermoelasticity.

$$\varepsilon_{ij} = \frac{1}{2G}\left[\sigma_{ij} - \frac{v}{1+v}\sigma_{kk}\delta_{ij} \right] + \frac{\alpha(1-2v)}{2G(1+v)}\delta_{ij}\,p + \frac{\alpha_s}{3}\delta_{ij}T \quad \text{.......................... (2.12)}$$

$$\zeta = \frac{\alpha(1-2v)}{2G(1+v)}\sigma_{kk} + \frac{\alpha^2(1-2v)^2(1+v_u)}{2G(1+v)(v_u-v)}\,p - \phi(\alpha_f - \alpha_s)T \quad \text{........................ (2.13)}$$

α_s and α_f are the volumetric thermal expansion coefficient of the solid and the pore fluid, respectively. Using this theory, Ghassemi and Zhang (2006) developed the poro-thermoelastic DDM considering a normal and shear deformation, fluid source (leakoff rate) and heat source (interface heat flow rate).

$$\Delta p(x, y, t) = p^{dn}(x, y, t)\,\Delta D_n + p^{ds}(x, y, t)\,\Delta D_s + p^{q}(x, y, t)\,\Delta q_{\text{int}}$$
$$+ p^{T}(x, y, t)\,\Delta q_{h-\text{int}}$$
$$\Delta\sigma_n(x, y, t) = \sigma_n^{dn}(x, y, t)\,\Delta D_n + \sigma_n^{ds}(x, y, t)\,\Delta D_s + \sigma_n^{q}(x, y, t)\,\Delta q_{\text{int}}$$
$$+ \sigma_n^{T}(x, y, t)\,\Delta q_{h-\text{int}} \qquad\qquad \text{...... (2.14)}$$
$$\Delta\sigma_s(x, y, t) = \sigma_s^{dn}(x, y, t)\,\Delta D_n + \sigma_s^{ds}(x, y, t)\,\Delta D_s + \sigma_s^{q}(x, y, t)\,\Delta q_{\text{int}}$$
$$+ \sigma_s^{T}(x, y, t)\,\Delta q_{h-\text{int}}$$

Using these equations, the pore pressure and stress caused by a normal and shear deformation (ΔD_n and ΔD_s), fluid leakoff rate (Δq_{int}) and heat flow rate (Δq_{h-int}), at a point (x,y) at time (t) will be obtained. Note that Δq_{int} and Δq_{h-int} are the fluid leakoff rate, and heat flux rate (between fracture and matrix) per fracture length each. And the superscript d_n is normal displacement discontinuity source, d_s is shear displacement discontinuity source, q is fluid source (injection or production) and T is heat source, respectively.

For the heat conductive case, heat source (Δq_{h-int}) is not dependent on the ΔD_n, ΔD_s and Δq_{int}, so that:

$$\Delta T(x, y, t) = T^{T}(x, y, t)\,\Delta q_{h-\text{int}} \qquad\qquad\qquad \text{(2.15)}$$

For the multiple (m) fracture segments on a curvy fracture,

$$\Delta \overset{i}{p}(t) = \sum_{j=1}^{m} \overset{ij}{p}^{dn}(t) \Delta \overset{j}{D}_n + \sum_{j=1}^{m} \overset{ij}{p}^{ds}(t) \Delta \overset{j}{D}_s + \sum_{j=1}^{m} \overset{ij}{p}^{q}(t) \Delta \overset{j}{q}_{int} + \sum_{j=1}^{m} \overset{ij}{p}^{T}(t) \Delta \overset{j}{q}_{h-int}$$

$$\Delta \overset{i}{\sigma}_n(t) = \sum_{j=1}^{m} \overset{ij}{\sigma}_n^{dn}(t) \Delta \overset{j}{D}_n + \sum_{j=1}^{m} \overset{ij}{\sigma}_n^{ds}(t) \Delta \overset{j}{D}_s + \sum_{j=1}^{m} \overset{ij}{\sigma}_n^{q}(t) \Delta \overset{j}{q}_{int} + \sum_{j=1}^{m} \overset{ij}{\sigma}_n^{T}(t) \Delta \overset{j}{q}_{h-int}$$

$$\Delta \overset{i}{\sigma}_s(t) = \sum_{j=1}^{m} \overset{ij}{\sigma}_s^{dn}(t) \Delta \overset{j}{D}_n + \sum_{j=1}^{m} \overset{ij}{\sigma}_s^{ds}(t) \Delta \overset{j}{D}_s + \sum_{j=1}^{m} \overset{ij}{\sigma}_s^{q}(t) \Delta q_{int} + \sum_{j=1}^{m} \overset{ij}{\sigma}_s^{T}(t) \Delta \overset{j}{q}_{h-int}$$

$$\Delta \overset{i}{T}(t) = \sum_{j=1}^{m} \overset{ij}{T}^{T}(t) \Delta \overset{j}{q}_{h-int}$$

.... (2.16)

$$\overset{ij}{p}^{dn}(t) \; , \; \overset{ij}{p}^{ds}(t) \; , \; \overset{ij}{p}^{q}(t) \; , \; \overset{ij}{p}^{T}(t) \; , \; \overset{ij}{\sigma}_n^{dn}(t) \; , \; \overset{ij}{\sigma}_n^{ds}(t) \; , \; \overset{ij}{\sigma}_n^{q}(t) \; , \; \overset{ij}{\sigma}_n^{T}(t) \; , \; \overset{ij}{\sigma}_s^{dn}(t) \; ,$$

$\overset{ij}{\sigma}_s^{ds}(t) \; , \overset{ij}{\sigma}_s^{q}(t), \; \overset{ij}{\sigma}_s^{T}(t)$ and $\;\overset{ij}{T}^{T}(t)$ denote the influence of the *jth* element (influence

coefficient) on the *ith* element at a given time (*t*). Eq. (2.16) is the poro-thermoelastic

DD equations, pressure, temperature, normal and shear stresses, in multiple fractures in

an infinite two-dimensional porous medium.

2.3 Fluid Transport in Fractured Porous Rock
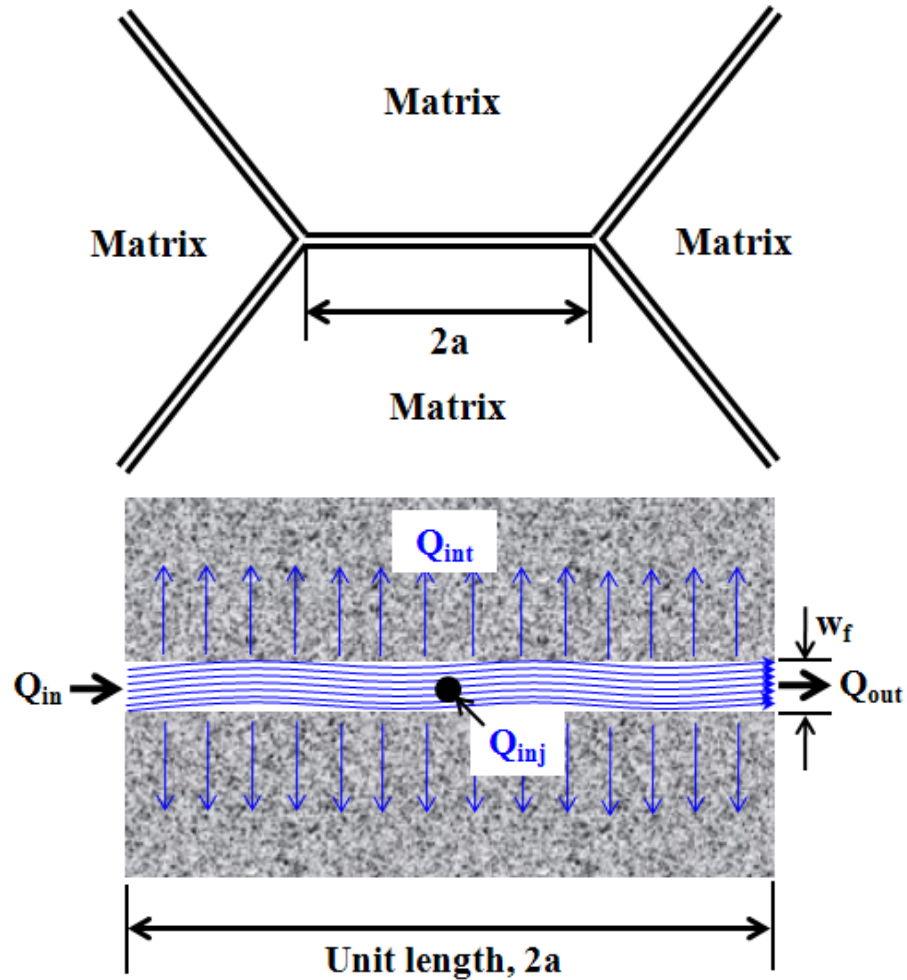
Fig. 2.4 Illustration of a single fracture segment in a fracture-matrix system and fluid flow in the fracture.

Mass balance equation can be used for fluid transport in fractured porous rock. General mass balance equation is shown below.

[Mass out flow rate] – [Mass in flow rate] = [Increase flow rate] .... (2.17)

The mass balance equation in fracture segment is (Tao and Ghassemi, 2010).

$$\left(\rho_f Q\right)_{out} - \left(\rho_f Q\right)_{in} - \rho_f v_{\text{int}} \Delta L \Delta h - \rho_f Q_{inj}^F = \frac{\partial\left(\rho_f w_f \Delta L \Delta h\right)}{\partial t} \quad \text{.............} \quad (2.18)$$

ρ_f is the density of the fluid, w_f is the fracture aperture, (ΔL = 2a) is the fracture length, Δh is the fracture height and v_{int} is the interface fluid. So, $\left(\rho_f Q\right)_{out}, \left(\rho_f Q\right)_{in}$ mean the flow in and out through fracture, $\rho_f v_{\text{int}} \Delta L \Delta h$ means the interface flow rate between fracture space and matrix. $\rho_f Q_{inj}^F$ means the injection flow rate and $\frac{\partial\left(\rho_f w_f \Delta L \Delta h\right)}{\partial t}$ means the increase rate of fluid mass in the fracture. Applying 2a as a length (Fig. 2.4) and unit height 1 m, get Eq. (2.18).

$$\left(\rho_f Q\right)_{out} - \left(\rho_f Q\right)_{in} - 2a\rho_f v_{\text{int}} - \rho_f Q_{inj}^F = \frac{\partial\left(2a\rho_f w_f\right)}{\partial t} \quad \text{.....................} \quad (2.19)$$

In reality, the fracture surface is usually very rough so the fracture aperture varies in every location. But using average aperture to simplify the fracture aperture, Darcy's law can be used for fluid flow in fracture (Witherspoon et al., 1980).

$$q_f = \frac{k_f w_f}{\mu} \frac{\partial p}{\partial x} \quad \text{...} \quad (2.20)$$

μ is the fluid viscosity and w_f fracture permeability (where, $k_f = w_f^2/12$). In this thesis, the fluid is compressible (consider fluid compressibility) and the density of the fluid is pressure dependent.

$$\frac{\partial \rho_f}{\partial p} = C_f \rho_f \quad \text{...} \quad (2.21)$$

C_f is the fluid compressibility. $\left(\rho_f Q\right)_{out} - \left(\rho_f Q\right)_{in}$ is rewritten to $\dfrac{\partial(\rho_f q_f)}{\partial x}$

(flow rate in fracture). So, substituting Eq. (2.20) to Eq. (2.21), a simplified relation is derived by neglecting the term that is multiplied by small compressibility (Lee et al., 2003).

$$\frac{\partial(\rho_f q_f)}{\partial x} = -\frac{\rho_f k_f w_f}{\mu} \frac{\partial^2 p}{\partial x^2} \quad\text{...} \quad (2.22)$$

The fracture volume changes with fracture aperture, so for a unit height, the fracture volume change is expressed below.

$$\frac{\partial V_f}{\partial x} = \Delta L \frac{\partial w_f}{\partial t} \quad\text{...} \quad (2.23)$$

And the fracture aperture is expressed by the fracture closure (D_n). So,

$$\frac{\partial w_f}{\partial t} = -\frac{\partial D_n}{\partial t} \quad\text{...} \quad (2.24)$$

Substituting Eq. (2.24) to Eq. (2.23), Eq. (2.25) is derived.

$$\frac{\partial V_f}{\partial x} = -\Delta L \frac{\partial D_n}{\partial t} \quad\text{...} \quad (2.25)$$

The mass of the fluid changes mainly due to density change, so get Eq. (2.26).

$$\frac{\partial m}{\partial t} = -w_f \Delta L \frac{\partial \rho_f}{\partial t} \quad\text{...} \quad (2.26)$$

And substituting Eq. (2.21) to Eq. (2.26).

$$\frac{\partial m}{\partial t} = -C_f \rho_f w_f \Delta L \frac{\partial p}{\partial t} \quad\text{...} \quad (2.27)$$

Finally, rearrange Eq. (2.19) by substituting Eq. (2.24), (2.25) and Eq. (2.27), the final fluid transport equation is constructed.

$$\frac{k_f w_f}{\mu} \nabla^2 p = 2aw_f c_f \frac{\partial p}{\partial t} - 2a \frac{\partial D_n}{\partial t} + 2aq_{\text{int}} + q_s \quad \text{.................................} \quad (2.28)$$

q_s is the injection and production and q_{int} is flow leakoff rate into matrix.

2.4 Heat Transport in Fractured Porous Rock
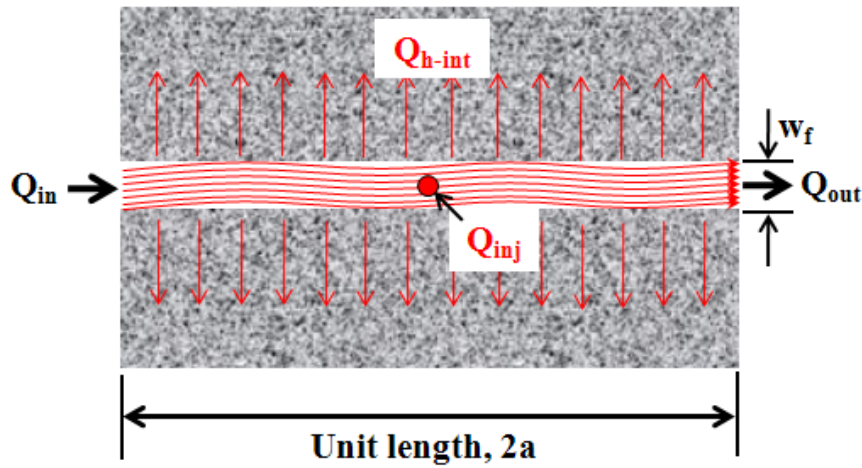
Fig. 2.5 Illustration of fluid flow in the fracture with heat transport.

The heat transport equation is derived using energy conservation and general energy conservation equation is introduced.

$$\Delta U = \Delta E_{conductive} + \Delta E_{convective} + Q_{h-\text{int}} \quad \text{...} \quad (2.29)$$

ΔU is the rate of internal energy, Q_{h-int} is the heat flow rate between fracture and matrix, $\Delta E_{conductive}$ and $\Delta E_{convective}$ are the energy change rate by conductive transport in fracture and convective transport within fracture. This thesis only considers that the temperature change effects the internal energy change because the internal energy

change caused by fracture aperture and fluid density variations are negligible (Fig. 2.5).

So, ΔU is simplified as:

$$\Delta U = 2a\,w_f\,\rho_w c_w \frac{\partial T}{\partial t}$$ .... (2.30)

w_f are the fracture aperture, ρ_w and c_w are the fluid density and heat capacity. $\Delta E_{conductive}$ and $\Delta E_{convective}$ are defined.

$$\Delta E_d = -\nabla \cdot Q_{heat}$$ .... (2.31)

$$\Delta E_v = -2a\,\rho_w c_w q_f \nabla T$$ .... (2.32)

q_f is the flow rate in the fracture segment and k_T is the thermal conductivity in fluid. Applying Fourier's law ($Q_{heat} = -k_T w_f \nabla T$), $\Delta E_{conductive}$ is rearranged.

$$\Delta E_d = k_T w_f \nabla^2 T$$ .... (2.33)

The interface heat rate per unit height is,

$$Q_{h-\mathrm{int}} = -2a q_{h-\mathrm{int}}$$ .... (2.34)

Substitute Eq. (2.30), (2.32), (2.33) and (2.34) to Eq. (2.29), the heat transport equation is defined.

$$2a\,w_f\,\rho_w c_w \frac{\partial T}{\partial t} = k_T w_f \nabla^2 T - 2a\,\rho_w c_w q_f \nabla T - 2a q_{h-\mathrm{int}}$$ .... (2.35)

In this thesis, convective transport within the matrix is not considered because in this work, this coupled theory is applied when neglecting convective heat transport in the porous matrix (Ghassemi and Zhang, 2004).

2.5 Fracture Deformation

The joint deformation is usually modeled using the Barton-Bandis (1983) joint model in which the normal effective stress and the normal joint closure are related hyperbolically:

$$\sigma_n' = \frac{K_{ni} D_n}{1 - D_n / D_{n\,max}} \quad\text{...} \quad (2.36)$$

When the fracture deformation is small, this equation can be approximated linearly:

$$\Delta\sigma_n' = -K_n \, \Delta D_n \quad\text{...} \quad (2.37)$$

σ_n' is the effective normal stress (where, $\sigma_n' = \sigma_n + p$, tension positive), K_{ni} is the initial normal stiffness, K_n is the tangent normal stiffness, D_n is the closure and $D_{n\,max}$ is the maximum possible closure of the fracture.

Before yielding, the shear stress has a linear relationship with shear displacement:

$$\Delta\sigma_s = K_s \, \Delta D_s \quad\text{...} \quad (2.38)$$

K_s is the shear stiffness. And shear displacement causes joint dilation which is accounted for by dilation angle (ϕ_d):

$$\Delta D_{n-dilation} = -\Delta D_s \, \tan\phi_d \quad\text{...} \quad (2.39)$$

Adding Eq. (2.39) to Eq. (2.37) and expressing the effective stress as the sum of the total stress and fluid pressure yields:

$$\Delta\sigma_n + \Delta p = -K_n \left(\Delta D_n + \Delta D_s \, \tan\phi_d \right) \quad\text{.................................} \quad (2.40)$$

2.6 Coupling Fracture and Matrix Processes Using DDM

Fully coupled poro-thermoelastic displacement discontinuity method is developed by Tao and Ghassemi (2010) to investigate the fracture aperture and permeability change in naturally fractured reservoirs. This numerical method uses displacement discontinuity method (DDM) for the related fracture deformation, finite difference method (FDM) for solving the fluid flow in fractures and the Barton-Bandis (1983) model for the joint deformation. Also, using this method, the pressure, temperature, leakoff flow rate, heat flux rate, shear and normal displacements in each fracture element at each time steps can be determined. Following equations show the details of numerical approaches.

2.6.1 Coupling DD Equations and Fluid Transport Equation
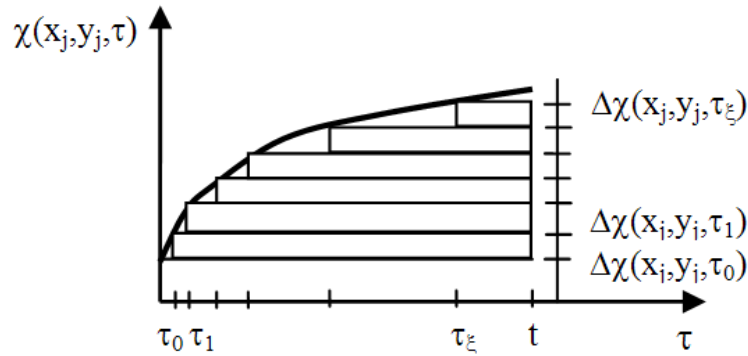
Fig. 2.6 Time marching scheme. χ represents D_n, D_s or q_{int} (Curran & Carvalho, 1987).

Fig. 2.6 shows the time marching scheme and to apply the DDM equations, recall the poro-thermoelastic DD equations, Eq. (2.16) from Section 2.2 and the fluid transport equation, Eq. (2.28) from Section 2.3.

Prior to applying the time marching scheme to the above DDM (Eq. 2.16), fluid

and heat transport equations (Eq. 2.28 and 2.25), this is applied to $\Delta \overset{i}{p}(t)$ and fracture

deformation equations, Eq. (2.38) and Eq. (2.40), so we get Eq. (2.41):

$$\Delta \overset{i}{p}(t) = \overset{i}{p}(t) - \overset{i}{p}_0$$

$$\Delta \overset{i}{\sigma}_n(t) + \overset{i}{p}(t) - \overset{i}{p}_0 = -\overset{i}{K}_n\left(\Delta \overset{i\xi}{D}_n + \Delta \overset{i\xi}{D}_s \tan\phi_d \right)$$

$$-\overset{i}{K}_n\left(\sum_{h=0}^{\xi-1} \Delta \overset{ih}{D}_n + \tan\phi_d \sum_{h=0}^{\xi-1} \Delta \overset{ih}{D}_s \right) \quad \text{...................... (2.41)}$$

$$\Delta \overset{i}{\sigma}_s(t) = \overset{i}{K}_s \Delta \overset{i\xi}{D}_s + \overset{i}{K}_s \sum_{h=0}^{\xi-1} \Delta \overset{ih}{D}_s$$

Where ξ is the current time step and h is the previous time from 1 to $\xi-1$.

After apply time marching scheme and substitute Eq. (2.16), rearrange the equations by

known and unknown terms, the following four equations are obtained.

$$-\overset{i}{p}(t) + \sum_{j=1}^{m} \overset{ij}{p}^{dn}(t-\tau_\xi)\Delta \overset{j\xi}{D}_n + \sum_{j=1}^{m} \overset{ij}{p}^{ds}(t-\tau_\xi)\Delta \overset{j\xi}{D}_s + \sum_{j=1}^{m} \overset{ij}{p}^{q}(t-\tau_\xi)\Delta \overset{j\xi}{q}_{\text{int}}$$

$$+ \sum_{j=1}^{m} \overset{ij}{p}^{T}(t-\tau_\xi)\Delta \overset{j\xi}{q}_{h-\text{int}} = -\overset{i}{p}_0 - \sum_{h=0}^{\xi-1}\sum_{j=1}^{m} \overset{ij}{p}^{dn}(t-\tau_h)\Delta \overset{jh}{D}_n - \sum_{h=0}^{\xi-1}\sum_{j=1}^{m} \overset{ij}{p}^{ds}(t-\tau_h)\Delta \overset{jh}{D}_s$$

$$- \sum_{h=0}^{\xi-1}\sum_{j=1}^{m} \overset{ij}{p}^{q}(t-\tau_h)\Delta \overset{jh}{q}_{\text{int}} - \sum_{h=0}^{\xi-1}\sum_{j=1}^{m} \overset{ij}{p}^{T}(t-\tau_h)\Delta \overset{jh}{q}_{h-\text{int}}$$

$$\text{.. (2.42)}$$

$$\overset{i}{p}(t)+\sum_{j=1}^{m}\overset{ij}{\sigma}_{n}^{dn}(t-\tau_{\xi})\Delta\overset{j\xi}{D}_{n}+\overset{i}{K}_{n}\,\Delta\overset{i\xi}{D}_{n}+\sum_{j=1}^{m}\overset{ij}{\sigma}_{n}^{ds}(t-\tau_{\xi})\Delta\overset{j\xi}{D}_{s}+\overset{i}{K}_{n}\tan\phi_{d}\Delta\overset{i\xi}{D}_{s}$$

$$+\sum_{j=1}^{m}\overset{ij}{\sigma}_{n}^{q}(t-\tau_{\xi})\,\Delta\overset{j\xi}{q}_{\text{int}}+\sum_{j=1}^{m}\overset{ij}{\sigma}_{n}^{T}(t-\tau_{\xi})\Delta\overset{j\xi}{q}_{h-\text{int}}=-\sum_{h=0}^{\xi-1}\sum_{j=1}^{m}\overset{ij}{\sigma}_{n}^{dn}(t-\tau_{h})\Delta\overset{jh}{D}_{n}$$

$$-\sum_{h=0}^{\xi-1}\sum_{j=1}^{m}\overset{ij}{\sigma}_{n}^{ds}(t-\tau_{h})\,\Delta\overset{jh}{D}_{s}-\sum_{h=0}^{\xi-1}\sum_{j=1}^{m}\overset{ij}{\sigma}_{n}^{q}(t-\tau_{h})\Delta\overset{jh}{q}_{\text{int}}-\sum_{h=0}^{\xi-1}\sum_{j=1}^{m}\overset{ij}{\sigma}_{n}^{T}(t-\tau_{h})\Delta\overset{jh}{q}_{h-\text{int}}$$

$$-\overset{i}{K}_{n}\left(\sum_{h=0}^{\xi-1}\Delta\overset{ih}{D}_{n}+\tan\phi_{d}\sum_{h=0}^{\xi-1}\Delta\overset{ih}{D}_{s}\right)+\overset{i}{p}_{0}$$

.... (2.43)

$$\sum_{j=1}^{m}\overset{ij}{\sigma}_{s}^{dn}(t-\tau_{\xi})\Delta\overset{j\xi}{D}_{n}+\sum_{j=1}^{m}\overset{ij}{\sigma}_{s}^{ds}(t-\tau_{\xi})\Delta\overset{j\xi}{D}_{s}-\overset{i}{K}_{s}\,\Delta\overset{i\xi}{D}_{s}+\sum_{j=1}^{m}\overset{ij}{\sigma}_{s}^{q}(t-\tau_{\xi})\Delta\overset{j\xi}{q}_{\text{int}}$$

$$+\sum_{j=1}^{m}\overset{ij}{\sigma}_{s}^{T}(t-\tau_{\xi})\Delta\overset{j\xi}{q}_{h-\text{int}}=-\sum_{h=0}^{\xi-1}\sum_{j=1}^{m}\overset{ij}{\sigma}_{s}^{dn}(t-\tau_{h})\Delta\overset{jh}{D}_{n}-\sum_{h=0}^{\xi-1}\sum_{j=1}^{m}\overset{ij}{\sigma}_{s}^{ds}(t-\tau_{h})\Delta\overset{jh}{D}_{s}$$

$$-\sum_{h=0}^{\xi-1}\sum_{j=1}^{m}\overset{ij}{\sigma}_{s}^{q}(t-\tau_{h})\Delta\overset{jh}{q}_{\text{int}}-\sum_{h=0}^{\xi-1}\sum_{j=1}^{m}\overset{ij}{\sigma}_{s}^{T}(t-\tau_{h})\Delta\overset{jh}{q}_{h-\text{int}}+\overset{i}{K}_{s}\sum_{h=0}^{\xi-1}\Delta\overset{ih}{D}_{s}$$

.... (2.44)

$$\sum_{j=1}^{m}\overset{ij}{C}_{p}\,\overset{j}{p}(t)-2a\Delta\overset{i\xi}{D}_{n}+2a\Delta\overset{i\xi}{q}_{\text{int}}\ =2aw_{f}c_{f}\,\overset{i}{p}(\tau_{\xi})-2a\sum_{h=0}^{\xi-1}\Delta\overset{ih}{q}_{\text{int}}\ -\sum_{h=0}^{\xi}\overset{ih}{q}_{s}$$

.... (2.45)

$\overset{ij}{C}_{p}$ is the fluid coefficient matrix. $\Delta\overset{i\xi}{D}_{n}$, $\Delta\overset{i\xi}{D}_{s}$ and $\Delta\overset{j\xi}{q}_{\text{int}}$ denote the increments of a normal and shear displacement discontinuities and leakoff rate of the *jth* fracture segment at time, t , τ_{ξ} , τ_{h} denote total time, current time step and the time step counter.

2.6.2 Coupling DD Equations and Heat Transport Equation

To arrange the DD equation for temperature and heat transport equation, recall Eq. (2.16) from Section 2.2 and Eq. (2.35) from Section 2.4. Also, $\overset{i}{\Delta T}(t)$ shows the temperature change in current time step which expressed by two terms with current temperature and the temperature of previous time step.

$$\overset{i}{\Delta T}(t) = \overset{i}{T}(t) - \overset{i}{T}_0 \quad\text{...} \quad (2.46)$$

Apply the time marching scheme, substituting Eq. (2.16) and rearrange the resulting equations according to known and unknown terms results:

$$-\overset{i}{T}(t) + \sum_{j=1}^{m} \overset{ij}{T^T}\left(t - \tau_\xi\right)\Delta \overset{j\xi}{q}_{h-\text{int}} = -\overset{i}{T}_0 + \sum_{h=0}^{\xi-1}\sum_{j=1}^{m} \overset{ij}{T^T}\left(t - \tau_h\right)\Delta \overset{jh}{q}_{h-\text{int}} \quad\text{.........} \quad (2.47)$$

$$\sum_{j=1}^{m} \overset{ij}{C_{ht}}\overset{j}{T}(t) + 2a\Delta \overset{i\xi}{q}_{h-\text{int}} = 2a\,w_f\,\rho_w c_w \overset{i}{T}(\tau_\xi) \quad\text{..} \quad (2.48)$$

$\overset{ij}{C_{ht}}$ is the coefficient matrix and c_w is the heat capacity.

2.6.3 Solution Procedure

To solve the fully coupled poro-thermoelastic displacement discontinuity equations, the unknowns should be clearly defined. There are six unknowns namely; temperature (T), heat flux rate ($q_{h\text{-}int}$), normal displacement discontinuity (D_n), shear displacement discontinuity (D_s), pressure (p) and fluid leakoff rate (q_{int}). And there are six equations; Eq. (2.42), Eq. (2.43), Eq. (2.44), Eq. (2.45), Eq. (2.47) and Eq. (2.48). So,

this problem can be solved using implicit numerical procedure (refer the Appendix A for solving matrix, and to Appendix D for a detailed flow chart).

First, using Eq. (2.47) and Eq. (2.48), temperature (T) and/or heat flux rate ($q_{h\text{-}int}$) are determined. And input these results to Eq. (2.42), Eq. (2.43), Eq. (2.44) and Eq. (2.45) and using these four equations, determine normal displacement (D_n), shear displacement (D_s), pressure (p) and fluid leakoff rate (q_{int}) at the end.

2.6.4 Sign Convention

In this thesis, all equations are expressed using the tension positive convention even though in rock mechanics, compression positive convention is usually used.

3. JOINT ELEMENT

This section reviews the elastic joint concept and the failure criteria for shear slip and full opening of the fracture. Also a non-equilibrium joint formulation is introduced. Considering joint deformation, there are two ways to investigate it under a far-field stress. When considering joint to be in equilibrium with the far-field stress, only perturbations of the stress will cause a deformation. However, when the joint is allowed to respond to the initial far-field stress, different results are obtained. Tao and Ghassemi (2010) investigate the fracture aperture and permeability change in naturally fractured reservoirs for joint in equilibrium with the far-field stress. In this section, the formulations for both conditions will be presented and their results will be compared in Section 5.3 for the same geometry and loading/material parameters.

3.1 Elastic Joint

A joint deforms by normal and shear stress (Fig. 3.1).
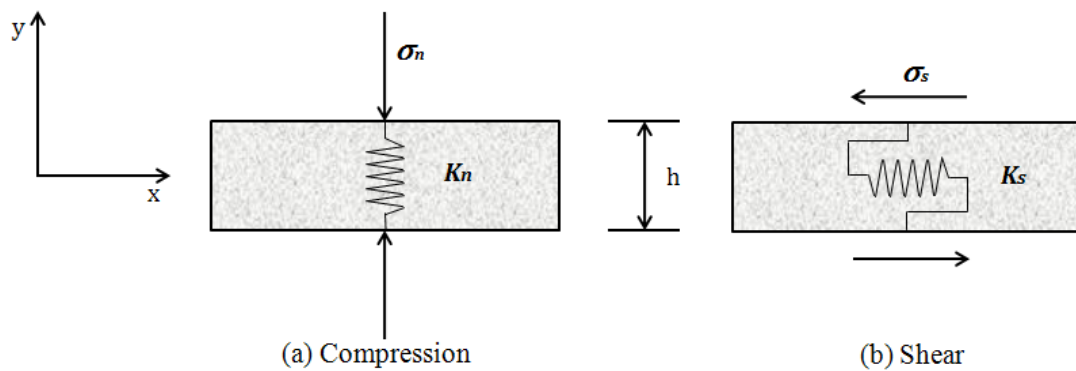
Fig. 3.1 Elastic deformation by normal and shear stress.

The joint deformation is usually modeled using the Barton-Bandis (1983) joint model in which the normal stress and the normal closure are related hyperbolically:

$$\sigma_n' = \frac{K_{ni} D_n}{1 - D_n / D_{n\,max}}$$ .... (3.1)

σ_n' is the effective normal stress, K_{ni} is the initial normal stiffness, D_n is the aperture close and $D_{n\,max}$ is the maximum aperture close of the fracture. When the fracture deformation is small, this equation can be approximated linearly. Eq. (3.1) is used to set up initial condition of the normal deformation. K_n and K_s are the normal and shear stiffness. σ_n and σ_s are the normal and shear stress, respectively. The total effective stress in elastic joint is introduced by Crouch and Starfield (1983).

$$\sigma_n^i = -K_n^i D_n^i$$
$$\sigma_s^i = -K_s^i D_s^i$$ .... (3.2)

According to Eq. (3.2), when the rock joint has higher normal (K_n) and shear stiffness (K_s), the amount of normal and shear deformation is lower compared to when the rock has lower K_n and K_s.

However, for example, when the shear stress is extremely high, the joint slips and the joint does not follow this elastic behavior and goes into a plastic condition.

3.2 Failure Mode

There are two failure modes. One is the permanent shear slip occurring when the shear stress is high enough to deform the fracture permanently or reducing the amount of

effective stress by fluid injection. The other one is the fully opened which occurs when the effective stress goes to zero by pressurization fluid.

3.2.1 Shear Slip

The joint is assumed to deform elastically until the stress conditions cause permanent slip to occur. The Mohr-Coulomb failure criterion (Fig. 3.2) is used to anticipate whether the joint will slip or not.
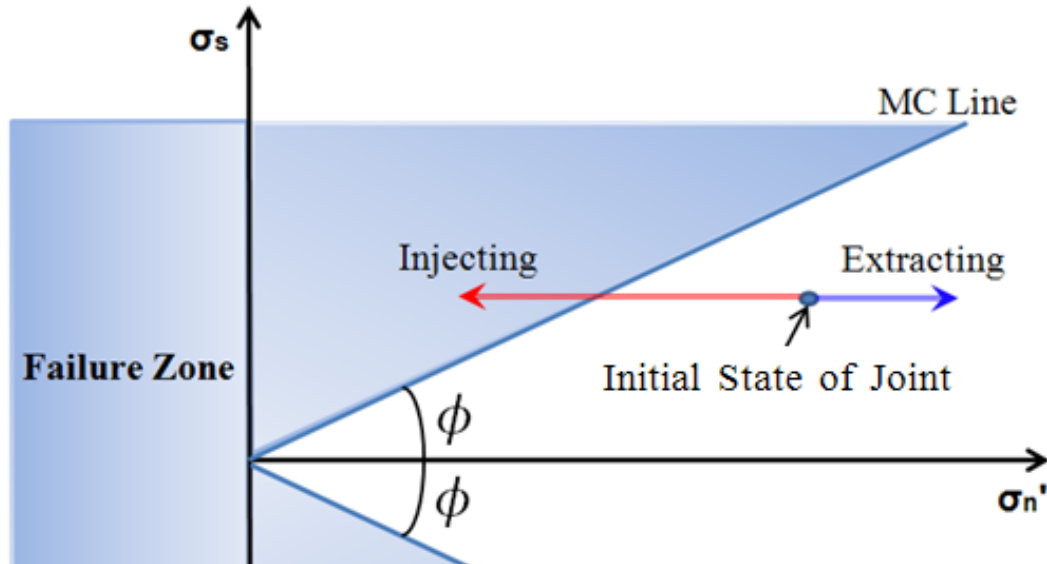
Fig. 3.2 Mohr-Coulomb failure criterion.

Using the maximum shear stress equation (Eq. 3.3) with σ_n' as the effective normal stress, and 'ϕ_f' as the friction angle and 'ϕ_d' the dilation angle, respectively:

The maximum shear stress criterion is:

$$\sigma_{S\max} = \sigma_n' \times \tan(\phi_f + \phi_d)$$ .... (3.3)

The joint yields when the shear stress exceeds the shear strength. In this case, the shear stress is set equal to the maximum allowable value and the joint is allowed to slip by an amount that corresponding to the excess shear stress, τ_p (peak).
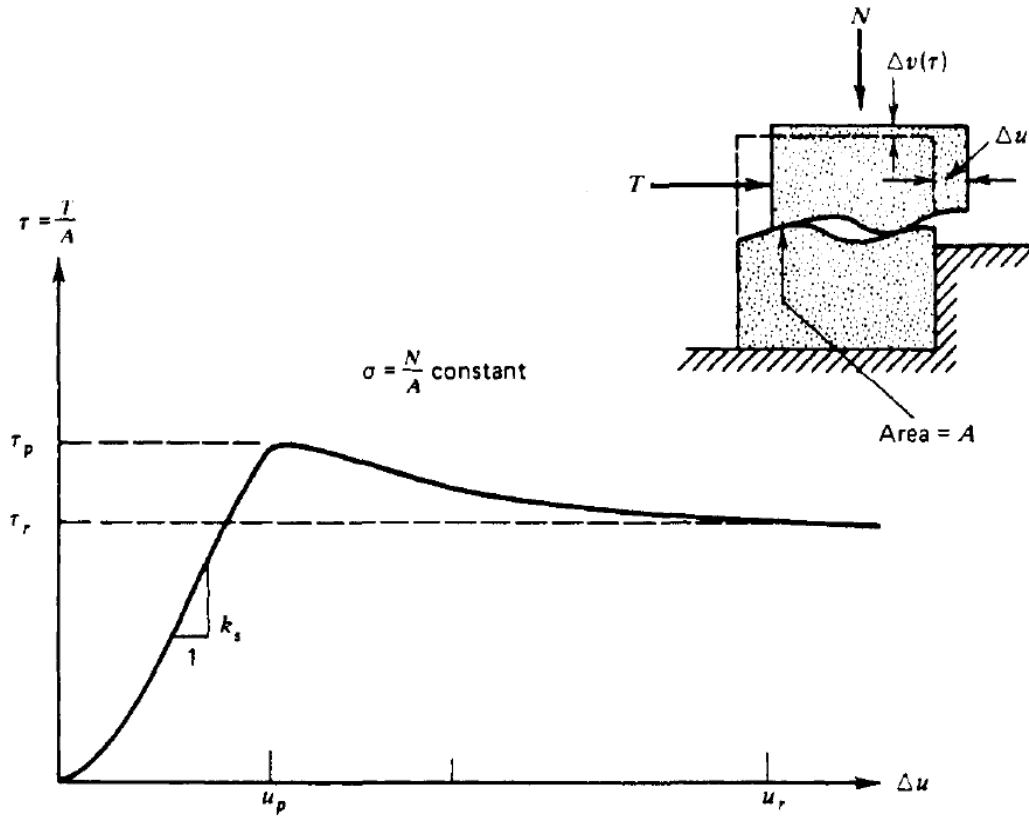
Fig. 3.3 Tangential displacement during direct shear (Goodman, 1989).

Fig. 3.3 shows the shear displacement change by shear stress for a rough joint. But in this application, the joint is not rough, so that τ_p (peak) is close to τ_r (residual). Prior to reaching τ_p, the shear displacement is changed elastically (proportionally). However, after τ_p, the shear displacement is changed is no longer uniquely proportional to stress. So, it means that the shear displacement is under plastic condition.

So, using Fig. 3.2, Fig. 3.3 and Eq. (3.3), when the shear stress is larger than the maximum shear stress (Mohr-Coulomb line), the fracture is located on the right side of the graph (after u_p point) and the shear displacement is changed plastically. The actual shear stress and the maximum allowable shear stress are compared to, judge whether the fracture is yielding or not.

3.2.2 Fully Opened Fracture

According to effective stress equation ($\sigma_n' = \sigma_n - p$, compression positive), the effective stress (σ_n') is positive when the normal stress (σ_n) is greater than pressure (p) in fracture. When injecting fluid into the fracture, the effective stress is decreased by increased pressure in fracture. Later, the effective stress value goes to below zero ($\sigma_n' = \sigma_n - p \leq 0$) and at that time, the joint is fully opened and not a joint anymore. In this thesis, the sign convention is *tension positive*, so the effective stress equation is:

$$\sigma_n' = \sigma_n + P$$ .... (3.4)

3.3 Non-equilibrium Condition

From Crouch and Starfield (1983), the amount of fracture deformation can be calculated including initial far-field stress or excluding initial far-field stress. Tao and Ghassemi (2010) found normal and shear deformations without initial far-field stress, it means that the deformations are calculated only by injection and extraction.

3.3.1 Fracture Deformation without Initial Far-field Stress

From Crouch and Starfield (1983), the total stresses at fracture element i are described in Eq. (3.5).

$$\overset{i}{\sigma}_n = (\overset{i}{\sigma}_n)_0 + \overset{i}{\sigma}_n^{'}$$
$$\overset{i}{\sigma}_s = (\overset{i}{\sigma}_s)_0 + \overset{i}{\sigma}_s^{'} \quad\text{...}\quad (3.5)$$

$\overset{i}{\sigma}_n, \overset{i}{\sigma}_s$ are the total stresses, $(\overset{i}{\sigma}_n)_0, (\overset{i}{\sigma}_s)_0$ are the initial stresses and $\overset{i}{\sigma}_n^{'}, \overset{i}{\sigma}_s^{'}$ are the induced stresses. According to Crouch and Starfield (1983), the induced stresses are defined.

$$\overset{i}{\sigma}_n^{'} = \sum_{j=1}^{m} (\overset{ij}{A}_{nn} \overset{j}{D}_n^{'} + \overset{ij}{A}_{ns} \overset{j}{D}_s^{'})$$
$$\overset{i}{\sigma}_s^{'} = \sum_{j=1}^{m} (\overset{ij}{A}_{sn} \overset{j}{D}_n^{'} + \overset{ij}{A}_{ss} \overset{j}{D}_s^{'}) \quad\text{...}\quad (3.6)$$

$\overset{ij}{A}_{nn}, \overset{ij}{A}_{ns}, \overset{ij}{A}_{sn}$ and $\overset{ij}{A}_{ss}$ represent the boundary influencing coefficients. And also, the local induced stresses are defined.

$$\overset{i}{\sigma}_n^{'} = -\overset{i}{K}_n \overset{i}{D}_n^{'}$$
$$\overset{i}{\sigma}_s^{'} = -\overset{i}{K}_s \overset{i}{D}_s^{'} \quad\text{..}\quad (3.7)$$

Actually, in this condition, the induced stresses are same with the total stresses because there are no initial stresses at the fracture. The initial stresses mean far-field

stresses or initial induced stresses by far-field. So, combining equation Eq. (3.6) and Eq. (3.7) by Eq. (3.5), Eq. (3.8) is derived.

$$0 = \overset{i}{K}_n \overset{i}{D}_n^{'} + \sum_{j=1}^{m} (\overset{ij}{A}_{nn} \overset{j}{D}_n^{'} + \overset{ij}{A}_{ns} \overset{j}{D}_s^{'})$$

$$0 = \overset{i}{K}_s \overset{i}{D}_s^{'} + \sum_{j=1}^{m} (\overset{ij}{A}_{sn} \overset{j}{D}_n^{'} + \overset{ij}{A}_{ss} \overset{j}{D}_s^{'}) \qquad \text{..} \qquad (3.8)$$

3.3.2 Fracture Deformation under Initial (Constant) Far-field Stress

Under non-equilibrium condition (in-situ stresses cause joints to deform), the total stresses on fracture element *i* are described by Crouch and Starfield (1983).

$$\overset{i}{\sigma}_n = (\overset{i}{\sigma}_n)_0 + \overset{i}{\sigma}_n^{'}$$

$$\overset{i}{\sigma}_s = (\overset{i}{\sigma}_s)_0 + \overset{i}{\sigma}_s^{'} \qquad \text{...} \qquad (3.9)$$

$\overset{i}{\sigma}_n, \overset{i}{\sigma}_s$ are the total stresses, $(\overset{i}{\sigma}_n)_0, (\overset{i}{\sigma}_s)_0$ are the initial stresses and $\overset{i}{\sigma}_n^{'}, \overset{i}{\sigma}_s^{'}$

are the induced stresses by injection/extraction (boundary condition), respectively. According to Crouch (1983), the initial stresses are composed of two terms, the resolved far-field stresses and the initial induced stresses due to any deformation on the joint element.

$$(\overset{i}{\sigma}_n)_0 = (\overset{i}{\sigma}_n)_0^{\infty} + (\overset{i}{\sigma}_n^{'})_0$$

$$(\overset{i}{\sigma}_s)_0 = (\overset{i}{\sigma}_s)_0^{\infty} + (\overset{i}{\sigma}_s^{'})_0 \qquad \text{...} \qquad (3.10)$$

$(\overset{i}{\sigma}_n)^\infty_0, (\overset{i}{\sigma}_s)^\infty_0$ are far-field stresses and $(\overset{i}{\sigma'_n})_0, (\overset{i}{\sigma'_s})_0$ are the initial induced stresses. The above equations show that the stresses on deformed joints are different from the initial state. So, substituting Eq. (3.10) to Eq. (3.9) results in:

$$\overset{i}{\sigma}_n = (\overset{i}{\sigma}_n)^\infty_0 + (\overset{i}{\sigma'_n})_0 + \overset{i}{\sigma'_n}$$

$$\overset{i}{\sigma}_s = (\overset{i}{\sigma}_s)^\infty_0 + (\overset{i}{\sigma'_s})_0 + \overset{i}{\sigma'_s}$$ .... (3.11)

The normal and shear stresses sum of the initial induced stresses and the induced stresses are defined:

$$(\overset{i}{\sigma'_n})_0 + \overset{i}{\sigma'_n} = \sum_{j=1}^m (\overset{ij}{A}_{nn} (\overset{j}{D}_n)_0 + \overset{ij}{A}_{ns} (\overset{j}{D}_s)_0) + \sum_{j=1}^m (\overset{ij}{A}_{nn} \overset{j}{D'_n} + \overset{ij}{A}_{ns} \overset{j}{D'_s})$$

$$(\overset{i}{\sigma'_s})_0 + \overset{i}{\sigma'_s} = \sum_{j=1}^m (\overset{ij}{A}_{sn} (\overset{j}{D}_n)_0 + \overset{ij}{A}_{ss} (\overset{j}{D}_s)_0) + \sum_{j=1}^m (\overset{ij}{A}_{sn} \overset{j}{D'_n} + \overset{ij}{A}_{ss} \overset{j}{D'_s})$$ ..... (3.12)

And the total joint deformations are:

$$\overset{i}{D}_n = (\overset{i}{D'_n})_0 + \overset{i}{D'_n}$$

$$\overset{i}{D}_s = (\overset{i}{D'_s})_0 + \overset{i}{D'_s}$$ .... (3.13)

Substitute Eq. (3.13) to Eq. (3.12) yields:

$$(\overset{i}{\sigma'_n})_0 + \overset{i}{\sigma'_n} = \sum_{j=1}^m (\overset{ij}{A}_{nn} \overset{j}{D}_n + \overset{ij}{A}_{ns} \overset{j}{D}_s)$$

$$(\overset{i}{\sigma'_s})_0 + \overset{i}{\sigma'_s} = \sum_{j=1}^m (\overset{ij}{A}_{sn} \overset{j}{D}_n + \overset{ij}{A}_{ss} \overset{j}{D}_s)$$ .... (3.14)

The total stresses on joint element are related to the total joint deformations as already introduced in Section 3.1.

$$\overset{i}{\sigma}_n = -\overset{i}{K}_n \overset{i}{D}_n$$

$$\overset{i}{\sigma}_s = -\overset{i}{K}_s \overset{i}{D}_s$$ .... (3.2)

Substitute Eq. (3.2) and Eq. (3.14) into Eq. (3.11) gives:

$$-(\overset{i}{\sigma}_n)_0^\infty = \overset{i}{K}_n \overset{i}{D}_n + \sum_{j=1}^{m}(\overset{ij}{A}_{nn}\overset{j}{D}_n + \overset{ij}{A}_{ns}\overset{j}{D}_s)$$

$$-(\overset{i}{\sigma}_s)_0^\infty = \overset{i}{K}_s \overset{i}{D}_s + \sum_{j=1}^{m}(\overset{ij}{A}_{sn}\overset{j}{D}_n + \overset{ij}{A}_{ss}\overset{j}{D}_s)$$ .... (3.15)

Using a time marching scheme shown in Fig. 2.6 in previous section and rearranging both equations, we get new equations:

$$\sum_{j=1}^{m}\overset{ij}{\sigma}_n^{dn}(t-\tau_\xi)\Delta\overset{j\xi}{D}_n + \overset{i}{K}_n\Delta\overset{i\xi}{D}_n + \sum_{j=1}^{m}\overset{ij}{\sigma}_n^{ds}(t-\tau_\xi)\Delta\overset{j\xi}{D}_s$$

$$+ \sum_{j=1}^{m}\overset{ij}{\sigma}_n^{q}(t-\tau_\xi)\Delta\overset{j\xi}{q}_{\text{int}} + \sum_{j=1}^{m}\overset{ij}{\sigma}_n^{T}(t-\tau_\xi)\Delta\overset{j\xi}{q}_{h-\text{int}} = -\sum_{h=0}^{\xi-1}\sum_{j=1}^{m}\overset{ij}{\sigma}_n^{dn}(t-\tau_h)\Delta\overset{jh}{D}_n$$

$$-\sum_{h=0}^{\xi-1}\sum_{j=1}^{m}\overset{ij}{\sigma}_n^{ds}(t-\tau_h)\Delta\overset{jh}{D}_s - \sum_{h=0}^{\xi-1}\sum_{j=1}^{m}\overset{ij}{\sigma}_n^{q}(t-\tau_h)\Delta\overset{jh}{q}_{\text{int}}$$

$$-\sum_{h=0}^{\xi-1}\sum_{j=1}^{m}\overset{ij}{\sigma}_n^{T}(t-\tau_h)\Delta\overset{jh}{q}_{h-\text{int}} - \overset{i}{K}_n\sum_{h=0}^{\xi-1}\Delta\overset{ih}{D}_n - (\overset{i}{\sigma}_n)_0^\infty$$

.... (3.16)

$$\sum_{j=1}^{m} \overset{ij}{\sigma_s^{dn}}(t-\tau_\xi)\Delta \overset{j\xi}{D_n} + \sum_{j=1}^{m} \overset{ij}{\sigma_s^{ds}}(t-\tau_\xi)\Delta \overset{j\xi}{D_s} - K_s \Delta \overset{i\xi}{D_s}$$

$$+ \sum_{j=1}^{m} \overset{ij}{\sigma_s^{q}}(t-\tau_\xi)\Delta \overset{j\xi}{q}_{\text{int}} + \sum_{j=1}^{m} \overset{ij}{\sigma_s^{T}}(t-\tau_\xi)\Delta \overset{j\xi}{q}_{h-\text{int}} = -\sum_{h=0}^{\xi-1}\sum_{j=1}^{m} \overset{ij}{\sigma_s^{dn}}(t-\tau_h)\Delta \overset{jh}{D_n}$$

$$-\sum_{h=0}^{\xi-1}\sum_{j=1}^{m} \overset{ij}{\sigma_s^{ds}}(t-\tau_h)\Delta \overset{jh}{D_s} - \sum_{h=0}^{\xi-1}\sum_{j=1}^{m} \overset{ij}{\sigma_s^{q}}(t-\tau_h)\Delta \overset{jh}{q}_{\text{int}}$$

$$-\sum_{h=0}^{\xi-1}\sum_{j=1}^{m} \overset{ij}{\sigma_s^{T}}(t-\tau_h)\Delta \overset{jh}{q}_{h-\text{int}} + K_s \sum_{h=0}^{\xi-1}\Delta \overset{ih}{D_s} - \overset{i}{(\sigma_s)}_0^\infty$$

.... (3.17)

Eq. (3.16) represents the total normal stress of the system. But in numerical calculations, the effective stress equation is used. So, substituting Eq. (2.40) and Eq. (3.4) to Eq. (3.16) gives:

$$\overset{i}{p}(t) + \sum_{j=1}^{m} \overset{ij}{\sigma_n^{dn}}(t-\tau_\xi)\Delta \overset{j\xi}{D_n} + K_n \Delta \overset{i\xi}{D_n} + \sum_{j=1}^{m} \overset{ij}{\sigma_n^{ds}}(t-\tau_\xi)\Delta \overset{j\xi}{D_s}$$

$$+ K_n \tan\phi_d \Delta \overset{i\xi}{D_s} + \sum_{j=1}^{m} \overset{ij}{\sigma_n^{q}}(t-\tau_\xi)\Delta \overset{j\xi}{q}_{\text{int}} + \sum_{j=1}^{m} \overset{ij}{\sigma_n^{T}}(t-\tau_\xi)\Delta \overset{j\xi}{q}_{h-\text{int}}$$

$$= -\sum_{h=0}^{\xi-1}\sum_{j=1}^{m} \overset{ij}{\sigma_n^{dn}}(t-\tau_h)\Delta \overset{jh}{D_n} - \sum_{h=0}^{\xi-1}\sum_{j=1}^{m} \overset{ij}{\sigma_n^{ds}}(t-\tau_h)\Delta \overset{jh}{D_s} - \sum_{h=0}^{\xi-1}\sum_{j=1}^{m} \overset{ij}{\sigma_n^{q}}(t-\tau_h)\Delta \overset{jh}{q}_{\text{int}}$$

$$-\sum_{h=0}^{\xi-1}\sum_{j=1}^{m} \overset{ij}{\sigma_n^{T}}(t-\tau_h)\Delta \overset{jh}{q}_{h-\text{int}} - K_n \left(\sum_{h=0}^{\xi-1}\Delta \overset{ih}{D_n} + \tan\phi_d \sum_{h=0}^{\xi-1}\Delta \overset{ih}{D_s} \right) + \overset{i}{p}_0 - \overset{i}{p}_0 - \overset{i}{(\sigma_n)}_0^\infty$$

.... (3.18)

Therefore, using Eq. (2.42), (2.47), (3.17) and Eq. (3.18) with Eq. (2.45) and Eq. (2.48) which are introduced in previous section, the unknown values, ΔD_n, ΔD_s, Δq_{int}, Δq_{h-int}, T and p can be determined.

4. MODEL VERIFICATION AND MECHANICAL ANALYSIS

In this section, the fully coupled DDM is used to simulate a simple fracture network to investigate and analyze the mechanical movement of the fractures and to study the conditions for the onset of permanent shear slip. The input parameters used in eth simulation of this section and Section 5 are listed in Table 4.1 and Table 4.2. The joint parameters are extracted from Tao and Ghassemi (2010).

Table 4.1
Rock properties of Westerly granite (McTigue, 1990).

Shear modulus G (GPa)	15
Possoin's ratio v	0.25
Undrained Possoin's ratio v_u	0.33
Matrix permeability (m^2)	4×10^{-19}
Matrix porosity ϕ	0.01
Biot's coefficient α	0.44
Fluid viscosity μ (cp)	3.547×10^{-4}
Fluid compressibility (MPa^{-1})	4.2×10^{-4}
Thermal expansion coefficient of solid α_s (K^{-1})	2.4×10^{-5}
Thermal expansion coefficient of pore fluid α_f (K^{-1})	2.1×10^{-5}
Thermal diffusivity of intact porous rock c^T (m^2/s)	1.1×10^{-6}
Fluid density ρ_f (Kg/m^3)	1×10^3
Heat capacity of fluid c_w (J kg^{-1} K^{-1})	4200
Thermal conductivity of fluid k_T (J s^{-1} m^{-1} K^{-1})	0.6
Normal Stiffness (GPa/m)	1×10^{11}
Shear Stiffness (GPa/m)	0.5×10^{11}

**Table 4.2**
Input parameters.

Initial reservoir temperature (K)	420
Initial normal stiffness (GPa/m)	0.5
The maximum closure (mm)	0.3
In-situ stress (MPa)	30
Initial reservoir pressure (MPa)	27

4.1 Simulating an Injection Well Using Fracture Elements

In this example, a single well is simulated using the DD and DD element (Fig. 4.1). Injection rate (or pressure) and temperature are prescribed and the radial stress and tangential stress change around the well are calculated. Refer the Appendix B for field points coordinates. The total injection rate in each of the 50 wells is 1×10^{-8} m^3/sec for 2 years (730 days) of operation. And the radius (r_w) of the circular fracture is 0.1 m, similar to a real well. Other input parameters are from Table 4.1 and Table 4.2. (Variables such as in-situ stresses in Table 4.2 will be changed for each case study.)
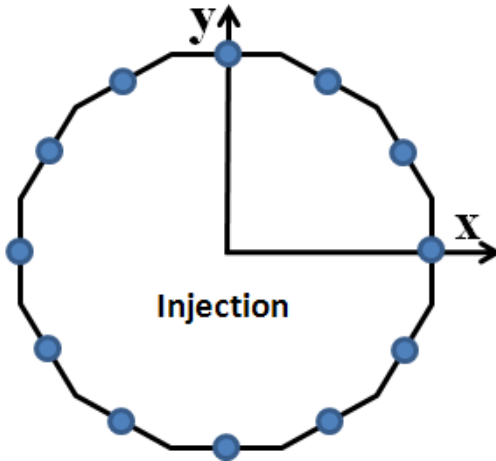
Fig. 4.1 A circle fracture network for simulating a well. 50 fracture elements are used in the simulations with the same injection rate prescribed on DD element (refer Appendix B).

Cooling and heating cases are considered to investigate how the pressure changes in each case. The pressure changes both in cooling and heating cases shown in Fig. 4.2. It can be seen that the pressure for the non-isothermal cases ($\pm$120 K) are different from the start and after 0.1 days, they gradually converge to the isothermal case.
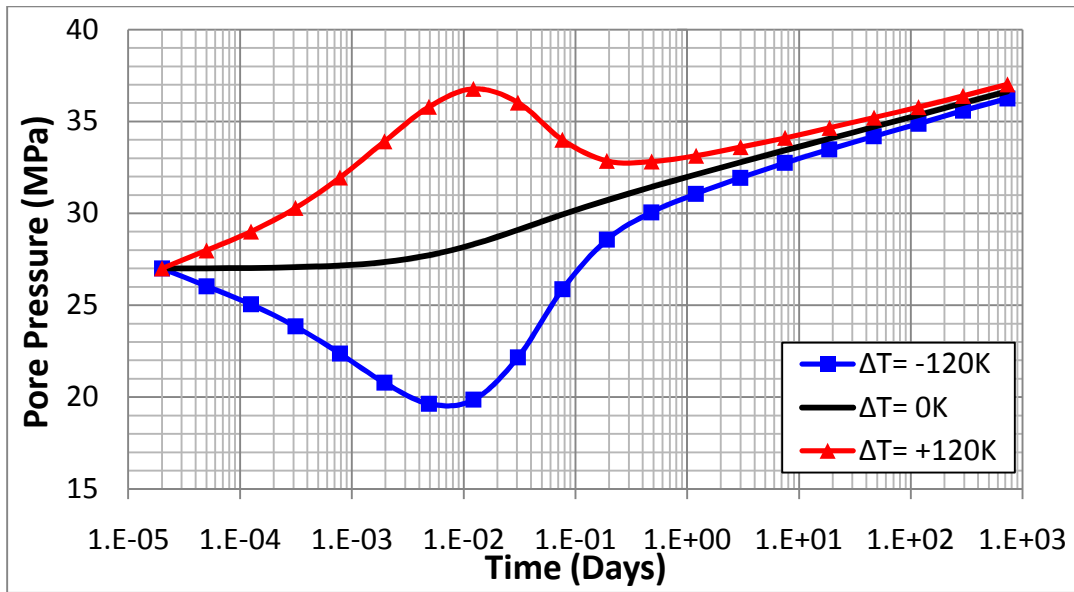
Fig. 4.2 Pressure variation in time at well in cooling, heating and isothermal cases.

According to Fig. 4.2, the fracture pressure for the non-isothermal case changes (decrease or increase). However, after few hours of operations, the pressures in all cases are increased gradually with injections.
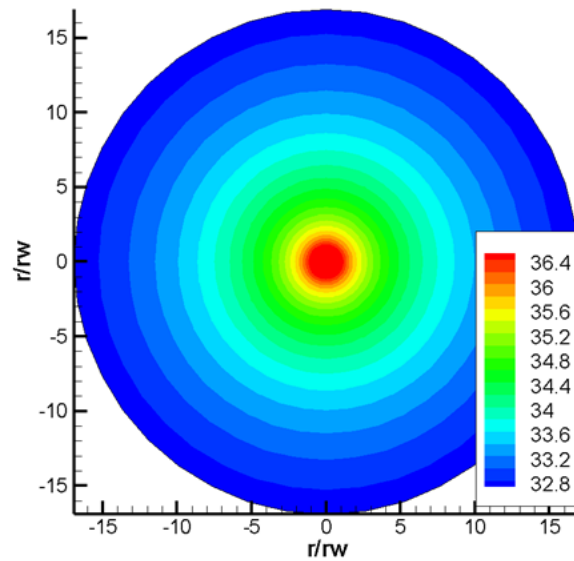
Fig. 4.3 Pressure (MPa) distribution after 2 years injection in isothermal condition.
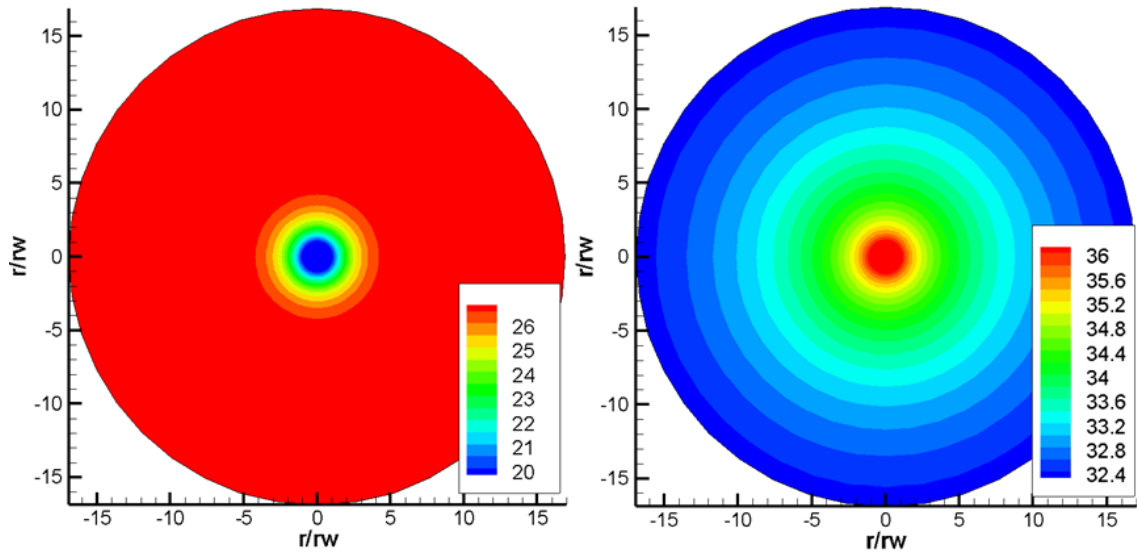
Fig. 4.4 Pressure (MPa) distribution after 1 hour (left)/ 2 years (right) injection in cooling.
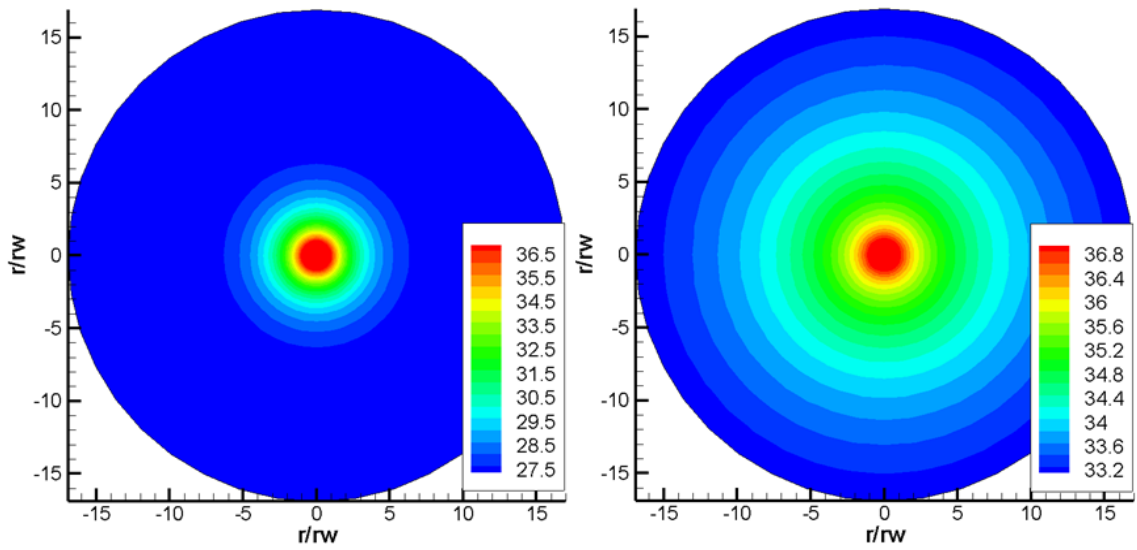
Fig. 4.5 Pressure (MPa) distribution after 1 hour (left)/ 2 years (right) injection in heating.

In Fig. 4.2, 4.3, 4.4 and 4.5, the quick (after 1 hour) pressure change for the non-isothermal cases caused by the temperature of the fluid itself. After 0.1 days, the

pressures are gradually increased by injection and the pressures in cooling, isothermal and heating reach 36 MPa, 36.4 MPa and 36.8 MPa, respectively.
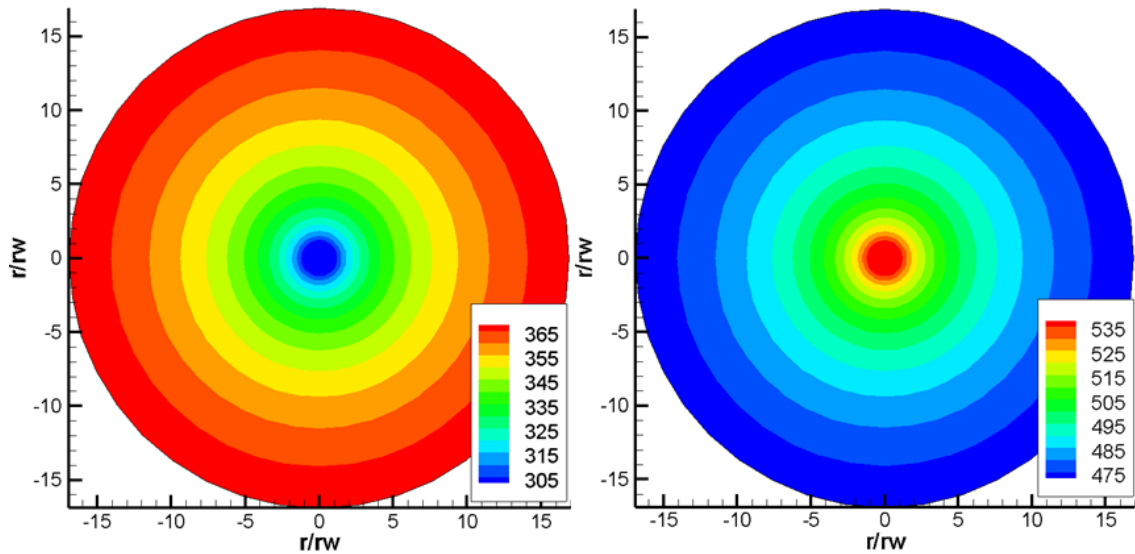
Fig. 4.6 Temperature (K) distribution after 2 years injection in cooling (left)/ heating (right).

Fig. 4.6 shows that with time, the cold or hot temperature front spread out in the porous matrix by conduction and, the distances of the temperature distribution from the wellbore are about just 20 times of the radius at the end.

To verify the result, the pressure, temperature, radial and tangential stress caused by injection is compared with analytical solutions came from Ghassemi and Tao (2010). Detail equations are introduced in Appendix C.
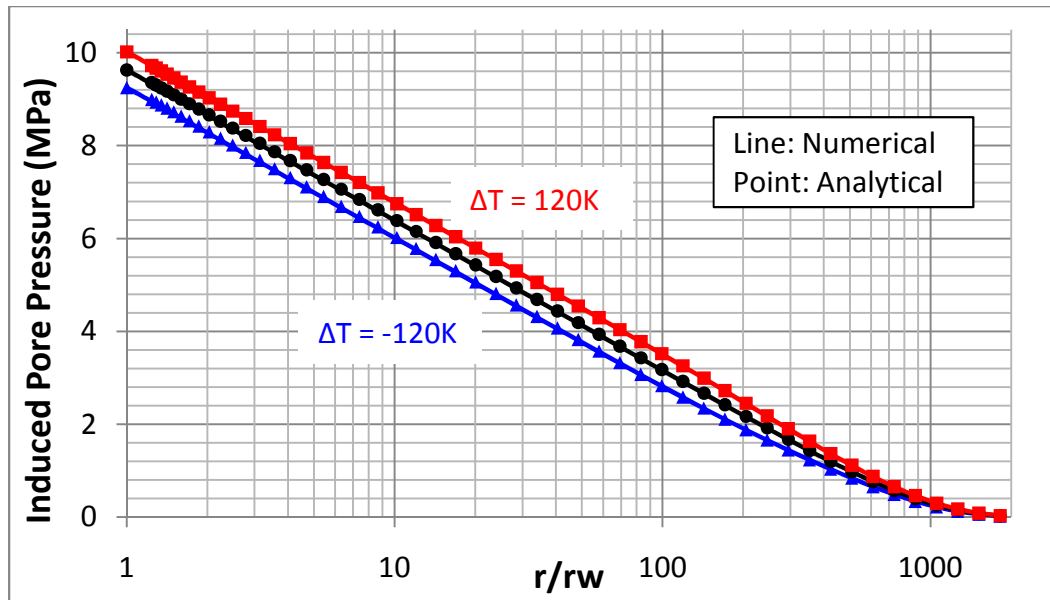
Fig. 4.7 Pressure (MPa) changes by distance in isothermal, cooling and heating.
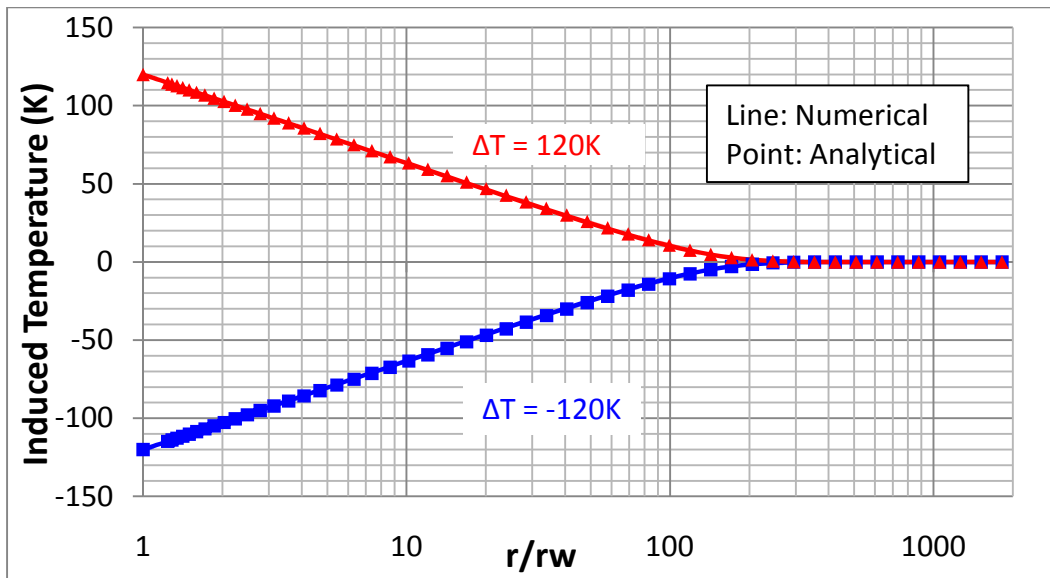
Fig. 4.8 Temperature (K) changes by distance in isothermal, cooling and heating.

Fig. 4.7 and 4.8 show the pressure and temperature variation for each case as a function of distance from the wellbore. The pressure decreases non-linearly from the

injection well. Comparing Fig. 4.7 and Fig. 4.8, it can be seen that the pore pressure spreads out much faster than the temperature because of higher fluid diffusivity.
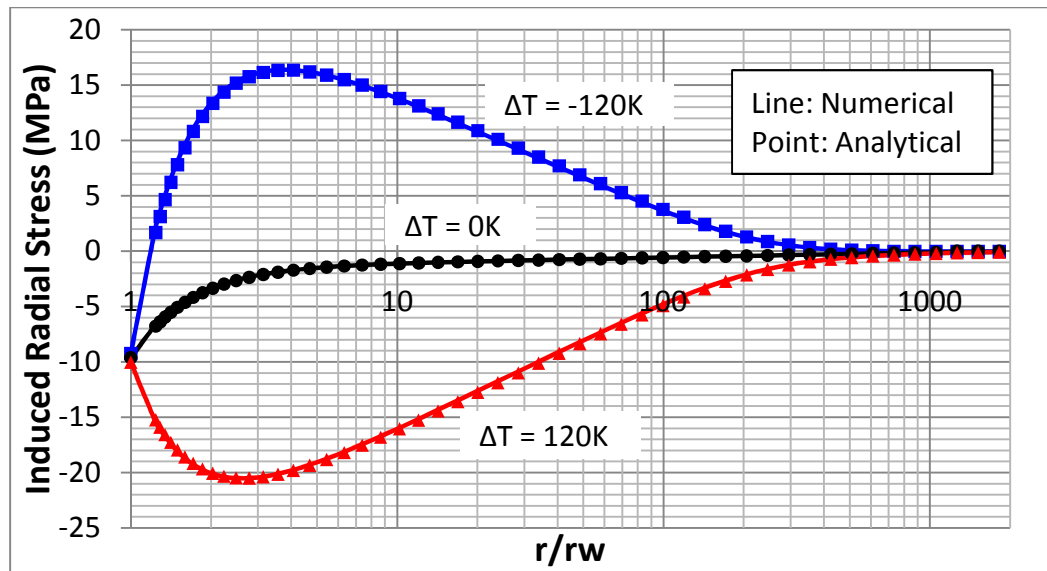
Fig. 4.9 Radial stress (MPa) changes by distance in isothermal, cooling and heating.
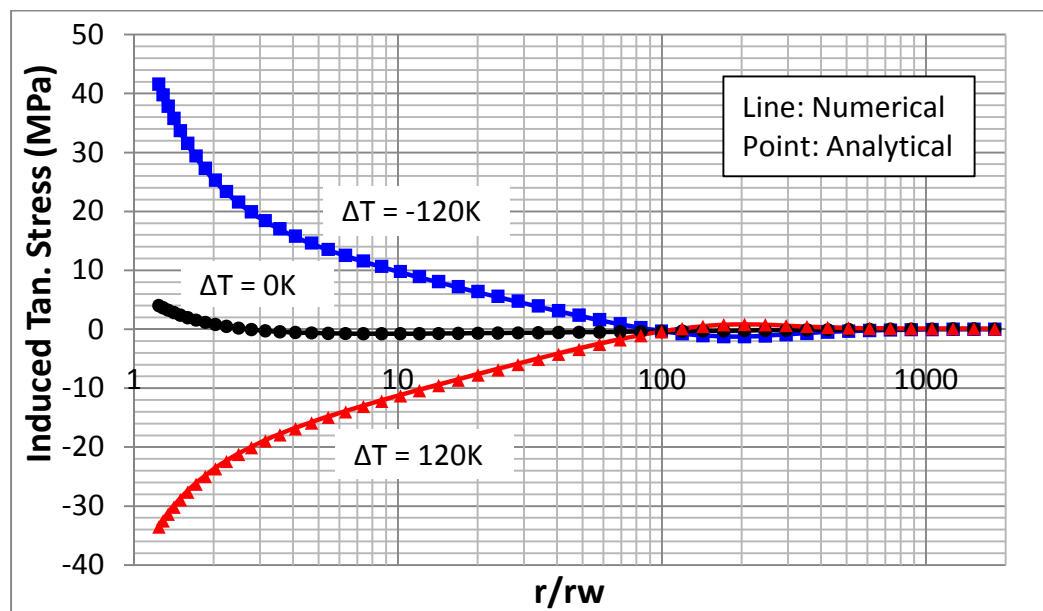
Fig. 4.10 Tangential stress (MPa) changes by distance in isothermal, cooling and heating.

According to Fig. 4.9 and Fig. 4.10, the radial and tangential stresses are compressive or tensile depending on the temperature change. Since the rock tends to shrink when cooled, the induced stresses are tensile. Note that the magnitude of tangential stress is higher than radial. Also, the tangential stress changes the sign at some distance from the injection well and becomes compressive for cold water injection. This is because of strain compatibility.

The plots of temperature pore pressure and stress show that the numerical solutions are in very good agreement with the analytical solution and there is no significant difference between them.

4.2 Shear Deformation and Permanent Slip under In-situ Stress
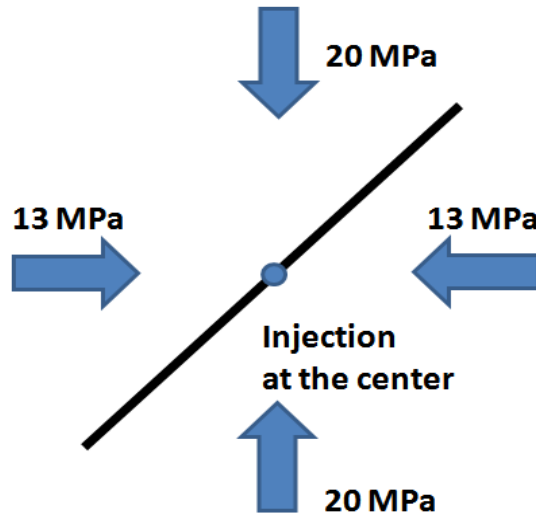
Fig. 4.11 A 40 m fracture inclined at 45 degrees. The fracture is modeled using 39 constant DD elements.

In the single fracture case, water is injected into a well located at the center of the fracture, at a rate of 6×10^{-8} m^3/sec. The rock mass is under anisotropic stress with an

initial pore pressure of 10 MPa. The initial far-field in y-direction is -20 MPa (tension positive) and in x-direction is -13 MPa and both stresses compress the fracture, resulting in 3.5 MPa of shear stress along the fracture (Fig. 4.11). Fracture slip, i.e., the permanent shear movement of the crack (Fig. 3.2) is assessed for an injection time of 6 months. When injecting under isothermal condition, the amount of effective normal stress on the fracture decreases as pressure in the fracture increases, enhancing the shear failure potential. On the other hand, when water is extracted from the fracture, the opposite occurs and the amount of effective stress increases, reducing the possibility of fracture slip. Referring to Fig. 3.2, the fracture status moves away from the Mohr-Coulomb failure line. We note that for the non-isothermal case, the joint fully opens and this opening causes shear slip on all fracture segments.
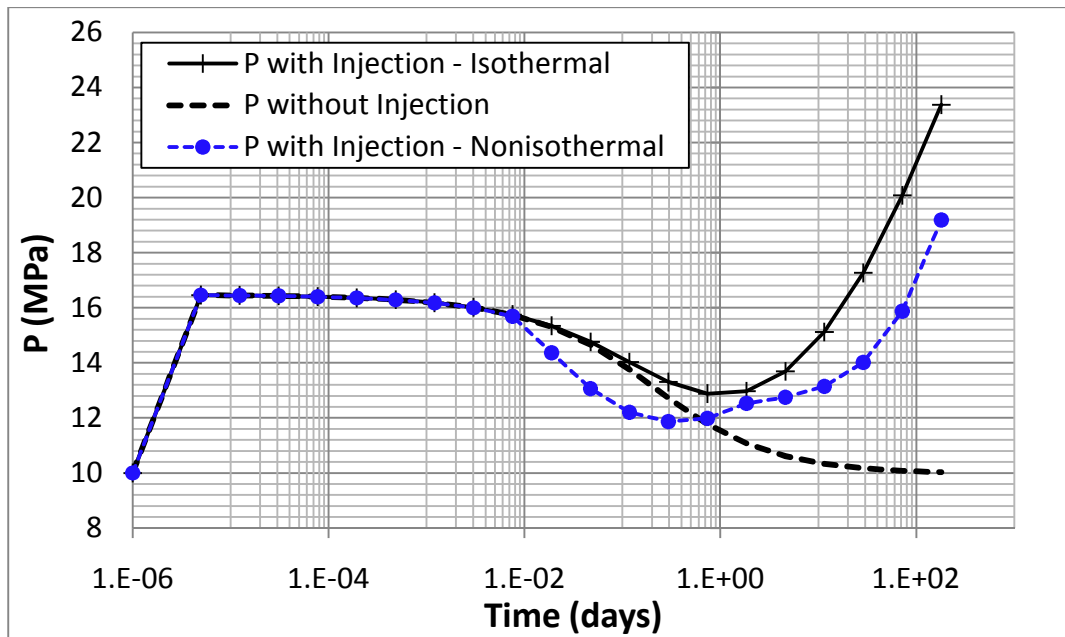
Fig. 4.12 Fracture pressure variation with time at injection well for isothermal and non-isothermal conditions.

According to Fig. 4.12, because of initial far-field stress and low compressibility of water, an initial rapid pressure rise to 16.5 MPa is observed, even though the initial pressure is 10 MPa in the fracture. With time, the pressure in the fracture decreases to the initial pressure of 10 MPa, with or without injection. However, when injecting, the pressure starts to increase after initial decay. A few points are worth noting in the pressure profiles. In non-isothermal (cooling) condition, the pressure is generally lower than isothermal case because of lower temperature (20 K cooling). Until the 9th time step, the pressures in all three cases are almost same. But in 10th time step in non-isothermal case, the pressure starts to drop more rapidly because of the cooling effect that begins to spread out to the fracture surface from the injection well. And after several steps, the pressure increase gradually in response to continued injection. At a time of 1 day, the pressure curve begins to show an increase followed by a rapid leveling off at 2 days, and a subsequent gradual rise. This variable response is caused in response to full opening of the joint under combined hydraulic pressure and thermal stress. At this stage, the element properties and boundary conditions are changed to that of a fully opened fracture (when the effective normal stress is positive, the joint is opened). Fig. 4.13, 4.14, 4.15 and 4.16 illustrate the normal displacement and the effective stress change at the injection point.
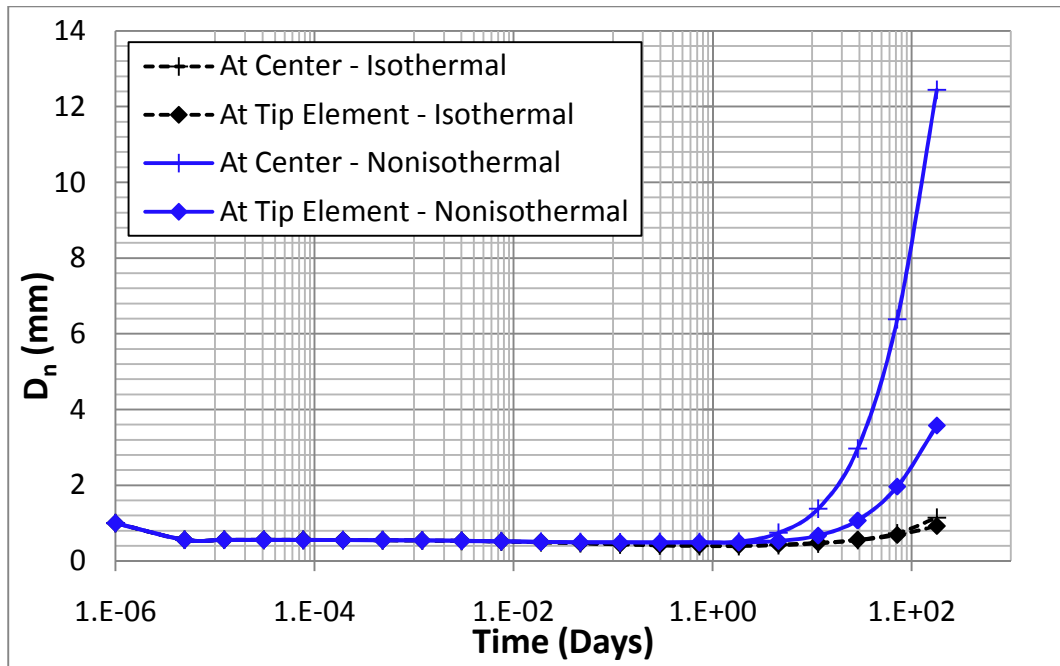
Fig. 4.13 Normal DD (fracture aperture) change with time at injection well for isothermal/non-isothermal conditions.

Initially, the opening response follows the pressure profile in Fig. 4.12, but after 1 day, the fracture aperture in the non-isothermal case begins to increase more than the isothermal case due to the cooling effect. As the cooling diffuses out from the fracture surface into the matrix, the rock starts to contract, increasing D_n and resulting in a lower pressure than the isothermal condition. And from 15th time step (right after 1 day), the D_n is increased because of the injection. From 17th time step (right after 2 day), the D_n increases rapidly because the fracture is now fully opened by combining effect of cooling and injection and no resistance is offered by the joint stiffness. After 180 days, the D_n at the center of the fracture reaches 12.4 mm.
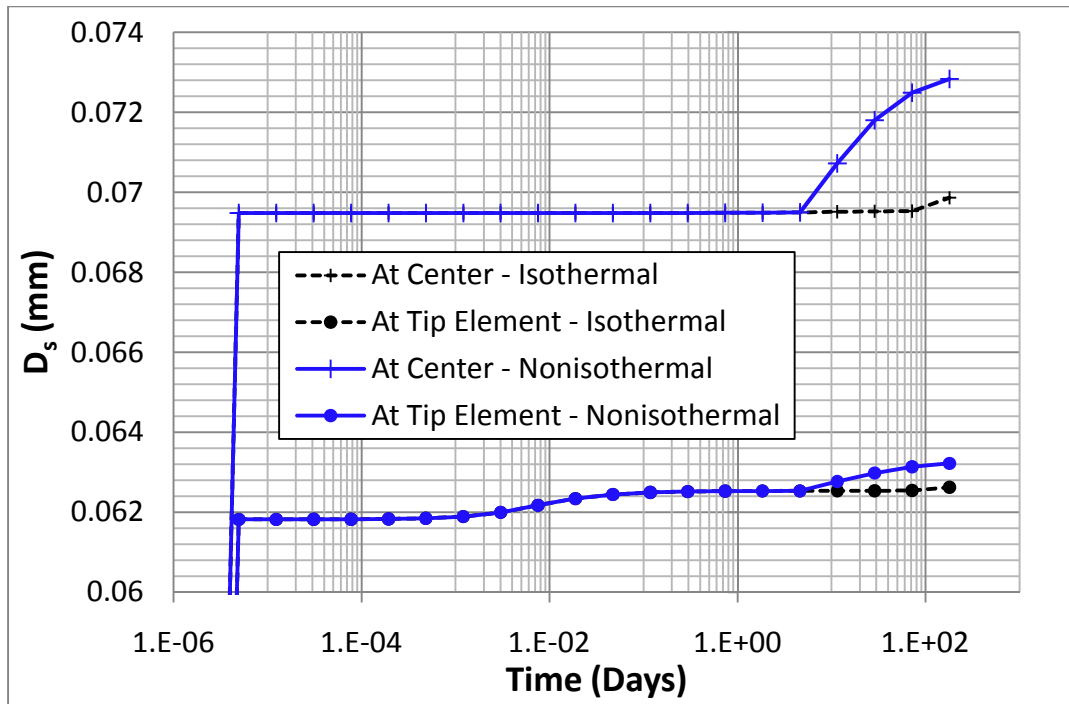
Fig. 4.14 Shear DD (D_s) change with time at the injection well for isothermal and non-isothermal conditions (Initially, $D_s = 0$).

Before operation, there is no deformation, so it is zero initially and as injection proceeds and effective normal stress is reduced, the shear stress caused by anisotropic in-situ stresses creates shear deformation. Fig. 4.14 shows the shear failure at the end of the time step in isothermal condition and at 19th time step in non-isothermal condition. Since the fracture is fully opened at the center of the fracture in early time step, the shear failure occurs earlier in cooling condition. Up to a time of 8 days, the shear displacement is nearly constant for both cases.
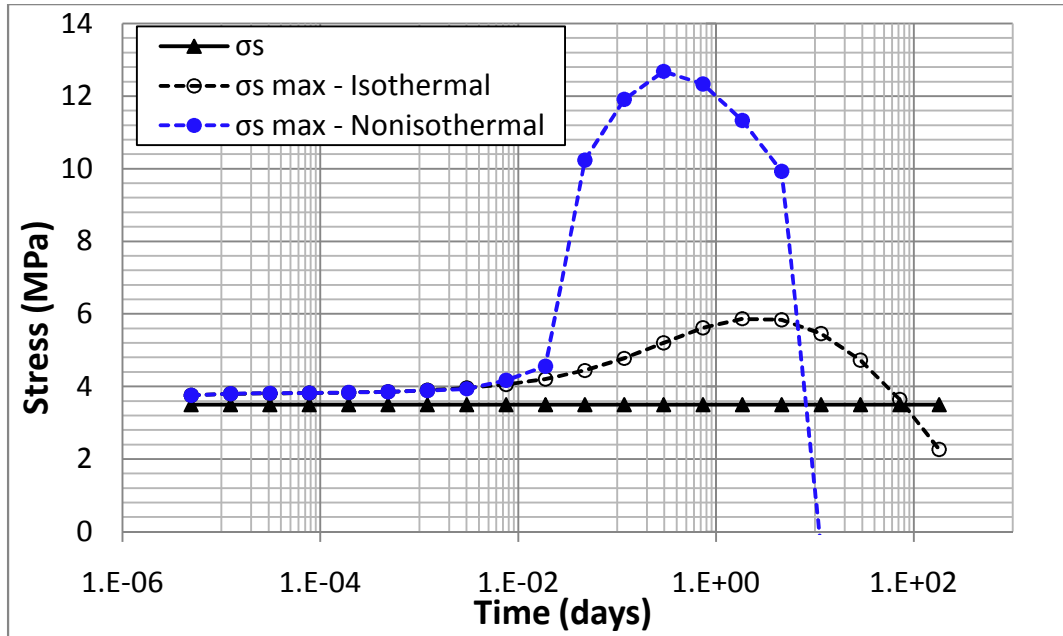
Fig. 4.15 Initial far-field shear stress and the maximum allowable shear stress (Eq. 3.2) at the injection well for isothermal and non-isothermal conditions.
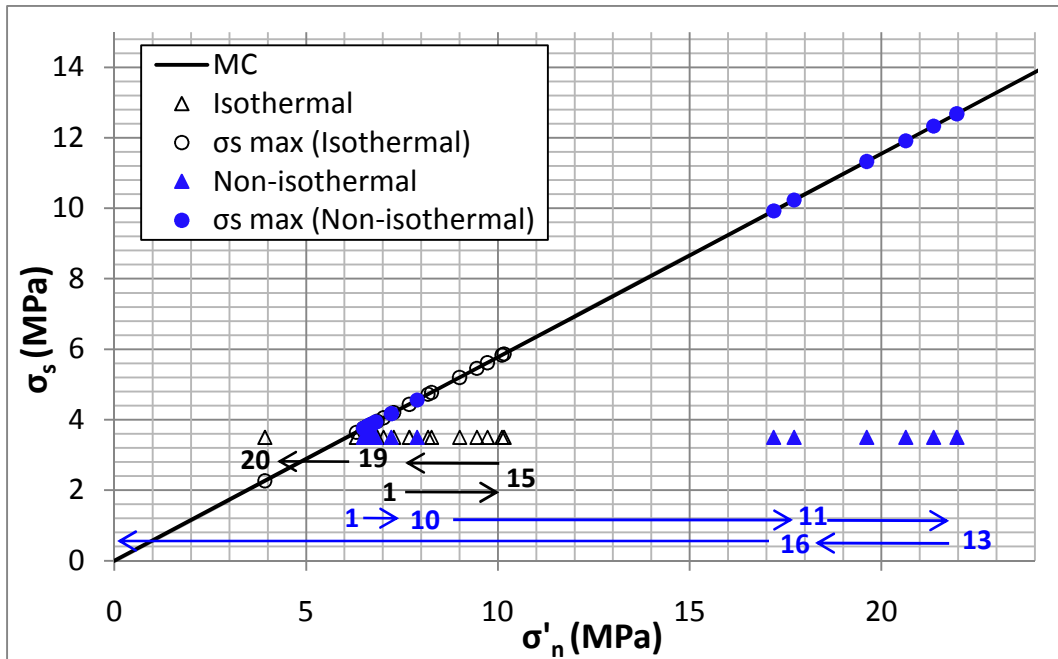
Fig. 4.16 Shear stress and its maximum change at injection well in isothermal and non-isothermal conditions.

In Fig. 4.15 and 4.16, the sign convention of the effective stress is compression positive. In Fig. 4.15, in isothermal case, the maximum allowable shear stress is changed with time because the effective stress varies with fluid compression and injection (pore pressure changes). It can be seen in Fig. 4.16 that because of the fluid compressibility, the amount of effective stress initially increases, and then decreases as the fracture pressure starts to increase because of fluid injection. The amount of normal effective stress eventually declines and the condition for Mohr-Coulomb failure is reached and permanent shear slip occurs. Note that the shear stress value due to the in-situ stress is constant from the start. For the cooling case, the maximum shear stress rapidly drops at about 10 days and the fracture is fully opened. When cooling is taken into account, the amount of effective stress decreases drastically at time 8 days and becomes negative at time 10 days, so the joint is an open fracture. Before completely opening, the joint also slips in response to the reduced amount of normal effective stress. At this stage, the fracture segments at the center of the fracture are opened first. And after 30 days, the fracture is fully opened. The joint opening profile is shown in Fig. 4.17 and we can see that the fracture segments near the center of the fracture are fully opened while fracture segments are still closed. As expected, the non-isothermal injection results in the highest fracture aperture with its maximum at the injection point.
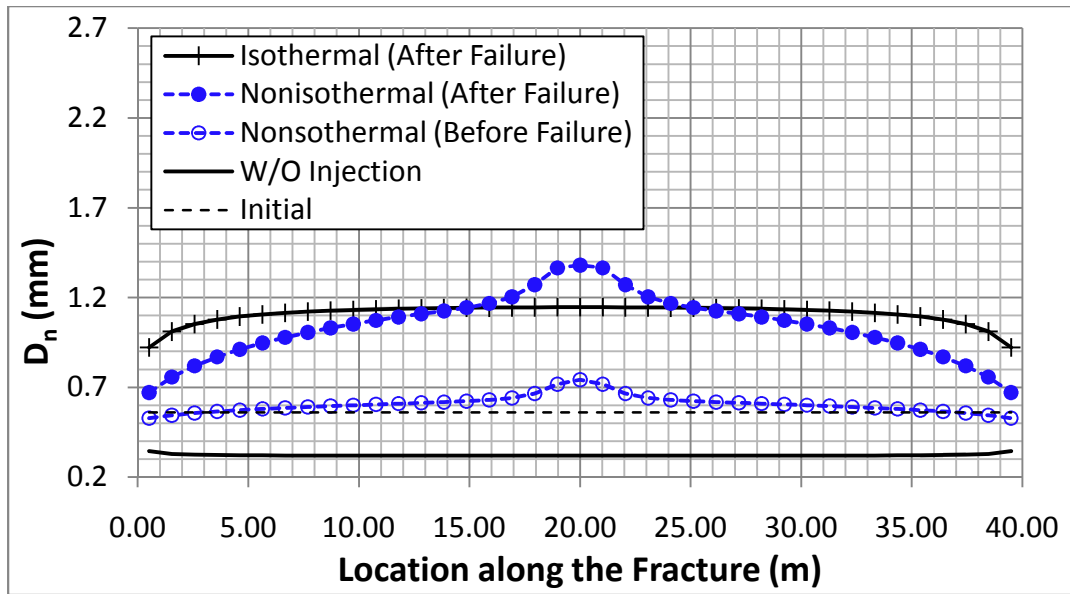
Fig. 4.17 Normal DD (D_n) along the joint.
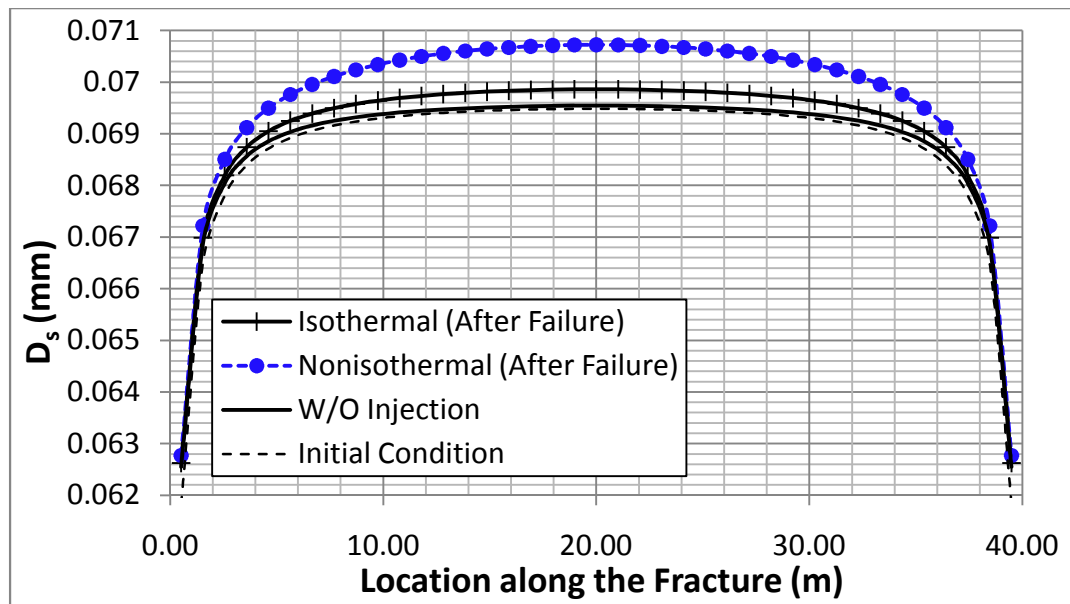
Fig. 4.18 Shear DD (D_s) along the joint.

Fig. 4.18 shows the joint shear deformation along its length. There is no noticeable difference between isothermal and non-isothermal cases before failure

because the shear deformation is entirely caused by initial far-field stress and not by injection. But after failure, the amount of shear slip is different for the cooling case as the fracture is fully opened by thermal stress not by injection pressure.

When comparing Fig. 4.17 and Fig. 4.18, right after failure in cooling case, we can see that the fracture has also slipped when there is fracture opening at the center of the fracture. It means that when the fracture segment is fully opened at the center of the fracture, it causes the fracture slipped at the same time.

The pore pressure and temperature distributions are illustrated in Fig. 4.19, 4.20 and 4.21 for 180 days of injection. The pressure distribution for the isothermal case is higher everywhere when compared to the cooling case. This is because rock cooling reduces the pore pressure due to differential thermal contraction of the pore fluid and the rock matrix.
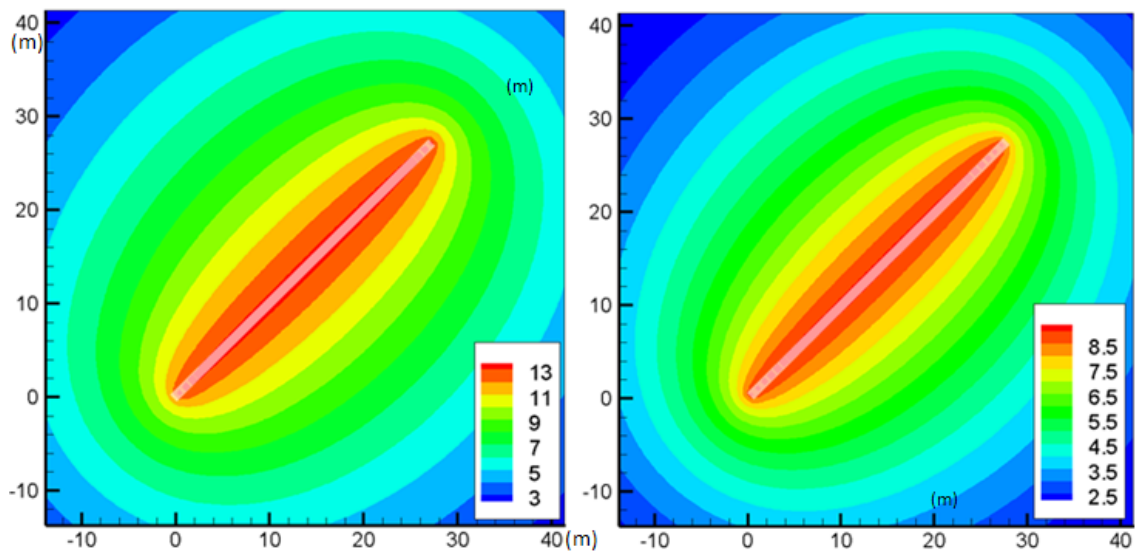
Fig. 4.19 Induced pressure Δp (MPa) distribution after 180 days of injection under isothermal condition (left) and non-isothermal condition (right).

However, according to Fig. 4.19, the fracture pressures in isothermal and non-isothermal cases reach about 19 MPa and 12 MPa (initial pressure, 10 MPa) just before failure, respectively and at the end of operation those reach about 23 MPa and 19 MPa. In the isothermal case, failure occurs by injection at the end of time step due to high pressure. But in non-isothermal case, failure occurs earlier by cooling, so even though the fracture pressure is lower, the fracture is fully opened.
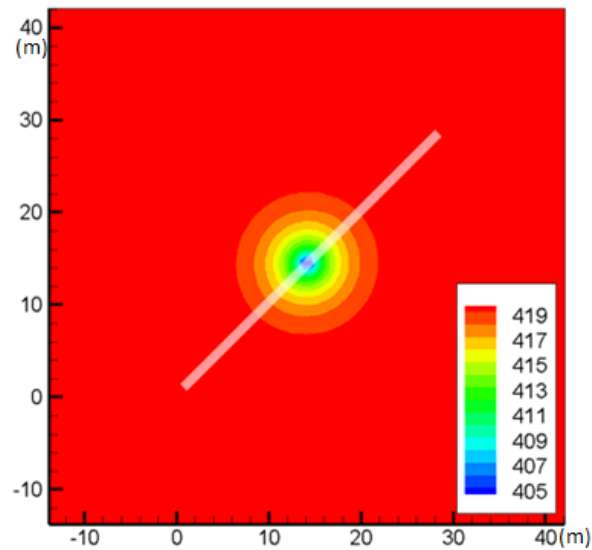
Fig. 4.20 Temperature (K) distribution after 180 days of injection.

The corresponding reservoir temperature distribution is shown in Fig. 4.20. The initial reservoir is 420 K and the temperature of cooling fluid is 400 K. In early time, even though the fracture temperature at injection well is very low, the matrix temperature is still high. With time, the cold front spreads out to the field. Note that even though a cool fluid is injected into the fracture, cooling does not spread out to other fracture segment (the pressure is nearly uniform because of the conduction domination

in fracture) as the fluid can only diffuse into the matrix without a production well
(convective transport within the matrix is not considered in this work).
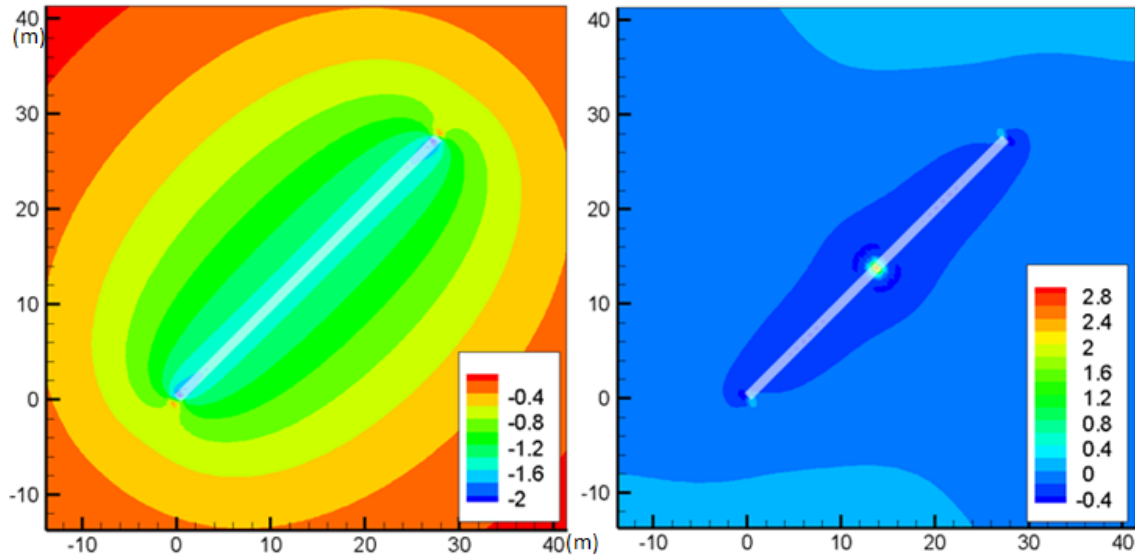
Fig. 4.21 Induced effective mean stress (MPa), $(\Delta\sigma'_{xx}+\Delta\sigma'_{yy})/2$, distribution right before failure at 72 days for isothermal (left) and at 10 days for cooling (right) condition (tension positive).

Fig. 4.21 shows the induced effective mean, average value of $\Delta\sigma'_{xx}$ and $\Delta\sigma'_{yy}$, $(\Delta\sigma'_{xx}+\Delta\sigma'_{yy})/2$, stress distribution resulting from deformation under the in-situ stress, and fluid injection in both isothermal and non-isothermal condition. The net result is -1.7 MPa in isothermal and 2.4 MPa in non-isothermal at the fracture. In isothermal case, because of the injection, the fracture pressure is increased. And this increased pressure compresses the surface of the fracture and it causes negative stress around the joint. In cooling case, its value near the center of the joint is positive, indicating tension. This tension and the accompanying fracture opening, induce a compressive stress zone behind the tensile region. The tensile stress can be explained by the cooling effect of the joint

surface. This stress distribution is consistent with Fig. 4.17 in which the D_n for non-isothermal case is higher than the isothermal condition, especially at the center of the joint. Because of cooling, only high joint opening is initially observed in its center. However, with shear failure, the D_n substantially increases along the entire joint. Also, it can be seen in Fig. 4.21 that the induced effective mean stresses in other fracture segments are negative meaning that the surface is in compression and unaffected by cooling. Since Fig. 4.21 shows the mean effective stresses right after failure for isothermal and cooling conditions, we can see that the failure occurs earlier in the case than the isothermal case.
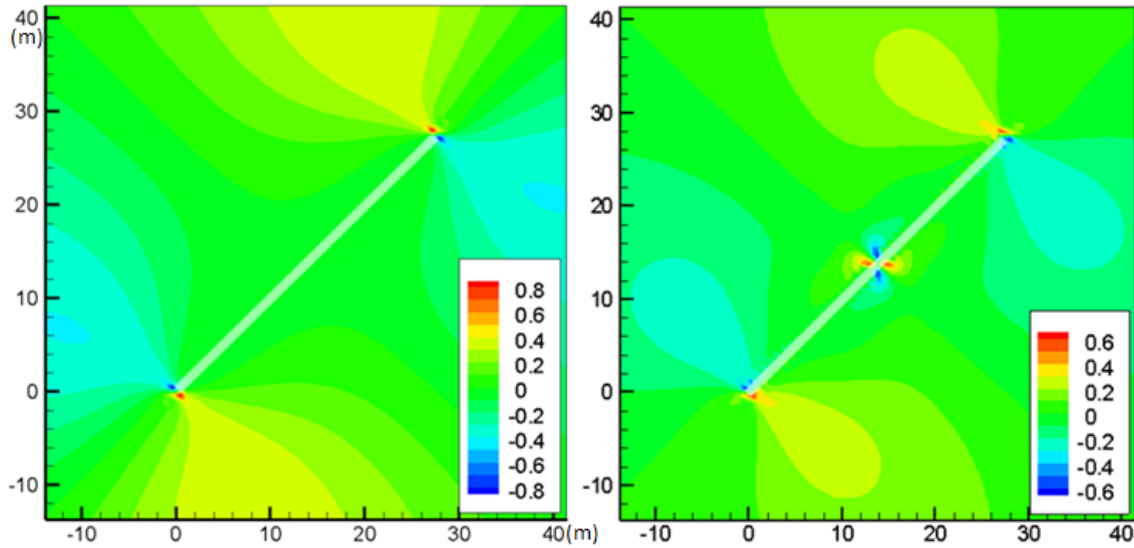
Fig. 4.22 Induced differential stress (MPa), $(\Delta\sigma'_{xx}-\Delta\sigma'_{yy})/2$, distribution right before failure at 72 days for isothermal (left) and at 10 days cooling (right) condition (tension positive).

For isothermal condition, the induced shear, $(\Delta\sigma'_{xx}-\Delta\sigma'_{yy})/2$, stress at injection location of the fracture is about 0 MPa (Fig. 4.22). For cooling condition, this stress at

injection location of the fracture is about 0.6 MPa. This tensile stress is caused by cooling effect which opens the fracture at the center, so these shear stresses are created while the fracture is opening. But these stresses are kinds of stress concentration shown at the tip. The differential stress in other area of this matrix is about 0 MPa. Therefore, the shear stress (3.5 MPa in this example) is caused by anisotropic in-situ stresses leading to shear deformation of the crack this case. When failure occurs, it is not because of additional shear stress change by injection, but because of the reduced amount of effective stress by injection. Therefore, if there were no shear stress on the joint, there will be no shear slip on the fracture caused by injection in this system.
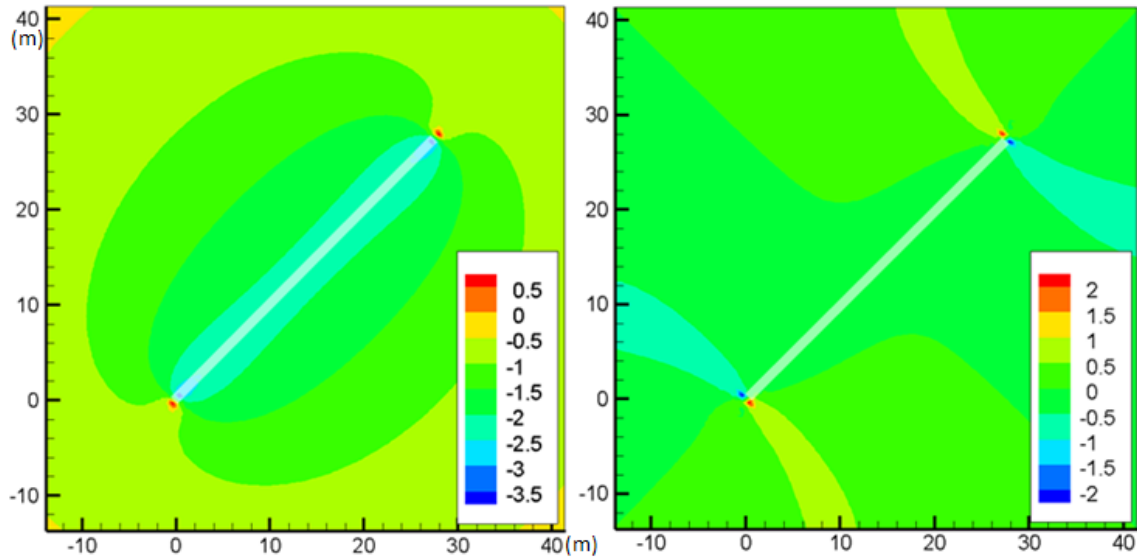
Fig. 4.23 Induced effective mean stress (MPa), $(\Delta\sigma'_{xx}+\Delta\sigma'_{yy})/2$ and induced differential stress, $(\Delta\sigma'_{xx}-\Delta\sigma'_{yy})/2$, distribution at 180 days for isothermal case (tension positive).
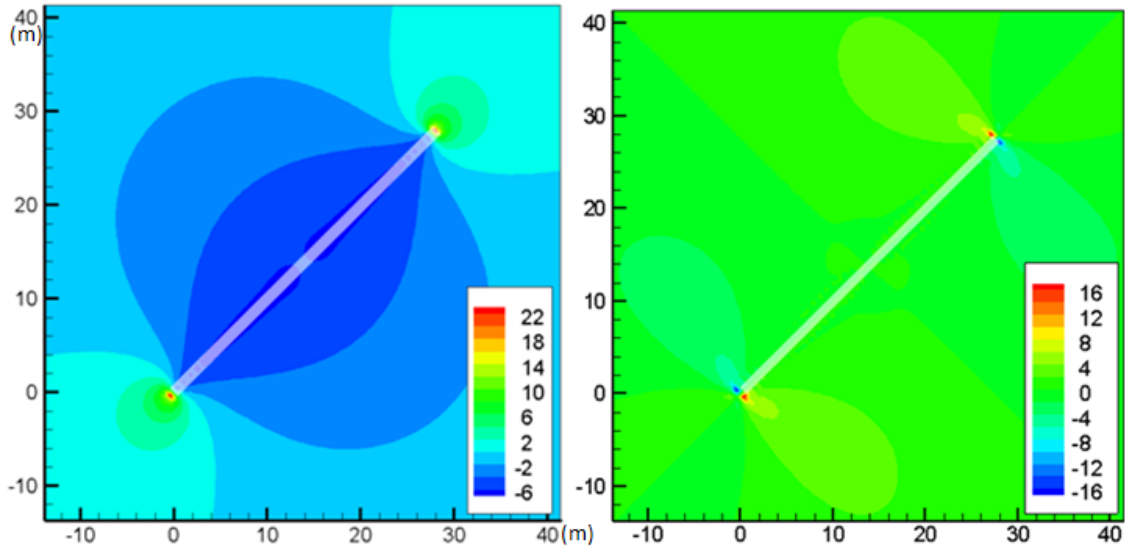
Fig. 4.24 Induced effective mean stress (MPa), $(\Delta\sigma'_{xx}+\Delta\sigma'_{yy})/2$ and induced differential stress, $(\Delta\sigma'_{xx}-\Delta\sigma'_{yy})/2$, distribution at 180 days for non-isothermal case (tension positive).

In Fig. 4.23, the induced effective mean stress along the fracture is negative because of constant injection. In Fig. 4.24, even though cool fluid is injected at the center of the fracture, the induced effective mean stress is compressive (negative), this is because the fracture is fully opened and the D_n is only increased by the injected fluid. Also, there are higher tensile stresses of about 22 MPa next to both tips of the joint, because of stress concentration. For the induced differential, $(\Delta\sigma'_{xx}-\Delta\sigma'_{yy})/2$, stress, there is no shear stress caused by injection of cooling even after failure.

In Fig. 4.12, the fracture pressure is increased quickly in response to the initial far-field stresses because of fluid compressibility (C_f) i.e., as the fluid in the fracture is quickly compressed it causes the pressure increase initially. The fluid compressibility value is from zero to 1.0 and the unit is "Pa^{-1}". In this simulation, the water compressibility value is $4.2 \times 10^{-10}\,Pa^{-1}$.
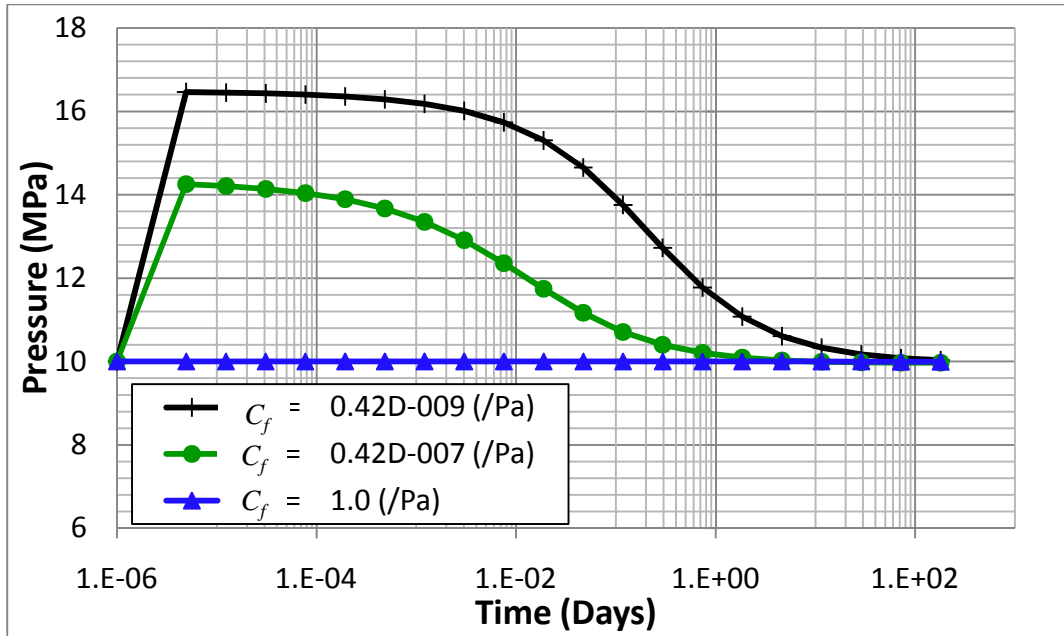
Fig. 4.25 Pressure variation in time at injection well with different C_f.

In this thesis, the fracture networks are filled with fluid from beginning. So, without injection, the pressures can be changed by in-situ stresses under non-equilibrium assumption. In this case, the zero injection example is used to see how the pressures are stabilized to the prescribed initial pressure, 10 MPa. According to Fig. 4.25, when the fluid compressibility (C_f) value is high, the fluid is more compressible and when this value is close to zero, the fluid is incompressible. When C_f is 1.0 Pa^{-1}, the pressure is almost constant with the initial pressure at 10 MPa because the fluid is compressed and absorbs the compression. However, in this example, because of lower fluid compressibility, there is a quick pressure increase initially. When the fluid compressibility is 4.2×10^{-10}, 4.2×10^{-8} and 1 Pa^{-1}, the initial fracture aperture is 0.56, 0.47 and 0.41 mm, respectively. Therefore, this fluid compressibility is the reason for initial pressure increase in fractures.

The possibility of permanent shear slip is checked with Mohr-Coulomb failure criterion. In addition, the amount of elastic shear displacement in this case is about 0.07 mm and this value is exactly 0.07 mm using analytical solution by Jaeger et al. (2007).

$$\sigma_n = \frac{1}{2}(\sigma_{xx} + \sigma_{yy}) + \frac{1}{2}(\sigma_{xx} - \sigma_{yy}) \times \cos 2\alpha_a + \sigma_{xy} \times \sin 2\alpha_a$$

$$\sigma_s = \frac{1}{2}(\sigma_{xx} - \sigma_{yy}) \times \sin 2\alpha_a - \sigma_{xy} \times \cos 2\alpha_a$$

.... (4.1)

α_a is the angle of the fracture from x-axis.

To compare the numerical solution to analytical solution, using same normal and shear stiffness given in Table 4.1 and put σ_{xx} is 30 MPa and change σ_{yy} from 30 MPa to 150 MPa, plot the shear displacement versus σ_{yy}.
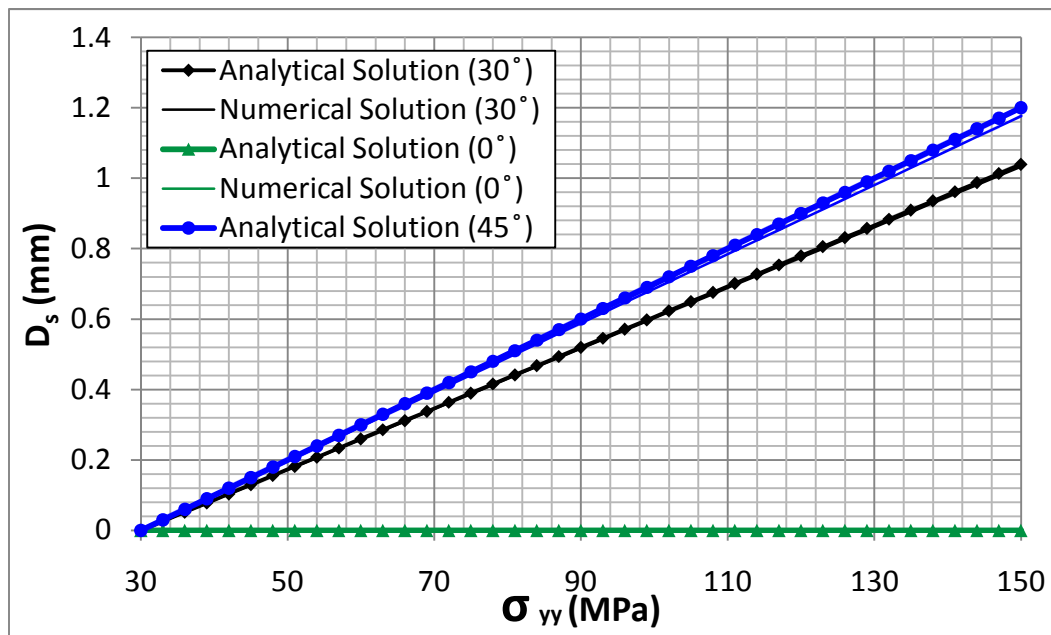
Fig. 4.26 Shear DD (D_s) changes by σ_{yy} with angle as 0°, 30° and 45° in both methods.

According to Fig. 4.26, the results from numerical solution and results from analytical solution are almost same.

4.3 Mechanisms of Shear Displacement

In previous section, the induced shear stress caused by injection was zero on the fracture surface and permanent shear slip on a single fracture was caused by under non-equilibrium condition. In this section, we investigate the shear movements in case of multiple fractures.
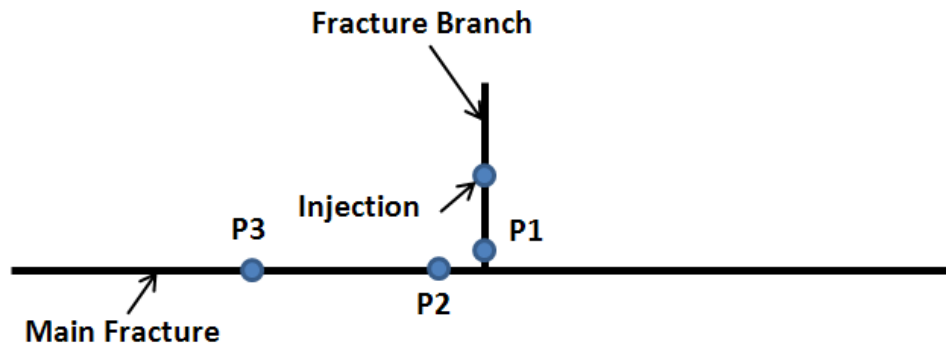
Fig. 4.27 A 20 m fracture with connected 90 degree 5 m fracture at the center. The fracture is modeled using 25 DD elements (P1, P2 and P3 are measure points).

According to Fig. 4.27, fluid is assumed to enter at the center of a secondary fracture at a flow rate, 1.5×10^{-8} m^3/sec. And initial pressure is 27 MPa, initial far-field stress is 30 MPa (just used for initial normal displacement set up) and operation time is 360 days. The fracture pressure, normal displacement and shear displacement changes when the fracture is fully opened at the injection well.
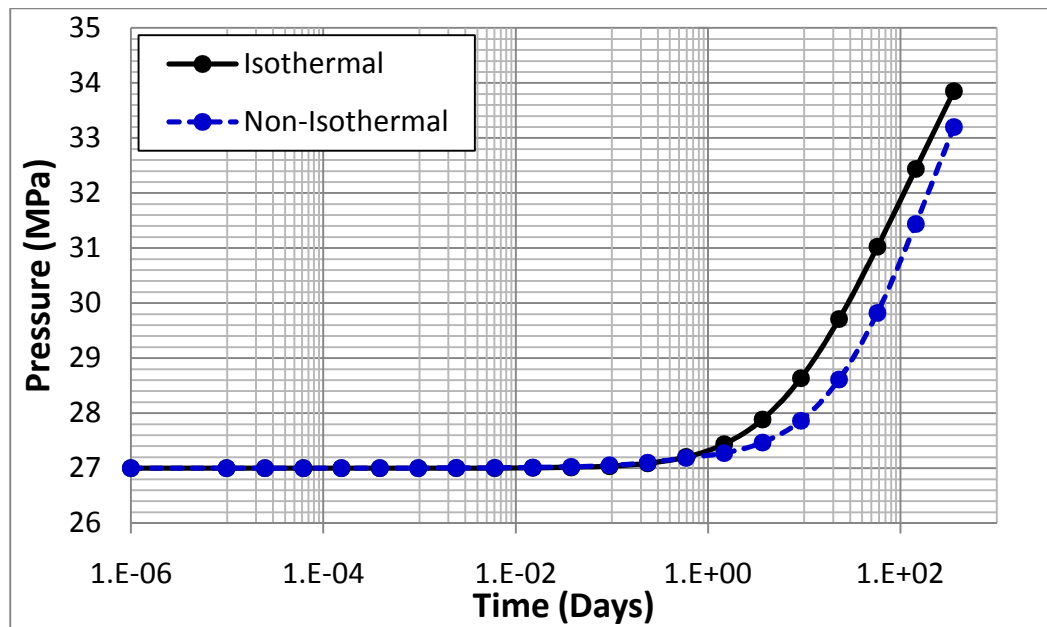
Fig. 4.28 Fracture pressure variation with time at injection well for isothermal and non-isothermal conditions.
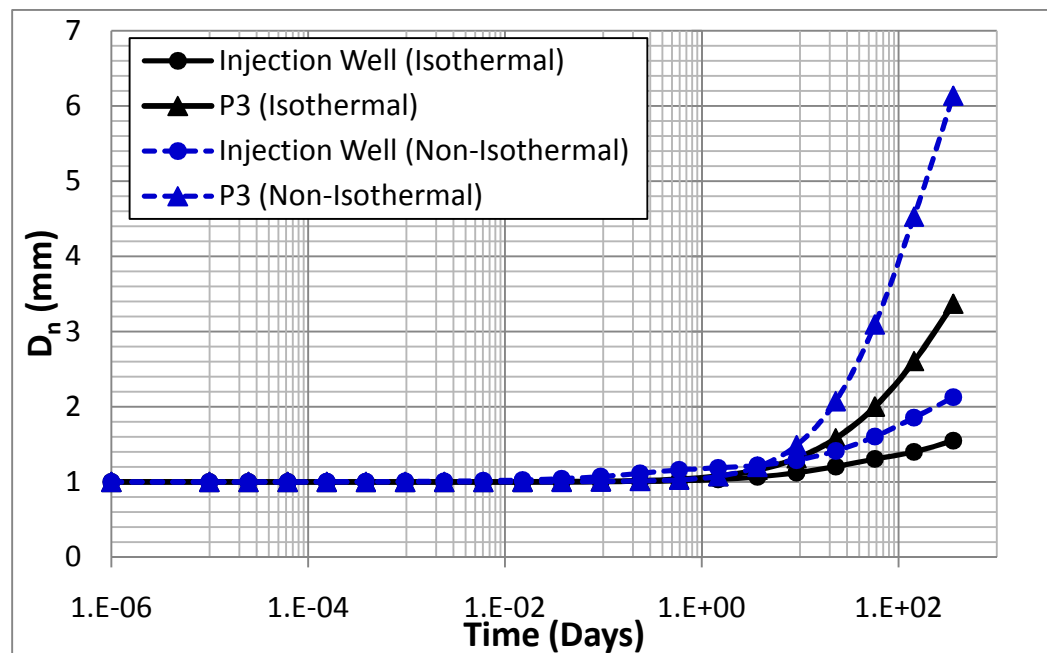
Fig. 4.29 Normal DD (fracture aperture) change with time at injection well and P3 (Fig. 4.27) for isothermal/non-isothermal conditions.

The fracture pressure increases by injection and the pressure in the cooling case is slightly lower in Fig. 4.28. The fracture pressure reaches 33 MPa in both isothermal and cooling at the end of operation. Fig. 4.29 shows that the fracture aperture of the main fracture is bigger than the fracture aperture of the fracture branch. The reason for this is that the main fracture is 4 times longer, so under a similar fracture pressure it opens more. Also, the fracture aperture in the cooling case is bigger than the one in isothermal case because of cooling effect.
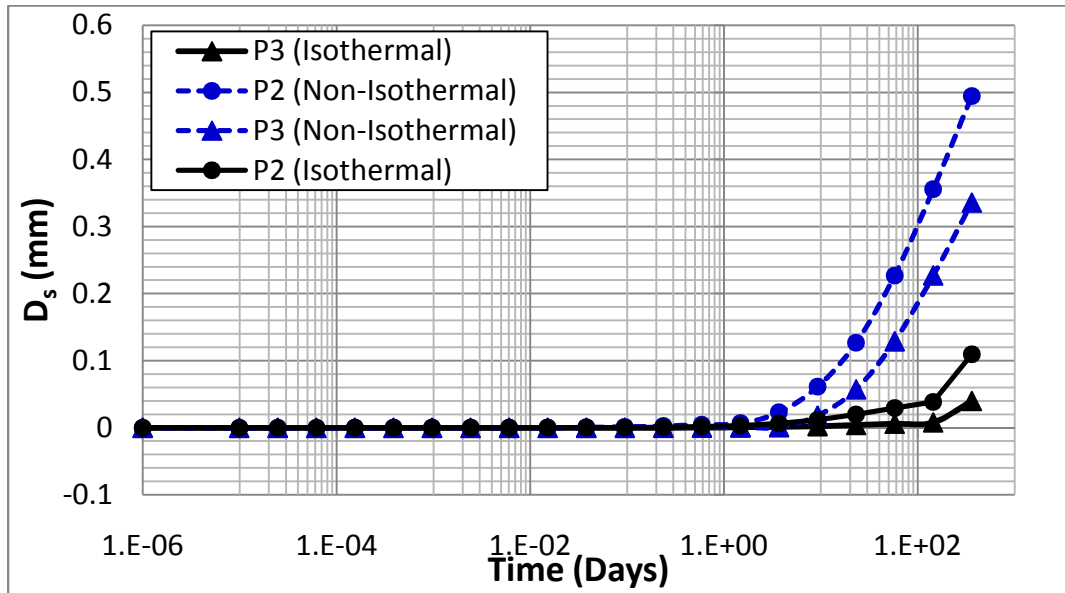
Fig. 4.30 Shear DD (D_s) change with time at P2 and P3 (Fig. 4.27) for isothermal/non-isothermal conditions.

In the isothermal case, the fracture branch is fully opened at the 19th time (144 days) step and in cooling case the branch is opened at the 15th time (10 days) step in Fig. 4.30. And the shear slips at P2 and P3 occur at the same time step in both conditions. It means that this shear slip in main fracture is caused by the opening of fracture branch.
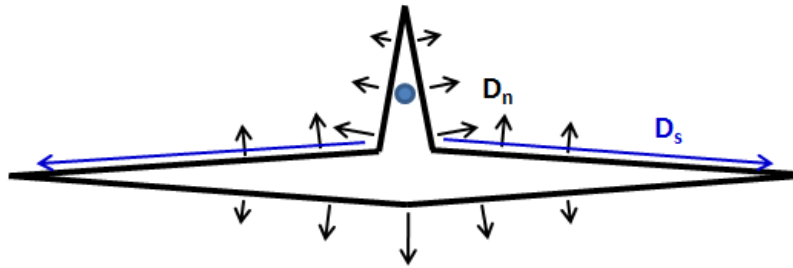
Fig. 4.31 Mechanism of normal and shear displacement generation.

Fig. 4.31 shows how the normal and shear displacement are generated for intersecting cracks. Previously, under non-equilibrium condition, the fracture is permanently slipped by far-field (in-situ) stress. However, for equilibrium condition, there is no shear slip under the initial stress.
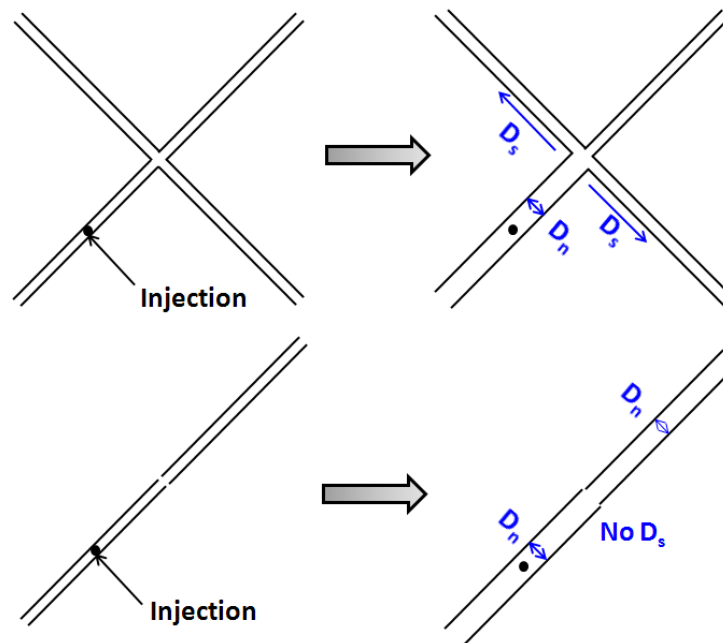
Fig. 4.32 Mechanism of normal and shear displacement generation in regular fracture network.

Fig. 4.32 illustrates no shear slip in single fracture under equilibrium with in-situ stresses. However, in a fracture network, because of the fracture deformation and interaction, shear displacement is generated by injection or production.
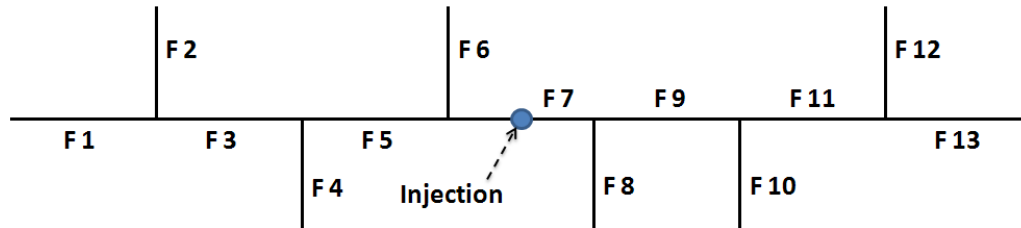
Fig. 4.33 A 35 m fracture with 5 m perpendicular fractures at seven locations. The fracture is modeled using 53 DD elements under equilibrium condition.

In this example (Fig. 4.33), we investigate the mechanism of shear displacement in irregularly connected fracture network under equilibrium condition. There is fluid injection at the center of the main fracture and it causes fracture deformation in normal and shear because of the opening of the secondary cracks as they are pressurized.
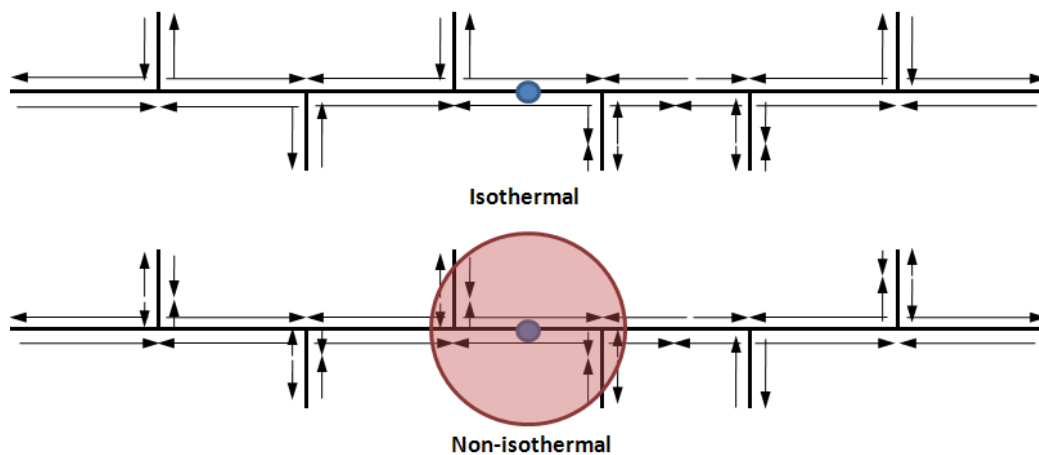
Fig. 4.34 Mechanism of shear displacement generation in irregular fracture network with isothermal (upper)/ cooling (lower) injection.

According to Fig. 4.34, in the main fractures network at the center (F1, F3, F5, F7, F9, F11 and F13), the shear displacements are caused by normal displacement in fracture branches (F2, F4, F6, F8, F10 and F12) due to injection. For cooling, the shear displacements in fracture branches are little bit different because of thermal effect, but the differences in D_s are negligible. So, in both isothermal and cooling cases, the pattern of D_s is similar.
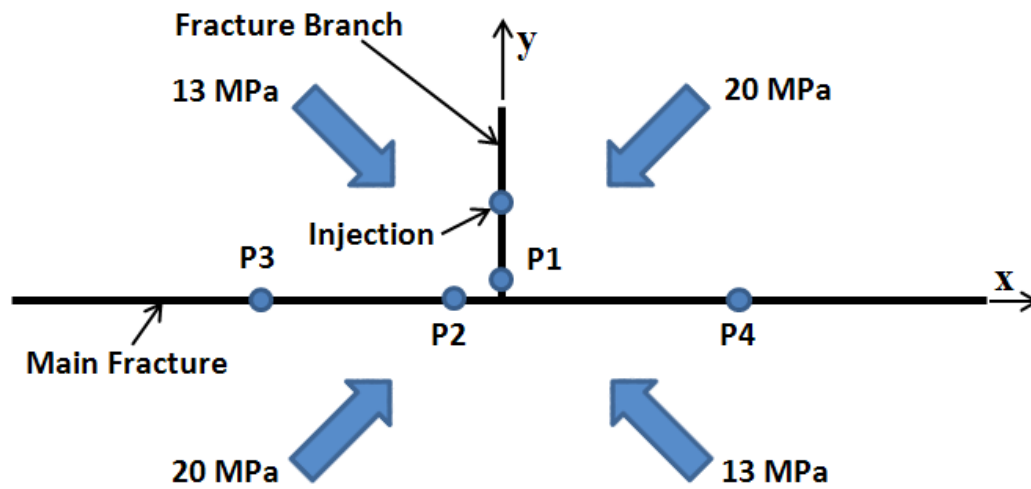
Fig. 4.35 A 20 m fracture with connected 90 degree 5 m fracture at the center. The fracture is modeled using 25 DD elements under anisotropic (45˚, 135˚, 225˚ and 315˚) in-situ stress (P1, P2, P3 and P4 are measure points).

However, under anisotropic in-situ stresses, the shear displacements in fracture segments are different. Since the anisotropic in-situ stresses, initially generates shear displacement on all fractures. Fig. 4.35 shows the fracture network with anisotropic in-situ stresses.
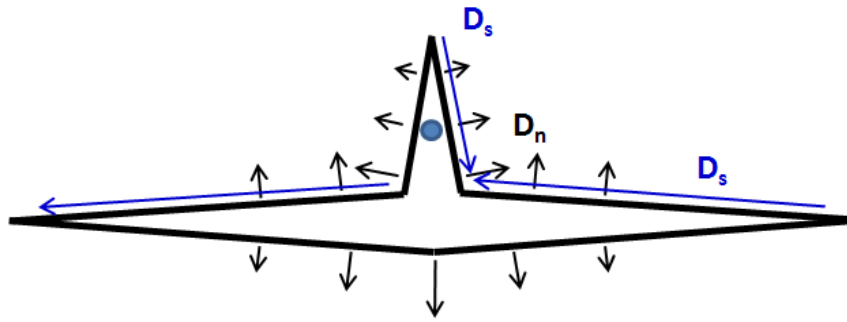
Fig. 4.36 Mechanism of initial normal and shear displacement generation under anisotropic in-situ stresses.

Due to higher in-situ stress anisotropy (13 vs. 20 MPa), there are shear displacements (blue arrows) initially (Fig. 4.36). Comparing Fig. 4.36 to Fig. 4.31, there is shear displacement in fracture branch in this case because of in-situ shear stress.
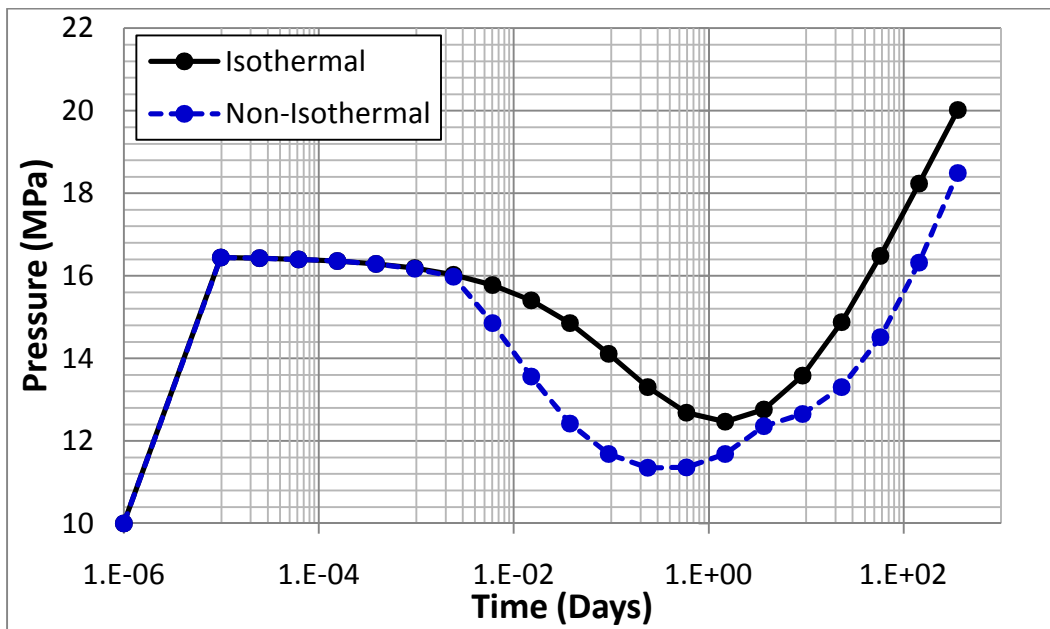
Fig. 4.37 Fracture pressure variation with time under in-situ stress at injection well for isothermal and non-isothermal conditions.
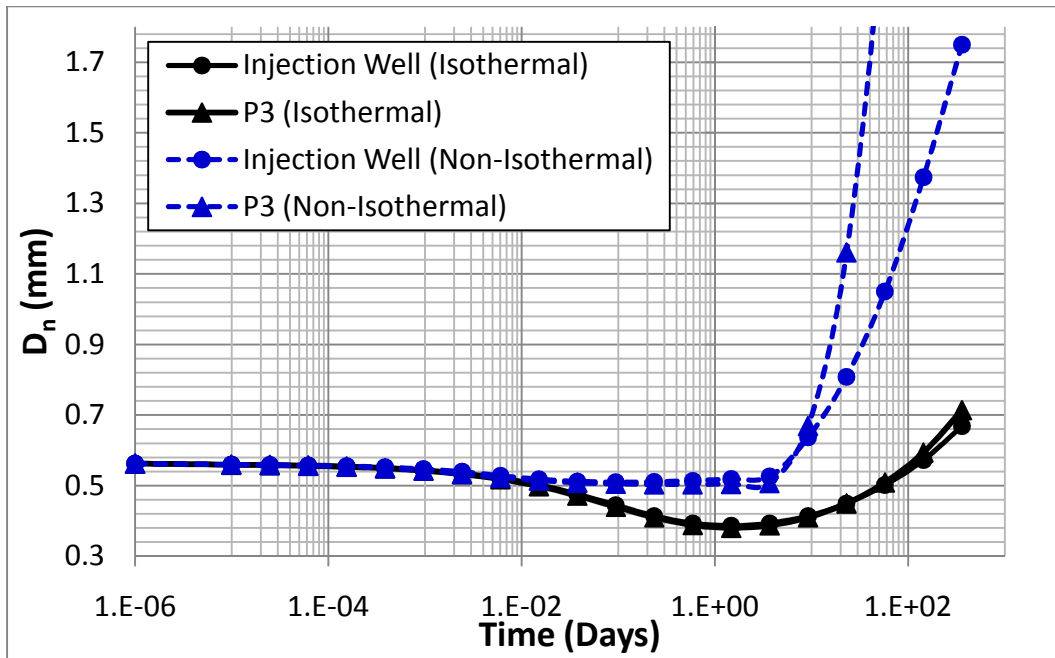
Fig. 4.38 Normal DD, D_n (fracture aperture) change with time at injection well and P3 (Fig. 4.35) for isothermal/non-isothermal conditions.

The pressure and fracture aperture changes for non-equilibrium condition was studied in Section 4.2. After a quick pressure increase due to fluid compressibility, the fracture pressure and fracture aperture decreased with time. Later when injection fluid was enough to increase the fracture pressure and apertures increased simoultaneously. Fig. 4.37 and Fig. 4.38 show a same pattern in fracture pressure and aperture changes (compare to Fig. 4.12 and Fig. 4.13). Fracture pressure in isothermal and cooling cases are uniform in all fracture segments. In cooling operation, the fracture aperture at P3 reaches about 6.5 mm while at injection point, it is about 1.8 mm.
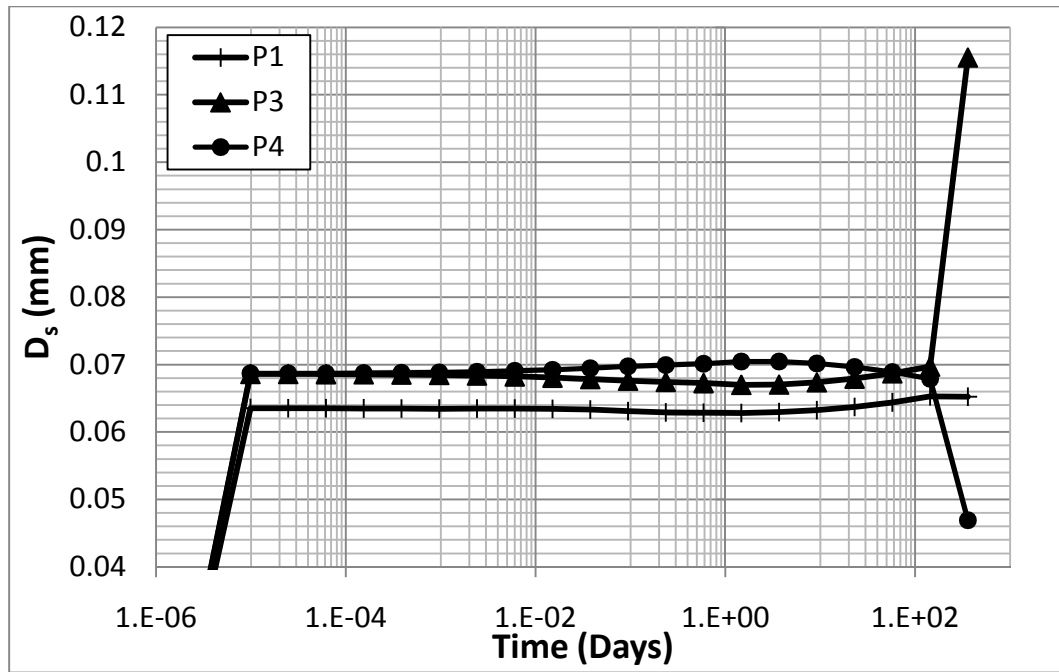
Fig. 4.39 Shear DD (D_s) change with time at P1, P2 and P4 (Fig. 4.35) for isothermal conditions (Initially, $D_s = 0$).

When the upper surface of fracture moves left or the right-hand side surface of fracture moves up, shear displacement discontinuity (D_s) are considered positive. In Fig. 4.39, D_s at P1 is its absolute value (actually, D_s at P1 has negative values). At point P1 (fracture branch), the injection does not affect shear displacement at this point so it does not change significantly (just little changes caused by pressure changes in main fracture). At P3 and P4, there are initial shear displacements about 0.68 mm caused by the anisotropic in-situ stresses under non-equilibrium condition. And D_s at P3 is decreased by pressure decreases at fracture branch and it starts to increase by pressure increase due to injection, and when the shear strength is overcome by shear stress on this segment, permanent shear slip occurs (at the end of time step). At P4, there is exactly opposite situation. The D_s is increased (because of upper surface movement direction) by pressure

decrease at fracture branch and with time it starts to decrease by injection. At the end of simulation, there is permanent shear slip caused by injection.
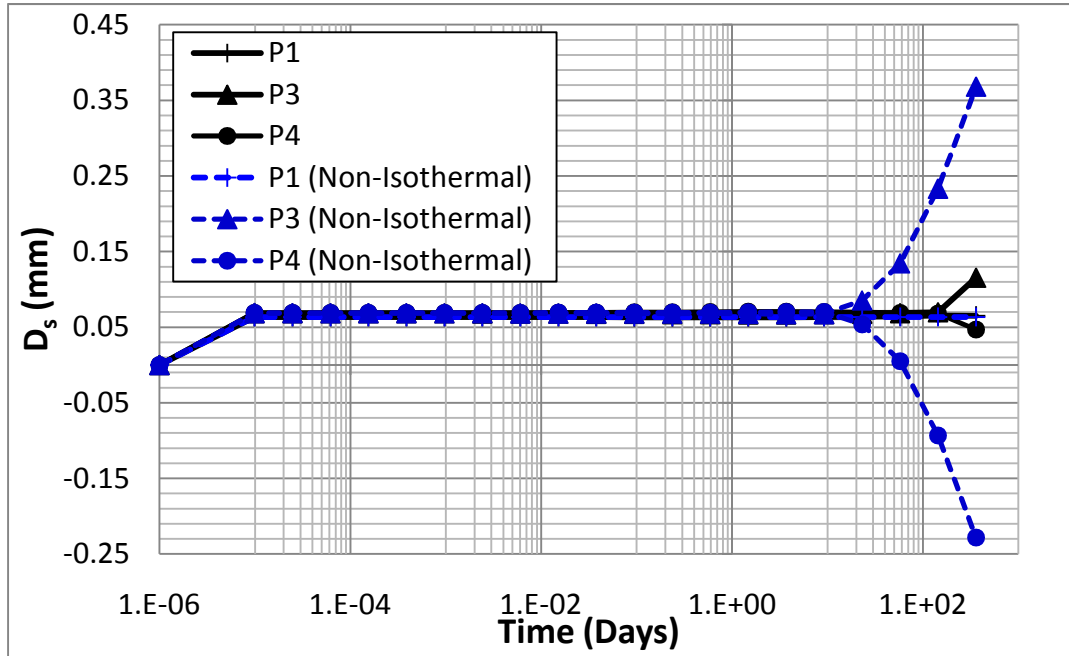
Fig. 4.40 Shear DD (D_s) change with time at P1, P2 and P4 (Fig. 4.35) for isothermal/cooling conditions.

According to Fig. 4.40, in cooling operation, there is an early permanent shear slip at 16th time step. Because of tensile stress by cold temperature, the fracture aperture at fracture branch opens faster than for the isothermal case, and causes early shear failure in main fracture. At P1, since the injection does not affect any shear displacement in this location, there is no significant difference between the shear displacement in isothermal and cooling cases. This result at P1 shows that the main cause of permanent shear slip in the main fracture is the opening of a secondary fracture due to injection.
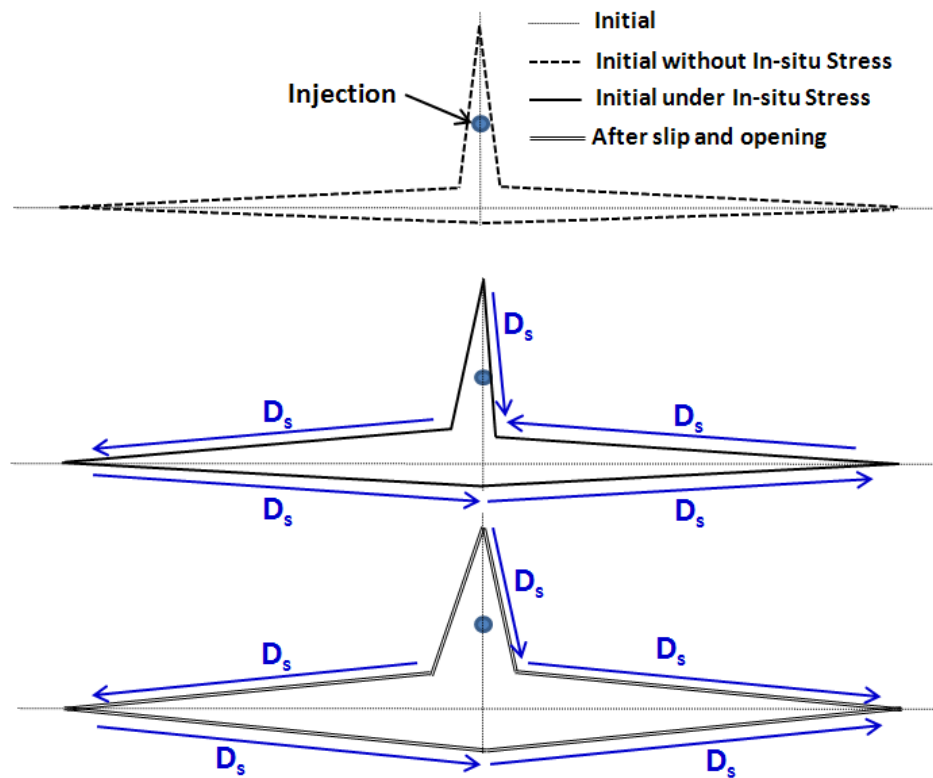
Fig. 4.41 Mechanism of normal and shear displacement generation under anisotropic in-situ stress.

This exaggerated illustration (Fig. 4.41) shows how the shape of the fracture network is changed. When putting anisotropic in-situ stresses (Fig. 4.35), the fracture is deformed initially and with constant injecting the branch fracture is fully opened causing shear slip on the main fracture.

4.4 Single Fracture with Injection/Production
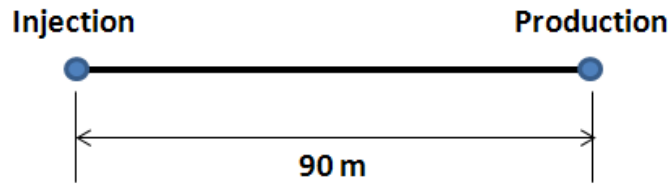
Fig. 4.42 A 90 m fracture with 30 DD elements with injection and production at each end of the fracture.

In this case study (Fig. 4.42), fluid is injected and extracted for 180 days with 2.0 $\times$ 10^{-3} m^3/sec and 1.9999 $\times$ 10^{-3} m^3/sec flow rate so the injection rate is slightly higher than production rate. In cooling operation, the fluid temperature is 300 K (reservoir temperature is 420 K). Other input parameters are same with Table 4.1 and Table 4.2.
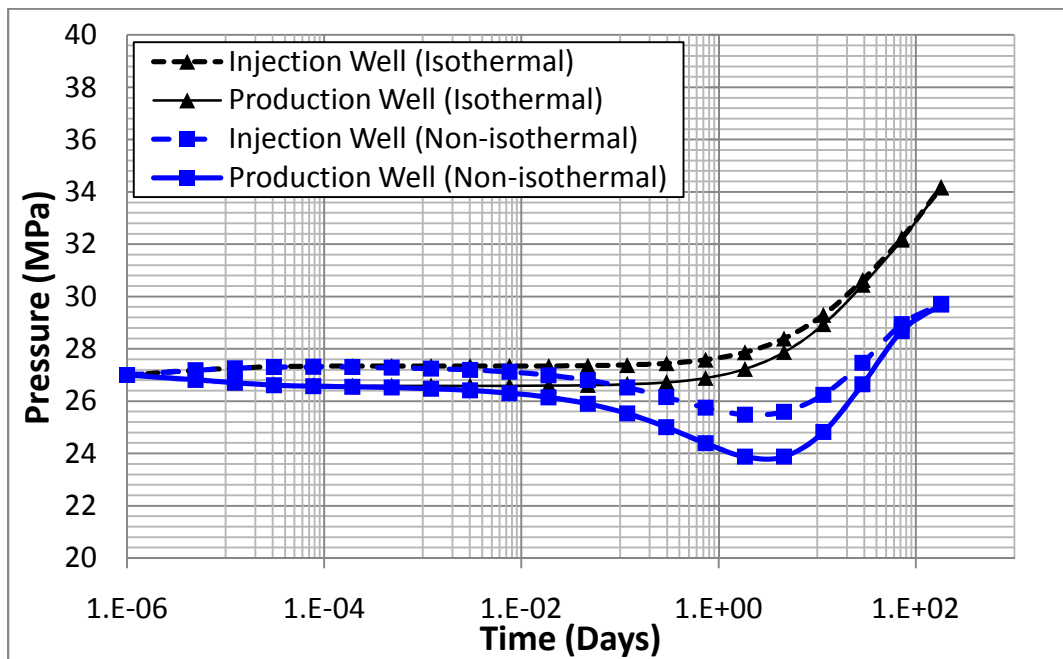
Fig. 4.43 Fracture pressure variation with time at injection/production well for isothermal and non-isothermal conditions.

According to Fig. 4.43, initially the pressure at injection well is higher than the pressure at production well. In isothermal operation, the pressure starts to increase after few hours of operations, but for the cooling case, the pressure is decreased first in early time step and it starts to increase after 2 days of operation because of slightly higher injection rate. When injecting cold water into the system, the pressure by the fluid itself is lower than isothermal operation. At the end of time step, the pressure gradients are decreased because when the cooling effect has fully developed at the end of the 19th time step, the fracture aperture and it does increase more because of higher injection rate. So, the initially small pressure gradients increase soon by injection.
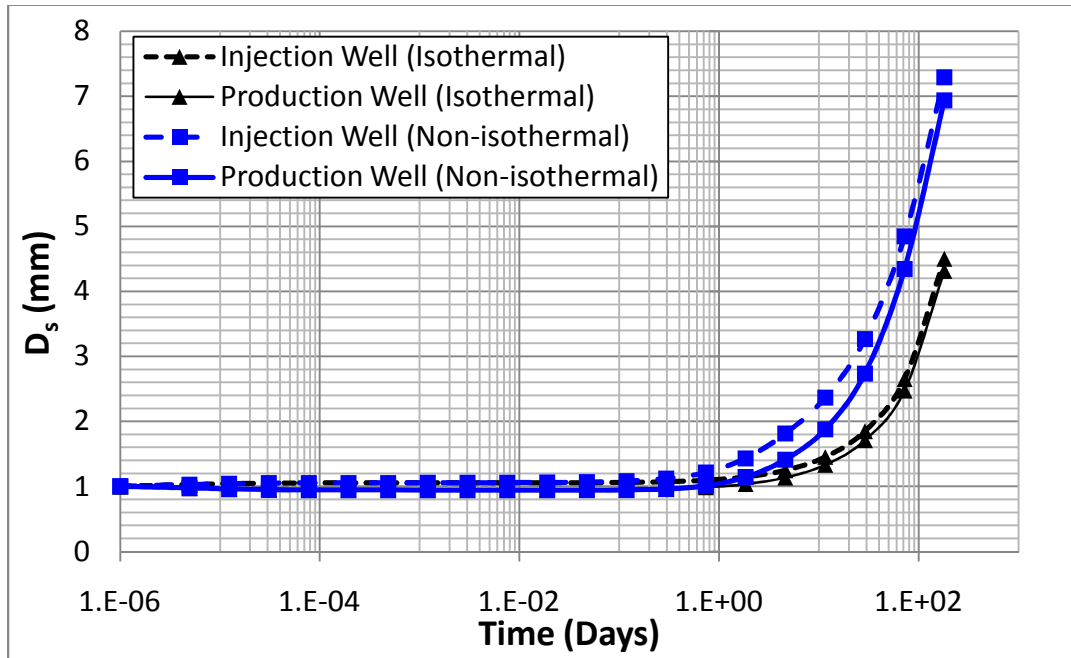
Fig. 4.44 Normal DD, D_n (fracture aperture) change with time at injection and production well for isothermal/non-isothermal conditions.

In Fig. 4.44, while cooling, the fracture apertures in both wells are bigger than those in isothermal operation because the cold fluid causes opening of the fracture by induced tension. The cooling effect is visible within 1 day of operation in this figure. In addition, the apertures at injection well are higher than at production well in isothermal and cooling cases.
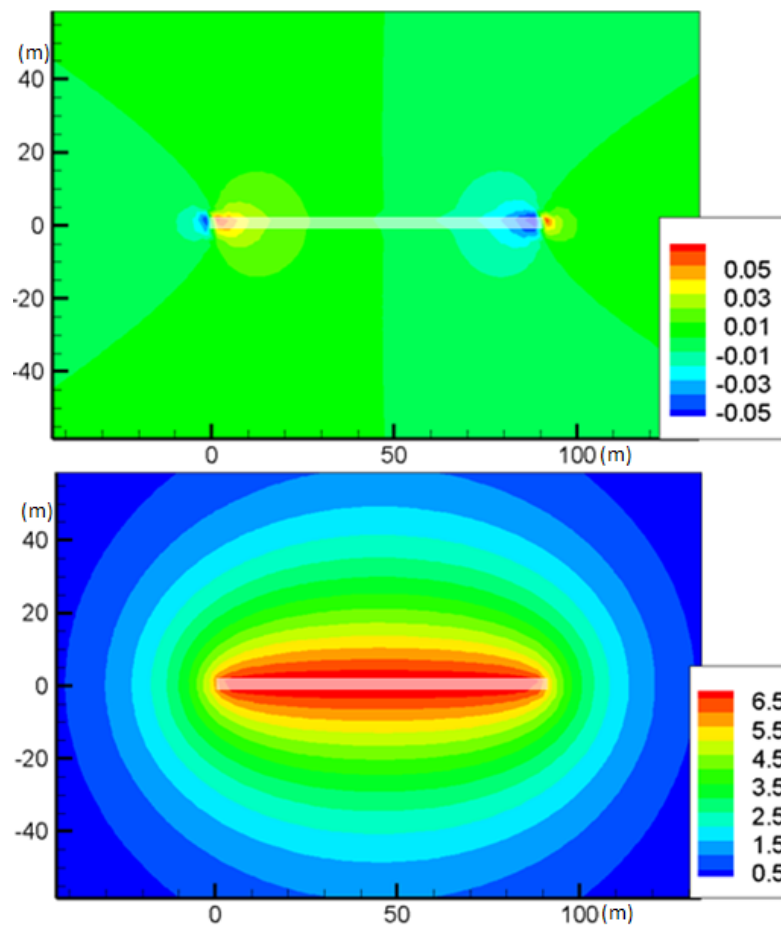
Fig. 4.45 Induced pressure, Δp (MPa) distribution after 10 (up) and 180 (lower) days of injection and production operation in isothermal condition.

In Fig. 4.45, after 10 days simulation, the induced pressure around the injection well is positive and the pressure around the production well is negative because of injection and production. And after 180 days operation, the pressure around the fracture reaches about 6.5 MPa because of slightly higher injection rate. The induced pressure at the end of the injection fracture segment has negative value and the induced pressure at the production fracture segment has positive value because of stress concentration. But these are present only in early time steps and disappeared by pressure increase.
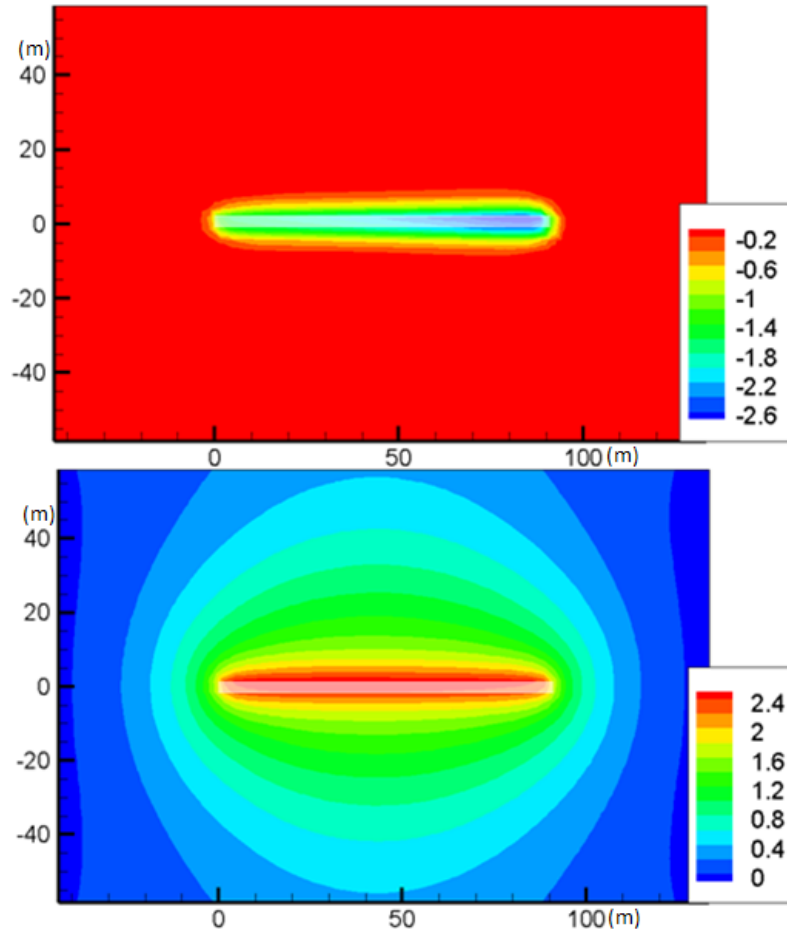
Fig. 4.46 Induced pressure, Δp (MPa) distribution after 2 (top) and 180 (lower) days of injection and production operation in cooling condition.

In cooling condition, the pressure is decreased by cold fluid itself so the pressures in matrix are decreased simultaneously. And the lowest pressure reaches about 24 MPa (-3 MPa induced pressure) in fracture (Fig. 4.46). After 2 days of operation, the pressure starts to increase (Fig. 4.43) by higher injection rate and reached 2.4 MPa at the end.
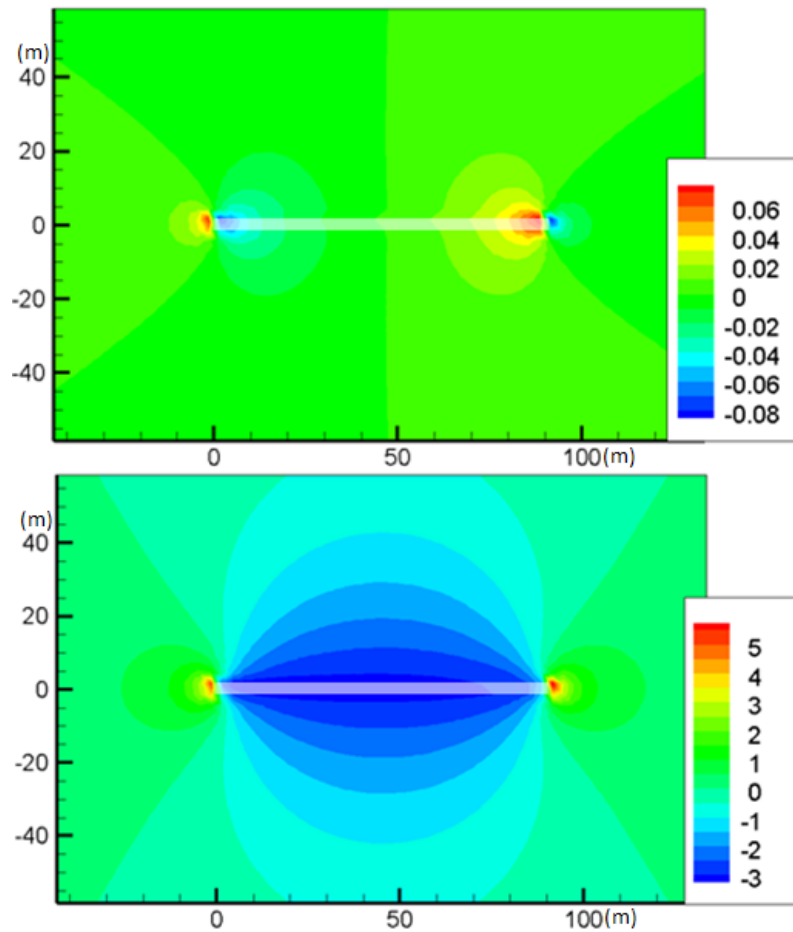
Fig. 4.47 Induced effective mean stress in rock matrix (MPa), $(\Delta\sigma'_{xx}+\Delta\sigma'_{yy})/2$ after 10 (top) and 180 days operation for isothermal (tension positive).

According to Fig. 4.47, after 10 days, the induced effective mean stress near the injection well is compressive (negative) because of pressure due to injection. On the

other hand, this value is positive at production well because of tensile stress due to production. At the end of operation, the induced effective mean stress reaches about - 3.1 MPa because of pressure increase and there are higher tensile stresses of about 5 MPa next to both tips of the joint due to strain compatibility. Comparing to Fig. 4.45, the pressure and this stress, $(\Delta\sigma'_{xx}+\Delta\sigma'_{yy})/2$ is distributed similarly in early time. However, at the end of simulation, there are stress concentration effects at the tips, but this feature disappears with time and the pressure spreads out evenly to the field.
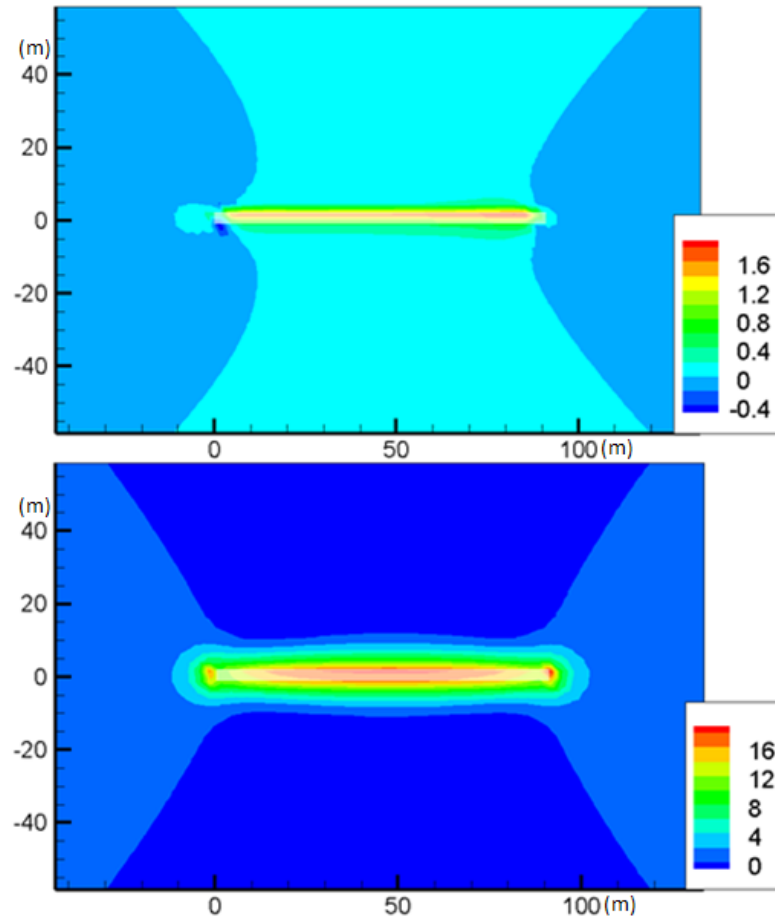
Fig. 4.48 Induced effective mean stress in rock matrix (MPa), $(\Delta\sigma'_{xx}+\Delta\sigma'_{yy})/2$ after 2 (top) and 180 days operation for cooling.

For cooling injection, the induced effective mean stress are higher around the fracture early on and at the end of this operation, the higher value is reached 17 MPa which is generated by shrinkage of fracture surfaces due to cooling operation (Fig. 4.48). Comparing to Fig. 4.21, the higher tensile stress affects along the fracture while in Fig. 4.21 (single fracture case), the tensile stress affects just an area in the vicinity of injection well. The following figure for temperature distribution shows the reason of this difference.
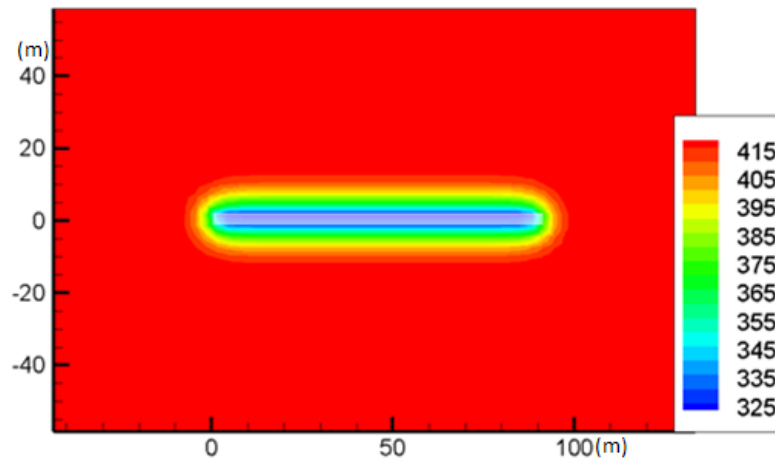
Fig. 4.49 Temperature (K) distribution after 180 days operation.

In this case, there is both injection and extraction. So, when injecting cold fluid into system, the cold fluid flows in the fracture network and is extracted at the production well while in Section 4.2, the temperature spreads out to field evenly in all directions conduction (Fig. 4.49).

5. MODEL APPLICATIONS TO STIMULATION

INJECTION/EXTRACTION; INDUCED SEISMICITY

In this section, the fully coupled displacement discontinuity method (DDM) is used to analyze the induced pressure, temperature and stress in the reservoir matrix under anisotropic in-situ stresses conditions and to simulate injection/extraction in irregular fracture networks to investigate flow channels evolution. Finally, the pressures and fracture apertures under equilibrium and non-equilibrium conditions will be compared in regular fracture network.

5.1 Irregular Fracture Network with Regular Pattern
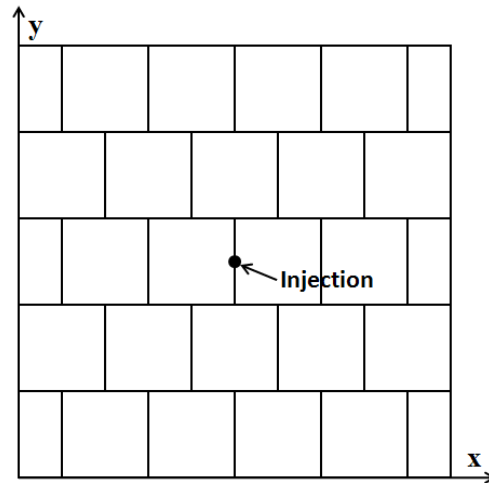
Fig. 5.1 Irregular fracture network having 129 fracture segments over an area of 150×150 (m^2).

In this study, the fracture pressure, temperature, aperture, and conductivity changes in fracture network subjected to and anisotropic in-situ stresses are considered under non-equilibrium condition.
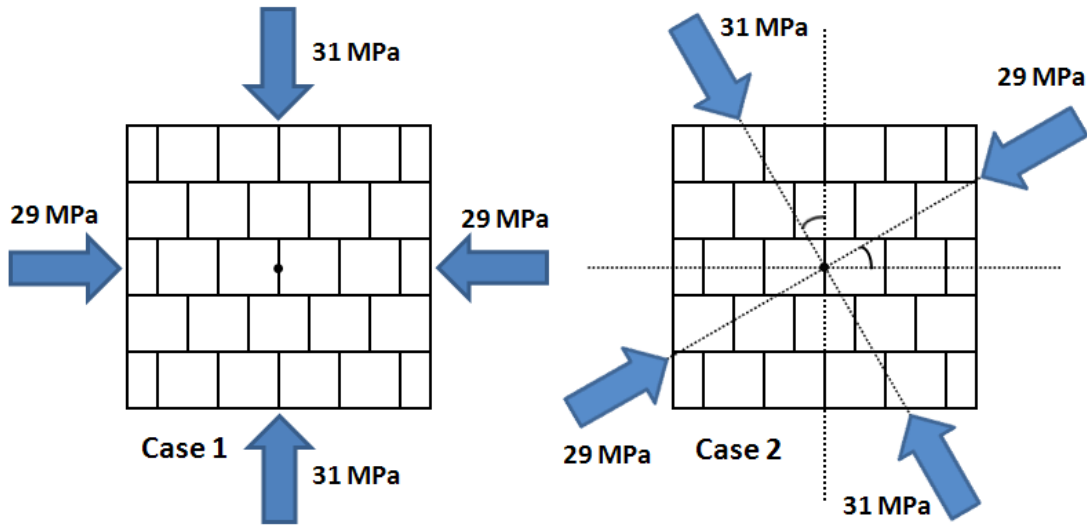
Fig. 5.2 Anisotropy field stresses (31 MPa, 29 MPa) with different angles (0°, 30°).

Initially, because of fluid compressibility, the fracture pressure will increase to 27 MPa, higher than initial pressure, and it will then decrease with time until fracture pressure is increased by the injection near the end of simulation time. The resulting pressure, temperature and normal displacements (fracture permeability) will be different for both cases in Fig. 5.2. In Fig. 5.1, the fluid is injected at the center of fracture network with rate, 2×10^{-5} m^3/sec and cooling temperature, 120 K. The geometry and loading condition for eth two cases are show in Fig. 5.1 and 5.2. Other parameters are listed in Table 4.1 and Table 4.2.
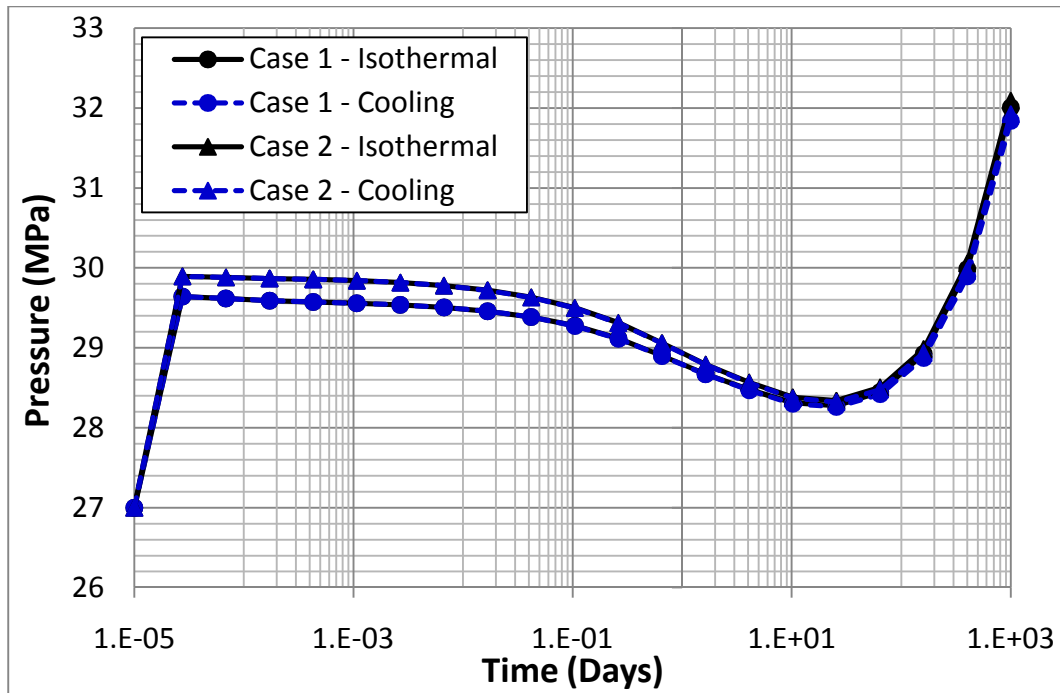
Fig. 5.3 Pressure variation in time at injection well with Case 1 and Case 2 in isothermal and cooling condition.

According to Fig. 5.3, the pressure decreases with time until the injection rates are enough to increase the fracture pressure (after 25 days injection). However, initially the pressures in Case 2 are higher than in Case 1. When comparing Case 1 and Case 2, the initial pressure in Case 1 is about 29.64 MPa while the initial pressure in Case 2 is about 29.89 MPa. The fracture pressure in Case 1 is slightly lower than the pressure in Case 2. In this example, the injection well is located a fracture which is parallel to y-direction. And in Case 1, this fracture is compressed at the beginning by 31 MPa in y-direction and by 29 MPa in x-direction while in Case 2 the fractures are compressed by about 30.5 MPa for horizontal fracture elements and 29.5 MPa for vertical fracture elements.
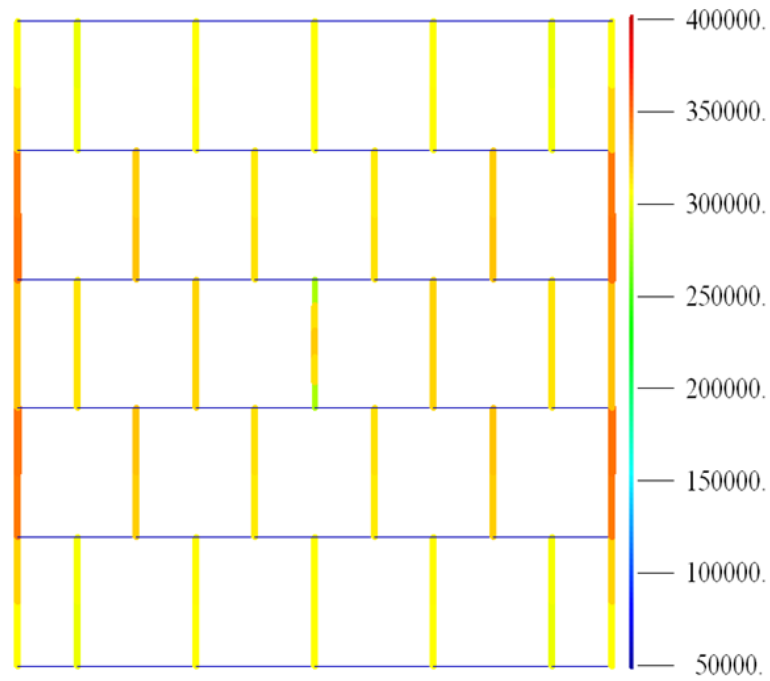
Fig. 5.4 Permeability (Darcy) distribution in fractures after 1000 days injection in isothermal condition (Case 1).

According to Fig. 5.4, the fracture apertures for the vertical set are larger than the apertures for the horizontal set because of lower in-situ stress in x-direction (29 MPa). So that the fracture permeability (where, $k_f = w_f^2/12$, Witherspoon et al., 1980) in fractures varies due to their angles, so the vertical fractures have higher permeability and the horizontal fractures have lower permeability resulting in flow channeling in the vertical direction.
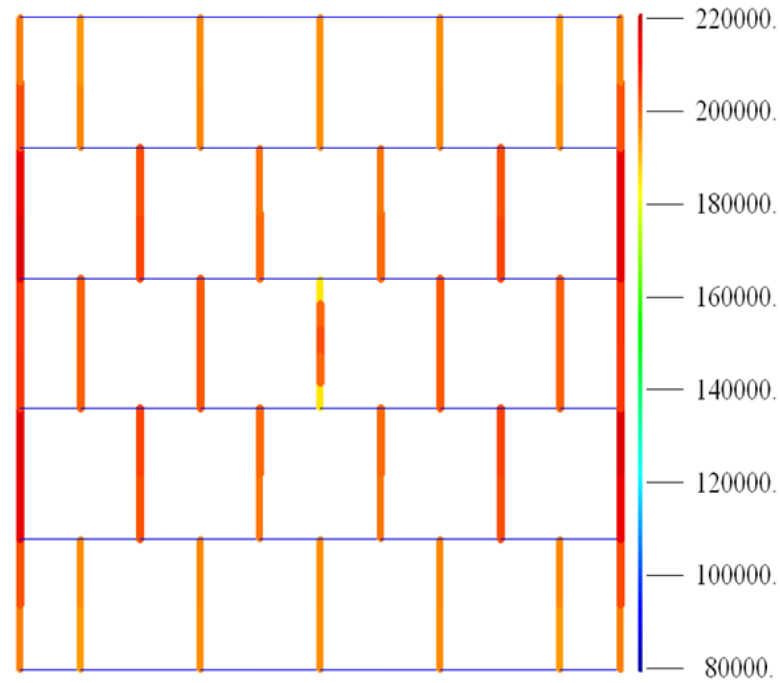
Fig. 5.5 Permeability (Darcy) distribution in fracture after 1000 days injection in isothermal condition (Case 2).

In Fig. 5.5, the pattern of permeability distribution is similar to Case 1, but it is more regularly distributed than Case 1 and horizontal fractures experience higher permeability than in Case 1. The fracture permeability ranges from 80,000 ~ 220,000 Darcy (D_n: 0.8 ~ 1.2 mm) and falls within the range of Case 1, 50,000 Darcy ~ 400,000 Darcy (D_n: 0.6 ~ 1.4 mm). This variable permeability is caused by different directions of the in-situ stresses for each case. When the in-situ stresses compress the fracture network with 45˚ rotation in counter-clockwise, the fracture permeability ranges from 124,000 Darcy to 140,000 Darcy.
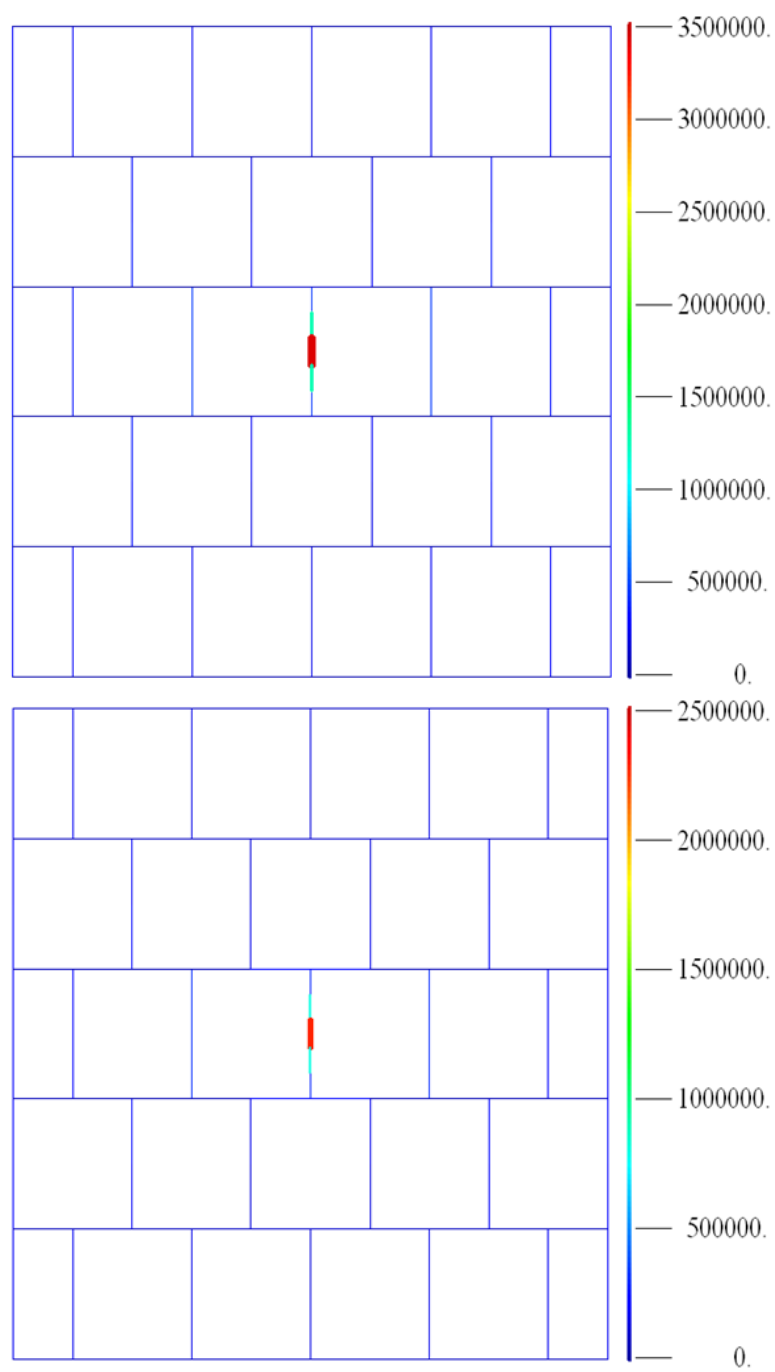
Fig. 5.6 Permeability (Darcy) distribution in fracture after 1000 days injection in cooling (top: Case 1, lower: Case 2).
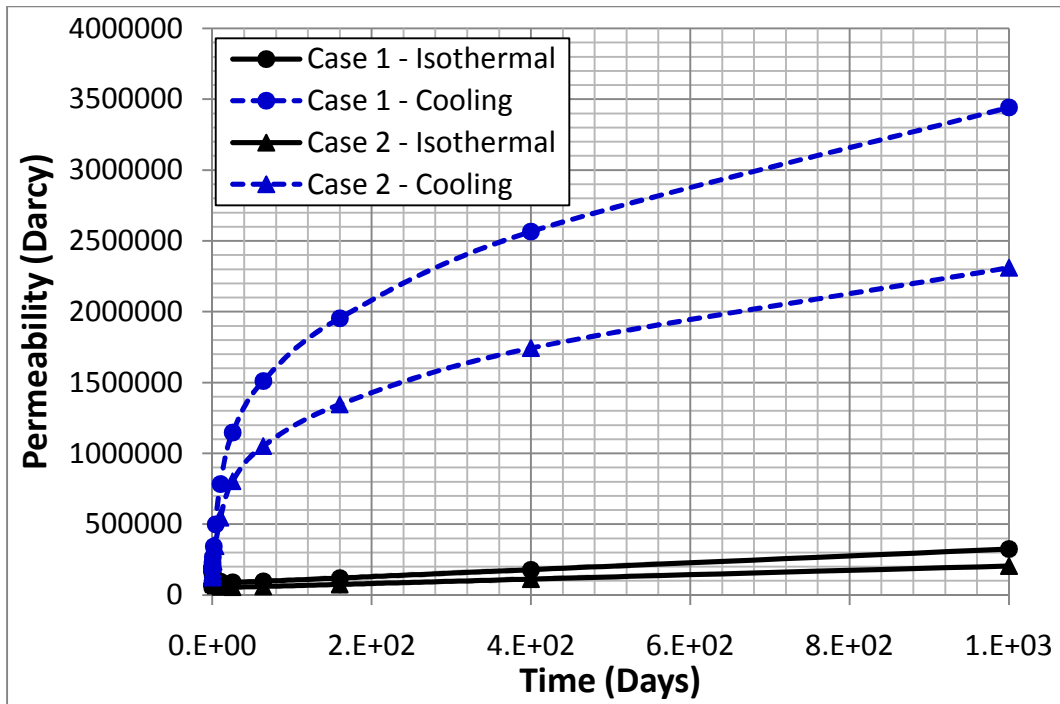
Fig. 5.7 Permeability (Darcy) change with time in fracture at injection well in isothermal and cooling cases.

According to Fig. 5.8, the cold temperature spreads out only in the vicinity of the injection well fracture because of there is no extraction. Due to cooling, in Case 1 and Case 2, the permeability of fractures are noticeably higher at the injection well and in horizontal fractures at the top and bottom of the injection point (Fig. 5.6). In other areas, the fracture permeabiliy is under 500,000 Darcy. Since the lower in-situ stress compresses the fracture in x-direction, the fracture permeability in Case 1 is higher than Case 2 from the start (Fig. 5.7).
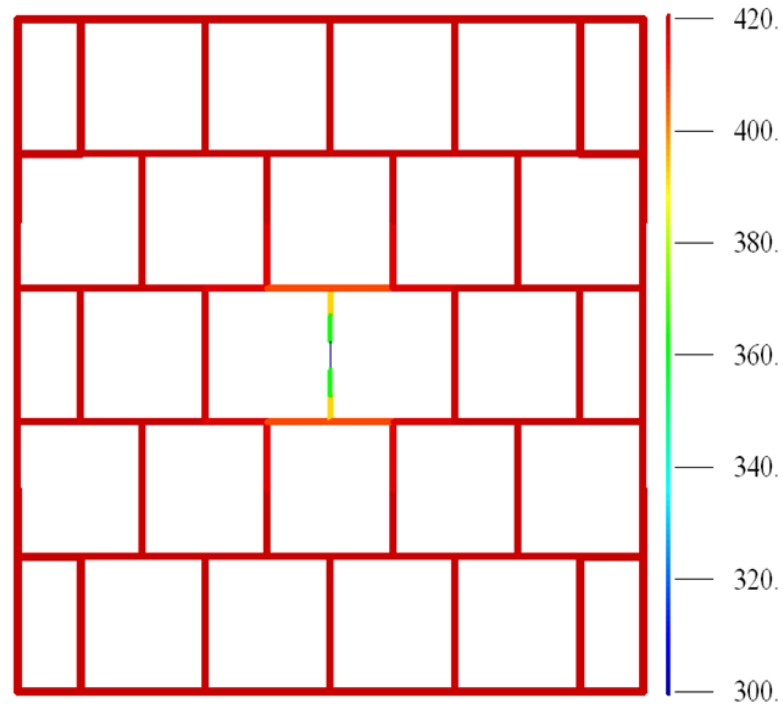
Fig. 5.8 Temperature (K) distribution in fracture after 1000 days injection in cooling.

5.2 Irregular Fracture Network

In this case study, we simulate heat extraction from a real fracture network that consists of irregular distribution of fractures (Fig. 5.9) used by Swenson and Hardeman (1997), and investigate the pressure, temperature and fracture aperture change. In this simulation, we assume that the fractures are in equilibrium under the initial far-field stress. The initial pore pressure is 27 MPa, the flow rates in both wells is set to 3.5×10^{-4} m^3/sec. The injection water has a temperature of 320 K while the reservoir rock is initially at 420 K, resulting in a maximum cooling of 100 K. Other parameters are all same with Tao and Ghassemi (2010).
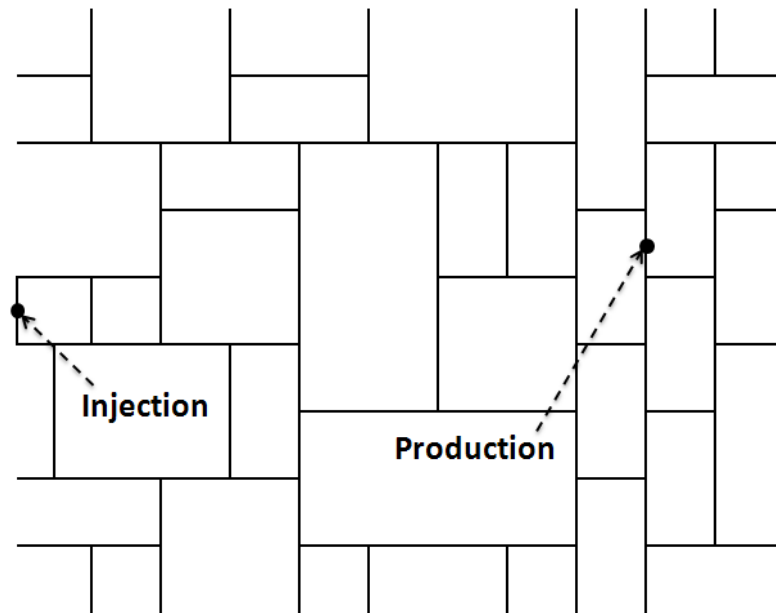
Fig. 5.9 Irregular fracture network having 111 fracture segments over an area of 132×108 (m^2).

5.2.1 Isothermal Condition

This section investigates the pressure and fracture aperture in the fracture network and also considers the induced pressure and stress distribution in the reservoir matrix. This can provide insight in relation to interpretation of induced seismicity.
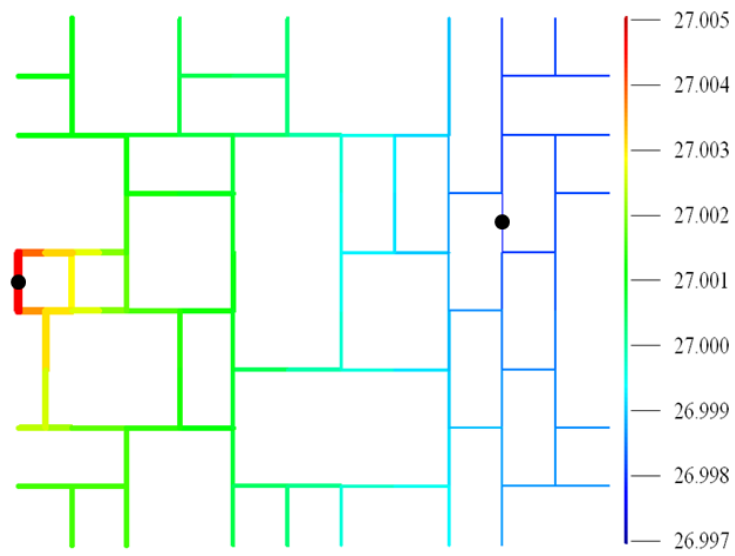
Fig. 5.10 Pressure (MPa) distribution in fracture after 1000 days of injection and production.

In Fig. 5.10, as expected, the pressure around the injection well is slightly higher and the pressure around the production well is slightly lower than other fracture segments and field (matrix).
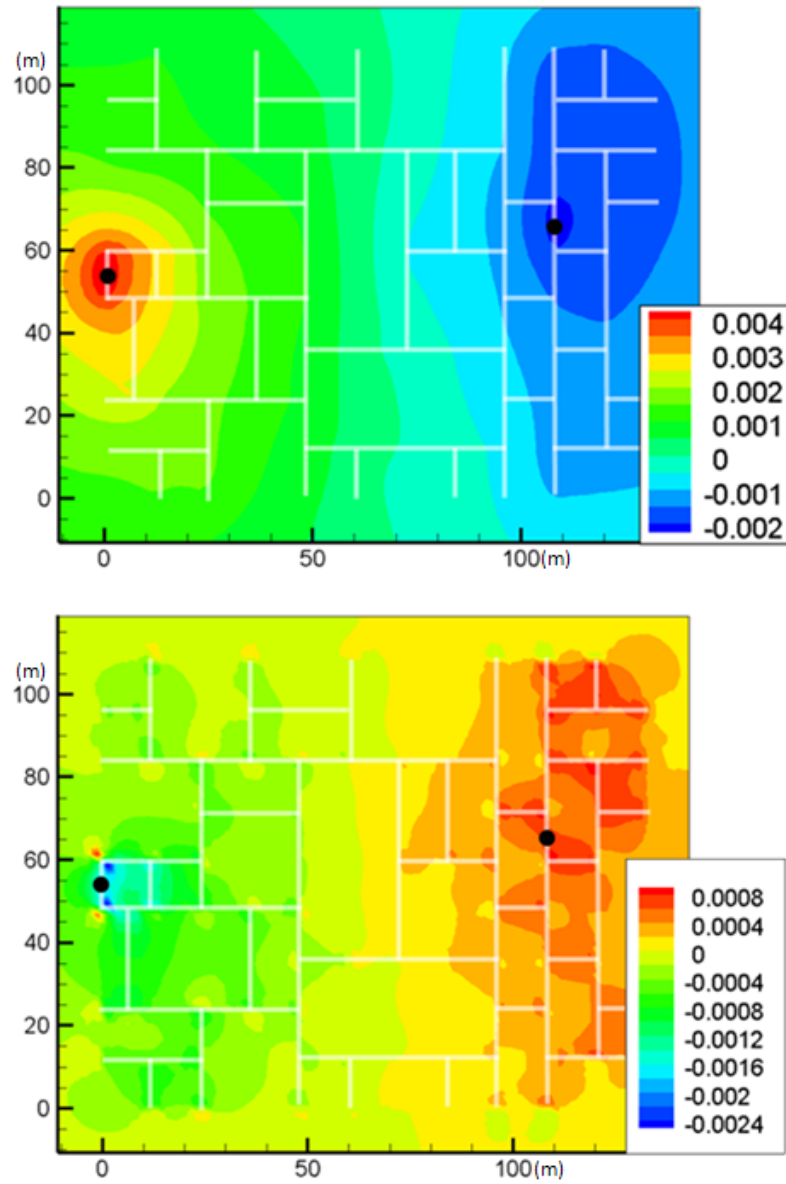
Fig. 5.11 Induced pressure (top, MPa) and stress (lower) distribution in the rock after 1000 days of injection and production.

In Fig. 5.11, because of pore pressure, the pressure around the injection well is higher than around the production well. Also, we can see the induced effective stress (mean stress, $(\Delta\sigma'_{xx}+\Delta\sigma'_{yy})/2$) around the injection well is lower than other area since the higher pore pressure reduces the amount effective stresses in the matrix. In contrast, the

induced effective stress around the production well is higher since the lower pore pressure makes the rock (matrix) expanded.
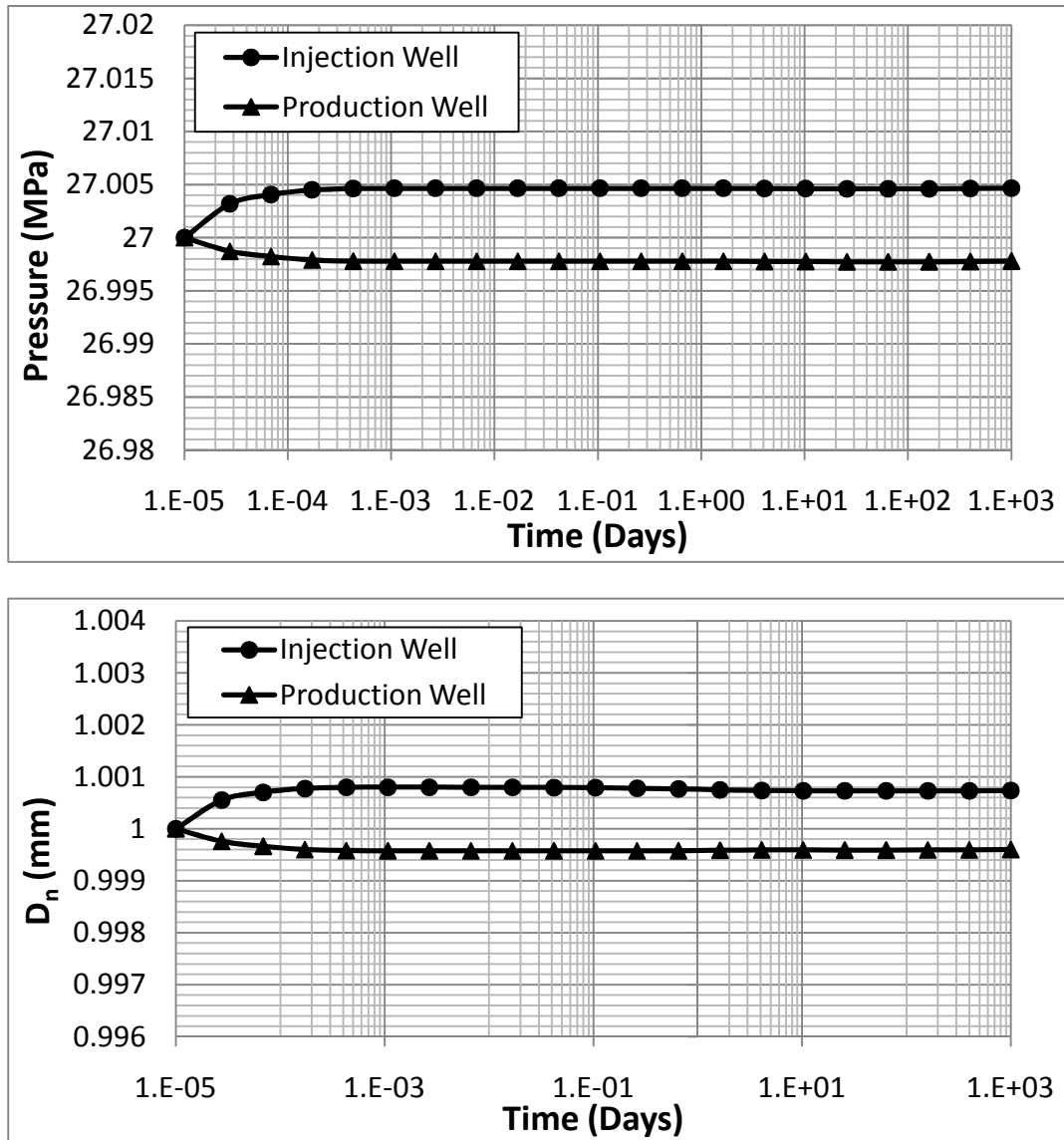
Fig. 5.12 Pressure and fracture aperture change with time in injection/production wells.

According to Fig. 5.12, the fracture pressure is stabilized in early time and so the fracture aperture is also stabilized. And with time, the fracture aperture at the injection

well decreases and the aperture at production well increase very slightly because of matrix dilation and contraction (poroelastic effect).

5.2.2 Non-isothermal Condition

In this section, also investigate the pressure and fracture aperture in fracture network and both wells and also investigate the induced pressure and stress distribution in matrix in 100 K cooling condition.
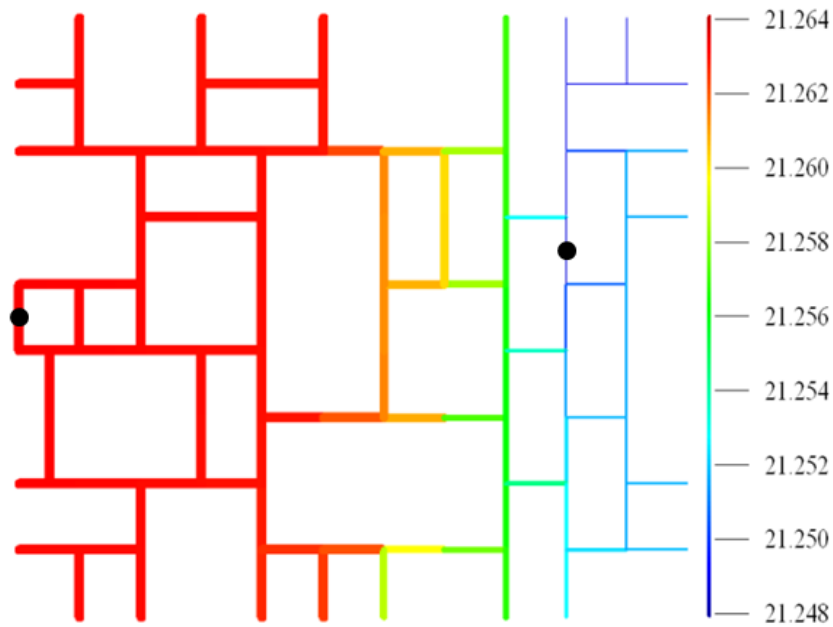
Fig. 5.13 Pressure (MPa) distribution in fracture after 1000 days of cooling injection and production.

According to Fig. 5.13, the injection fluid flows following fracture network and cause pressure increase in fracture around the injection well. We can also see several flow channels from the injection well to the production well. It can be noted that despite equal injection/extraction rates, the pressure within the flow paths is much lower than

the initial reservoir pressure. This is because the fluid is colder and tends to open the
fractures.
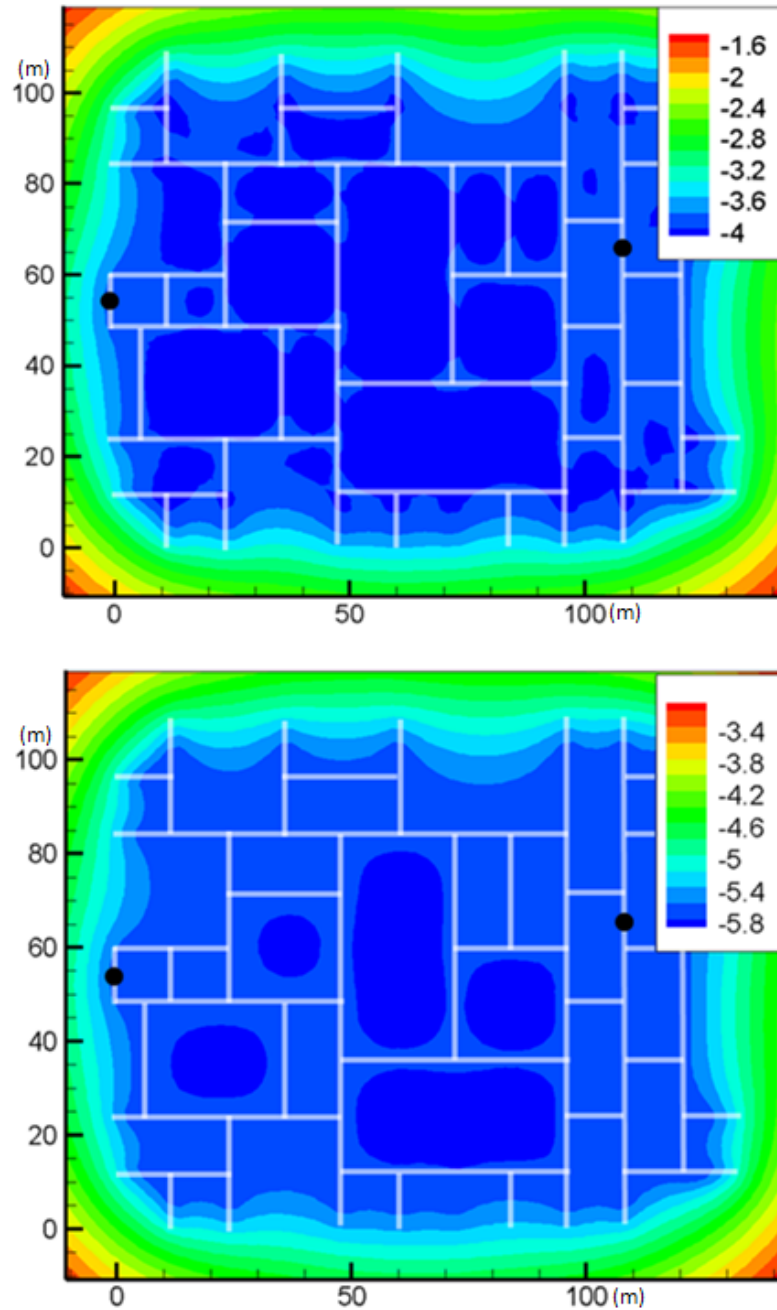
Fig. 5.14 Induced pore pressure (MPa) distribution in the rock after 400 (top), 1000
(lower) days of cooling injection and production.

In Fig. 5.14, after 400 days of cooling operation, the pressure in fractures are about 23 MPa and outside of fracture network are 25.4 MPa, so in fracture network and matrix inside or near the fracture network is lower than outside of fracture network because of cooling effect. And after 1000 days of operation, the pressure within the fracture network drops to about 21 MPa.
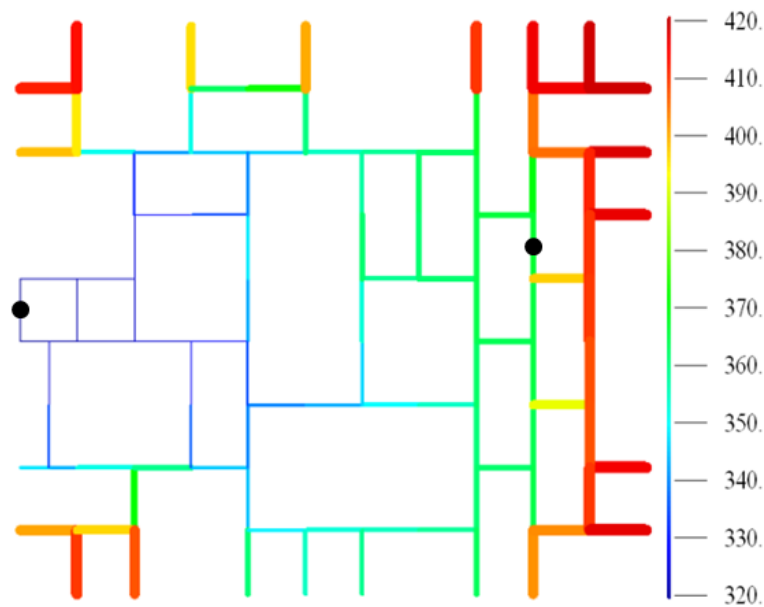
Fig. 5.15 Temperature (K) distribution in fracture network after 1000 days in cooling operation.

An interesting result from this figure is that the pressure in the matrix is lower than the pressure in fracture because of poro-thermoelastic effect. Excessive drop in pore pressure may not contribute to shear failure in those areas, particularly since they are not subjected to significant cooling-induces tensile stress. If the matrix is not fully surrounded by fracture network and the square is small, we cannot see this pattern.

According to Fig. 5.15, the temperature is 320 K near the injection well. The temperatures in fracture segments located near the production well and on the right side are higher. This is because the injected fluid flows mostly from injection well to production along some of the fracture on the left side. When we see the temperatures in four corners of this fracture network, the temperature is still high because the cold fluid doesn't flow the corner and also the temperature does not spread out to the corners yet. When looking the fractures at the bottom of the center area, the temperatures are lower because there is a fracture channel right above those fractures.
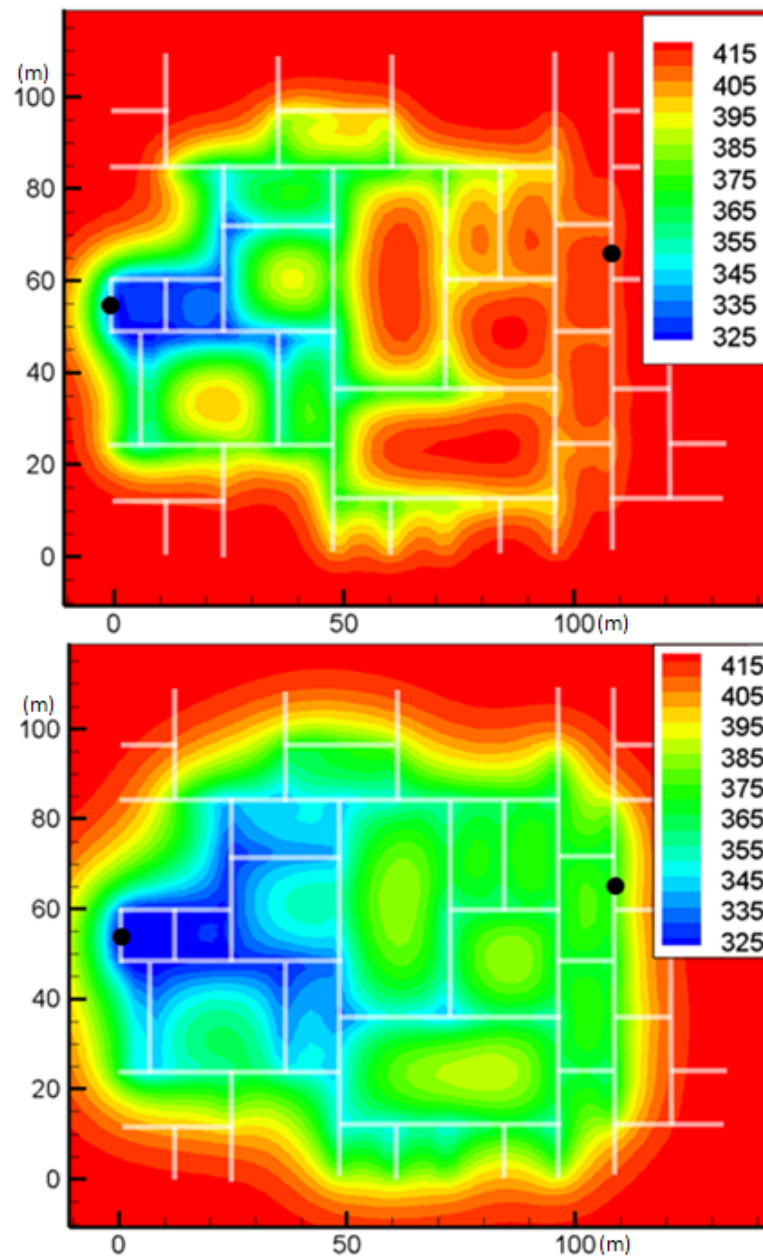
Fig. 5.16 Temperature (K) distribution in the rock after 400 (top), 1000 (lower) days of cooling injection and production.
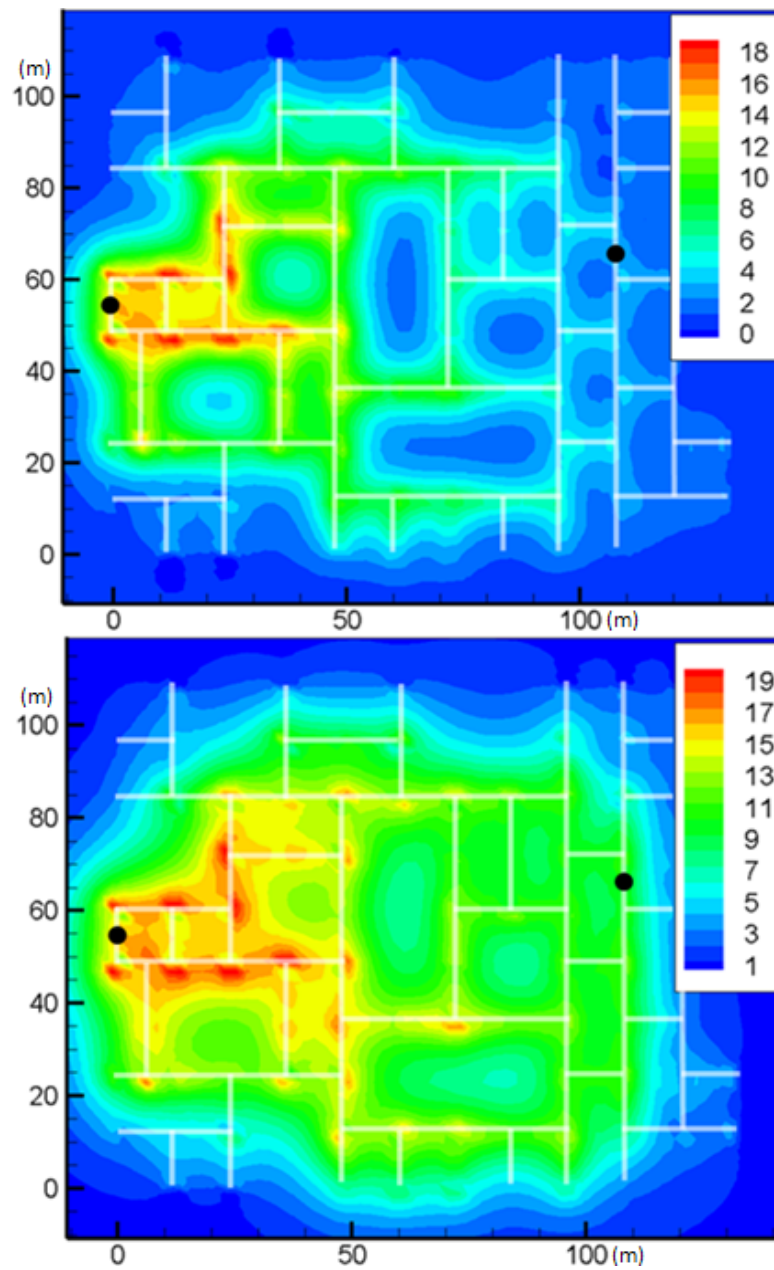
Fig. 5.17 Induced mean, $(\Delta\sigma'_{xx}+\Delta\sigma'_{yy})/2$, stress (MPa) distribution in the rock after 400 (top), 1000 (lower) days of cooling injection and production (tension positive).

In Fig. 5.16, after 400 days, the temperature around the injection well is about 320 K but in production well, it still is close to the initial temperature of 420 K. After 1000 days, the cold fluid spreads out from through fracture network and cools down the

reservoir matrix by heat conduction. Note the zones of higher matrix temperature occur in the central regions of each block except where the water has cooled the area from all sides. Also we can see a smooth temperature boundary in this figure; it means that the temperature also spreads out from fracture segments to matrix by poro-thermoelasticity.

Fig. 5.17 shows the effective mean, average value of $\Delta\sigma'_{xx}$ and $\Delta\sigma'_{yy}$, $(\Delta\sigma'_{xx}+\Delta\sigma'_{yy})/2$, stress distribution. 400 days cooling of operation, since injecting cold fluid at injection well, the rock (matrix) around it is shrunk and it causes tensile stress. And after 1000 days, due to the cold temperature spreading, we can see that most parts of system show high tensile stress. When comparing Fig. 5.16 and 5.17, the distribution shapes are very similar but not exactly the same because the pore pressure increases by fluid injection causes compressive stresses (small compared to thermal stress).
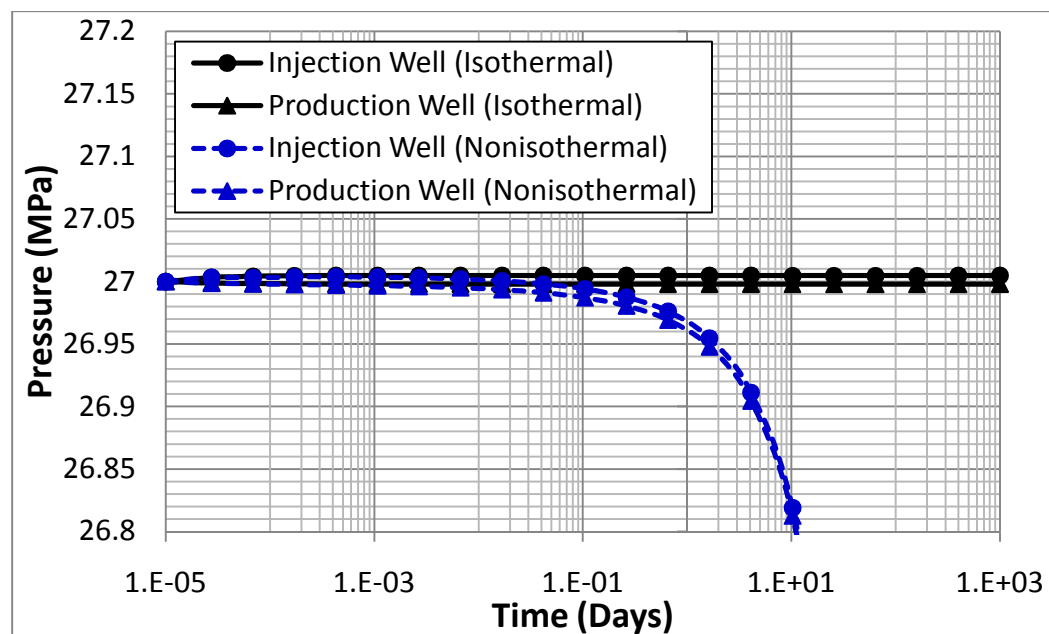
Fig. 5.18 Fracture pressure change with time at injection/production well in isothermal/non-isothermal cases.

According to Fig. 5.18, the pressure at injection and production well is 27.01 MPa and 26.99 MPa each, initially. (Because of small flow rate, the pressure difference in both wells is small.) After the cooling starts to affect to system, the pressure starts to decrease in both wells. And at the end of the time step, the pressures in both wells are 21.26 MPa and 21.24 MPa.
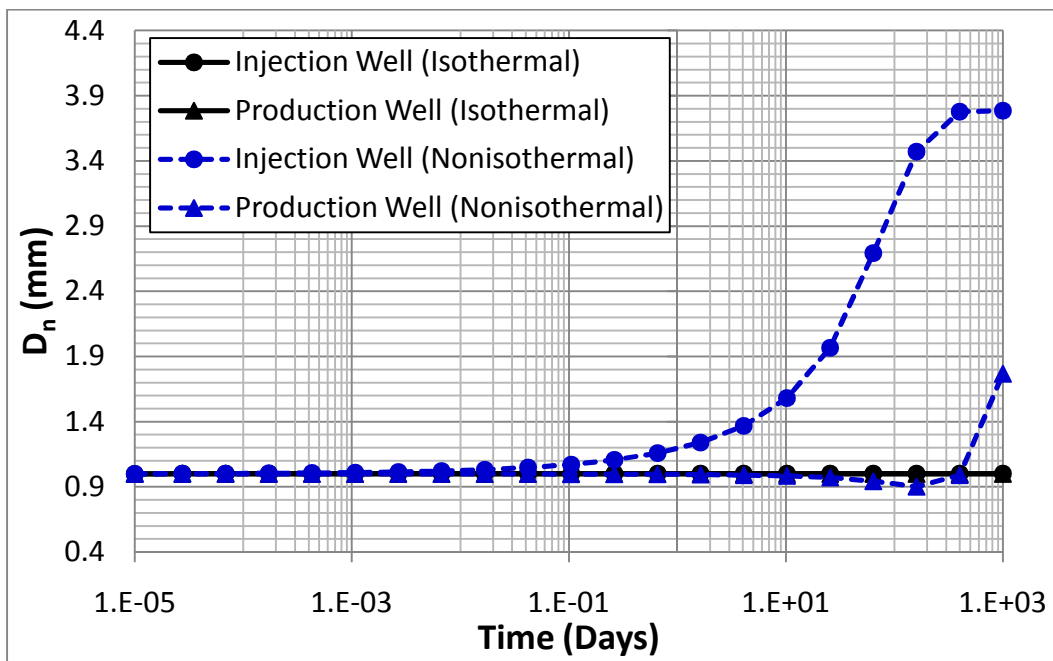
Fig. 5.19 Fracture aperture (D_n) change with time at injection/production well in isothermal/non-isothermal cases.

According to Fig. 5.19, for the cooling case, D_n increases at the injection well and stabilizes after 400 days while it initially decreases at the production well and starts to increase after 200 days. The contribution of cooling to aperture increase at the production well is high at the time shown and the closure due to the pore pressure reduction is much smaller than cooling effect.
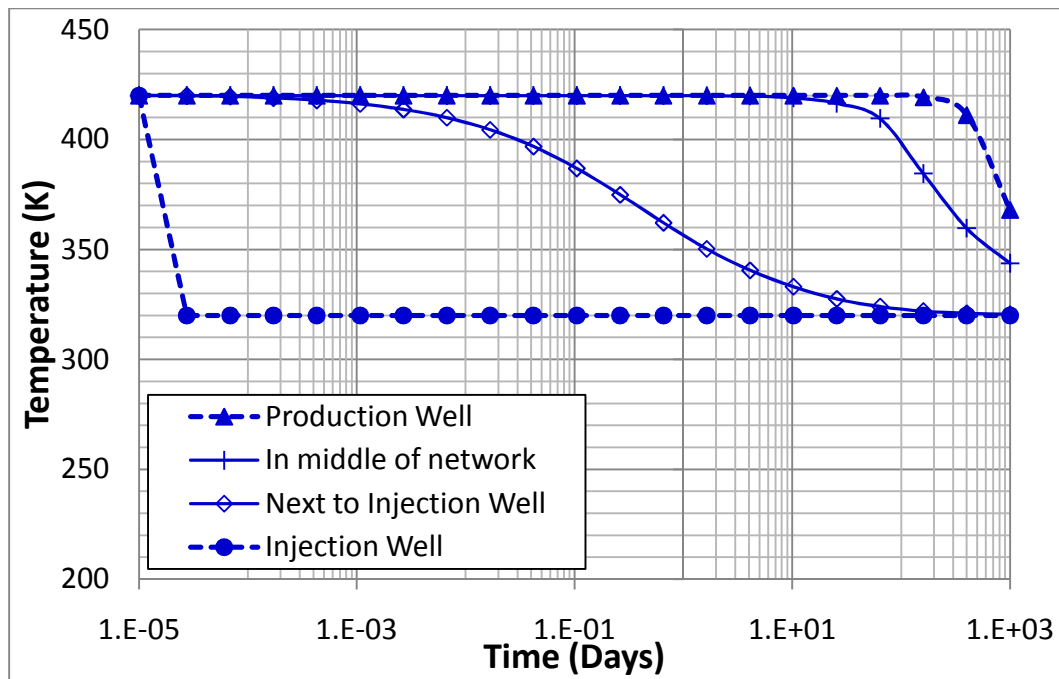
Fig. 5.20 Variation of temperature (K) at injection and production wells with time.

In Fig. 5.20, the temperature at production well is changed by cooling effect at 200 day and it reaches about 368 K at 1000 days of operation. A temperature near the injection well is decreased in early time step and it reaches 320 K after 200 days later.
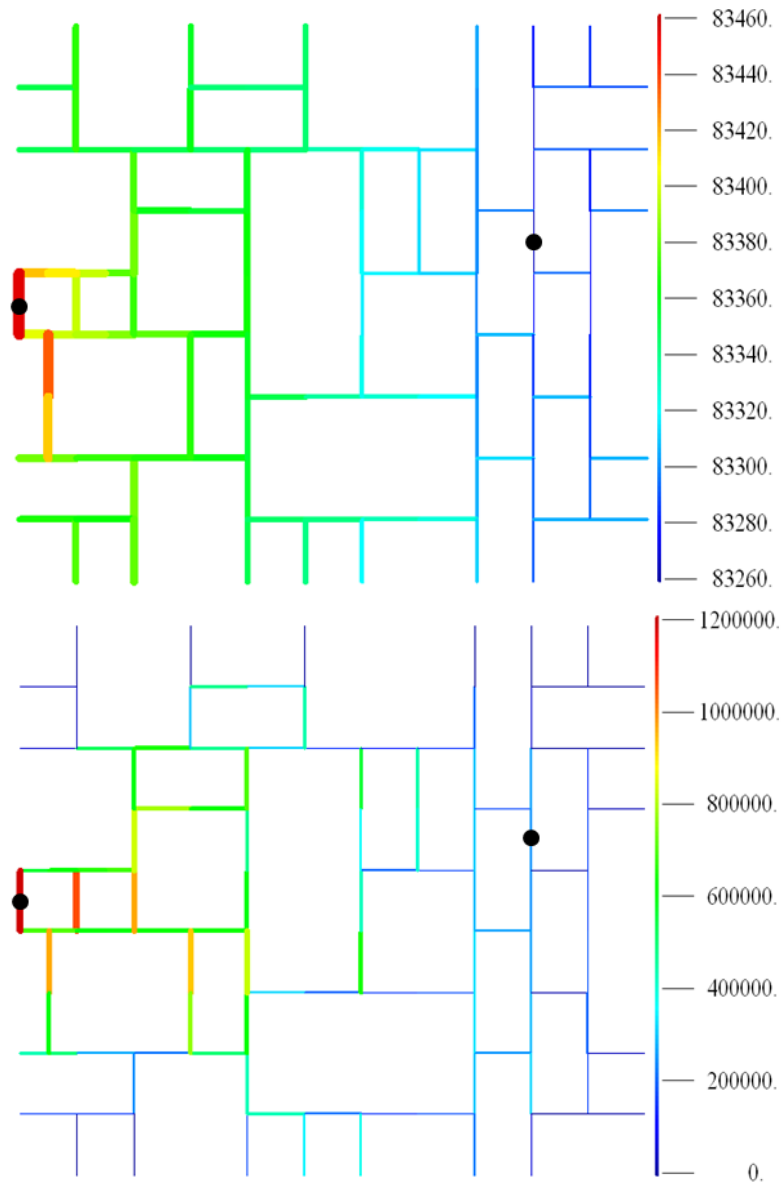
Fig. 5.21 Permeability (Darcy) distribution in fracture after 1000 days in isothermal (top) and cooling (lower) operation.

Fig. 5.21 shows the conductivity ($k_f = w_f^2/12$, Witherspoon et al., 1980) distribution in the fracture network. For isothermal condition, the fracture apertures at injection/production wells stabilized in early time step. So, the permeability values are more stable at the beginning and equal about 83,460 Darcy.

However in cooling case, the aperture of fracture segments are very high because the cooling makes the fracture aperture larger. Therefore, the fracture conductivity in cooling is higher comparing with isothermal condition.
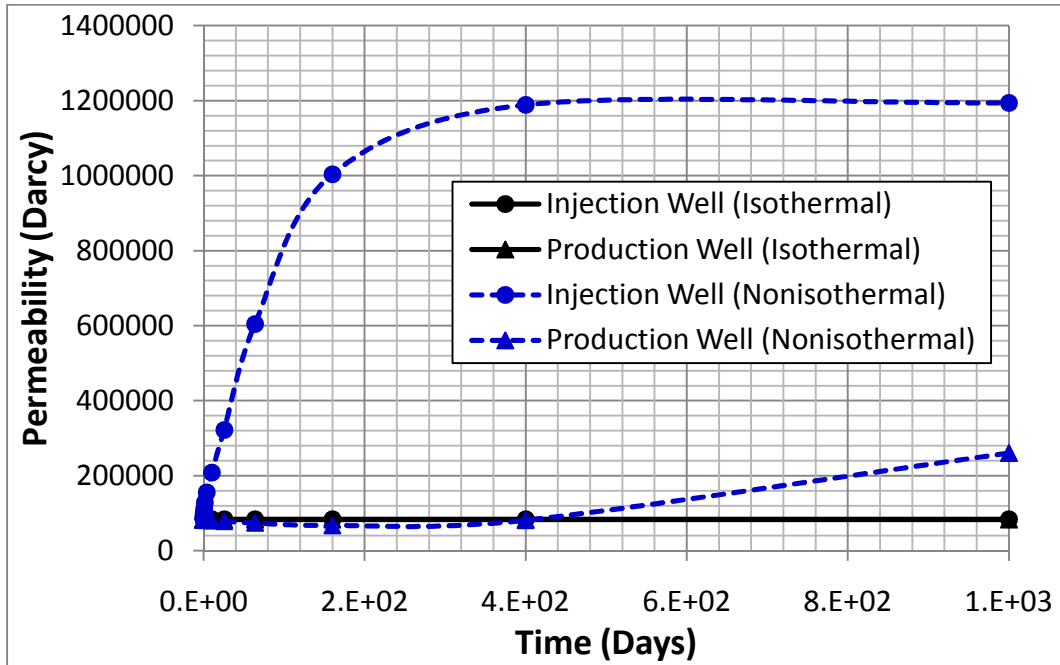
Fig. 5.22 Permeability change at injection/production wells in isothermal/cooling with time.

According to Fig. 5.22, the conductivity of the fracture varies by time at injection and production well also both in isothermal and cooling operation. Due to the graph, the permeability at the injection well in cooling is increased quickly in early time step. After 400 days, this value is stabilized around 1,200,000 Darcy.

In following example (Fig. 5.23), a fluid channel with slightly different fracture network is examined. The fluid flows from injection well to the production well so the cold temperature mainly spreads out through the fracture network.
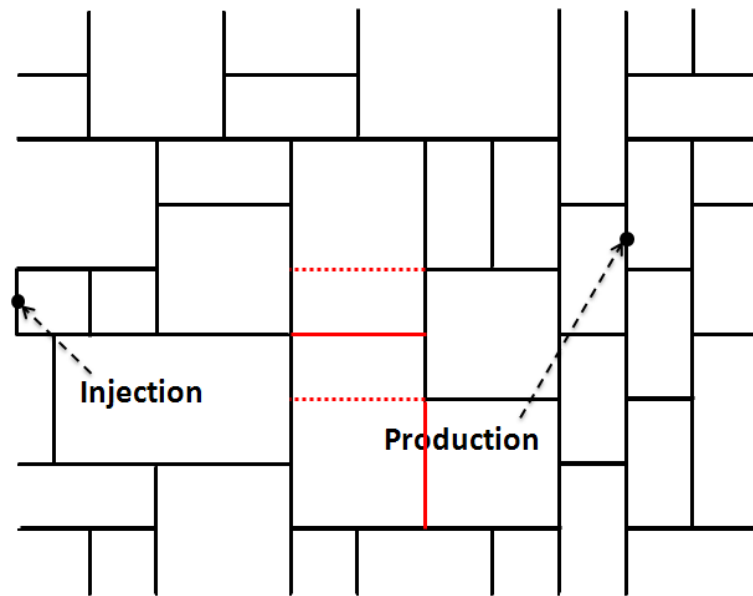
Fig. 5.23 Irregular fracture network (red line: slightly different with Fig. 5.9) having 111 fracture segments over an area of 132×108 (m^2).
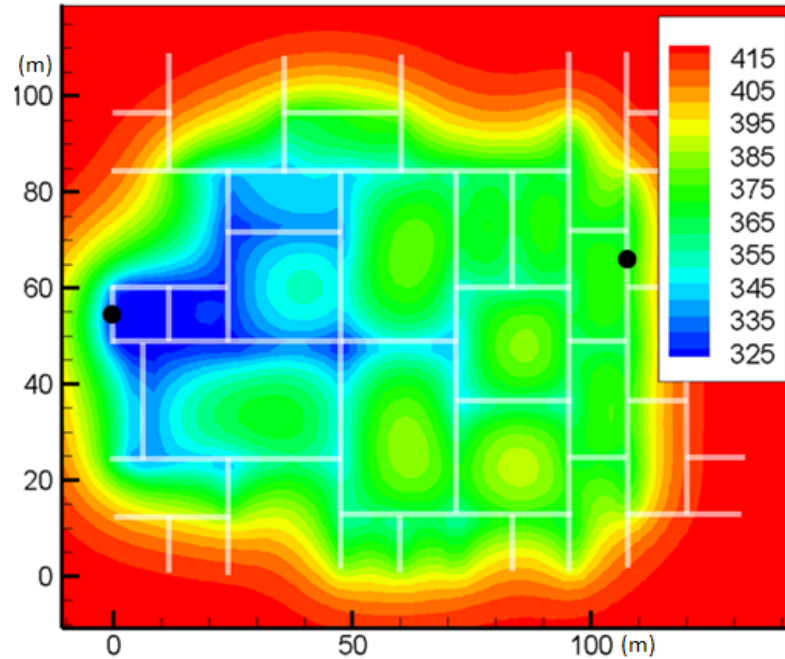
Fig. 5.24 Temperature (K) distribution in the rock after 1000 days of cooling injection and production.

When comparing this figure to Fig. 5.16, in Fig. 5.24, the fracture network is slightly changed affecting the flow channels in the central area. But in the outer regions the spread of temperature in both figures are very similar. The figures illustrate the importance of fracture flow on heat transport. The temperature profile near the edge of these fracture networks is similar because there is no fluid flow so the cold temperature spreads out by just conduction (Fig. 5.24).
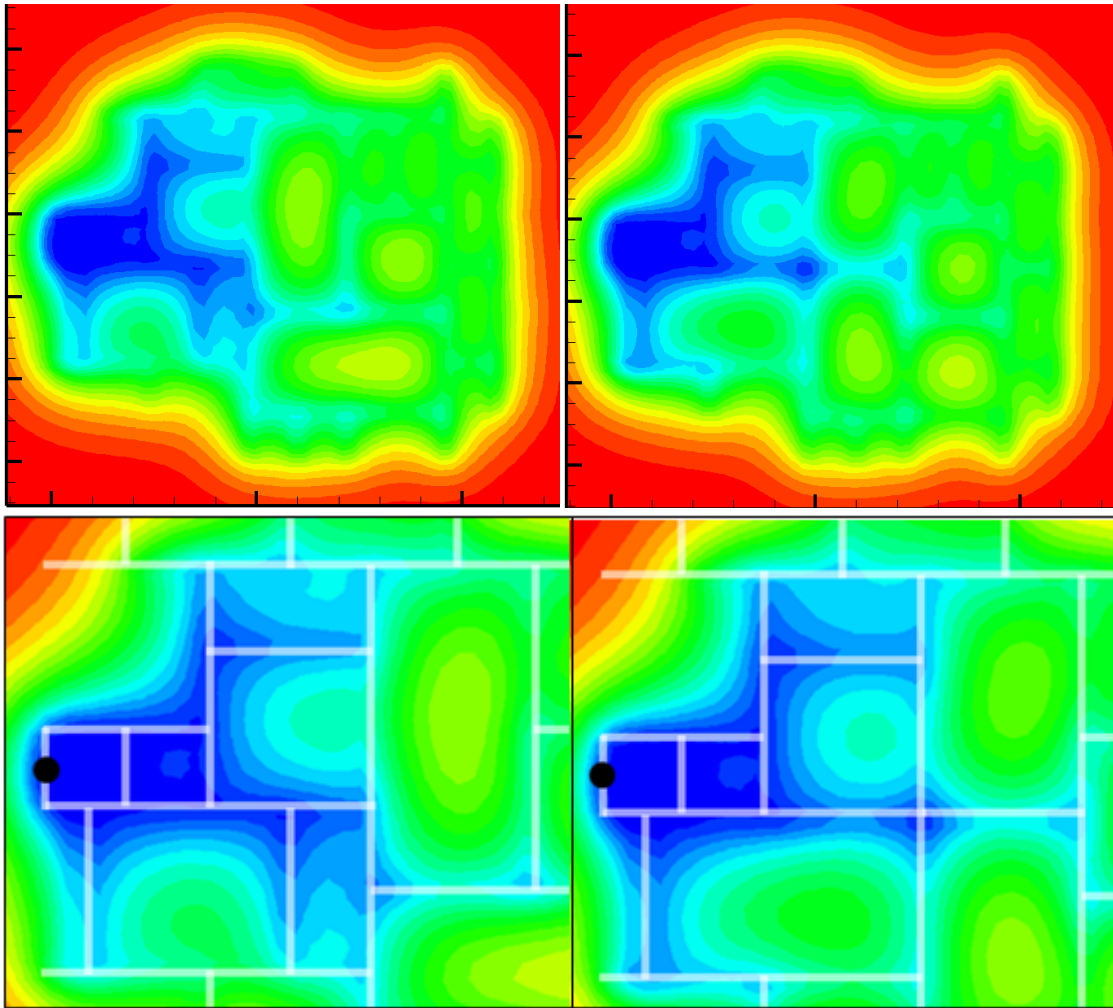
Fig. 5.25 Overall shape (top) and center (lower) area of Fig. 5.16 (left) and Fig. 5.24 (right), the cold temperature spread out through the different fracture channels.

Fig. 5.25 shows the different flow channels in different fracture network. The cold temperature spreads out the fracture network and the cold temperature spreads out from fracture channel to matrix.

To investigate more detail temperature distribution resulting from discontinuous injection/extraction, consider the smaller irregular fracture network for shorter route from injection point to extraction point shown in Fig. 5.26 to check more dynamic temperature changes in each measure point. The production well shut-in is simulated by reducing the rate to zero while the injection well rate is reduced from 3.5×10^{-4} m^3/sec to 7×10^{-7} m^3/sec at the 19th time step.
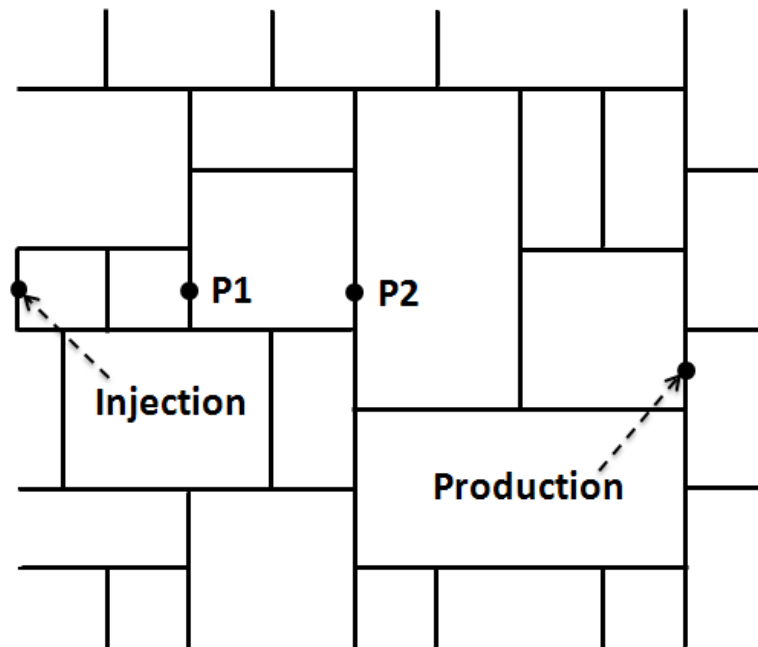
Fig. 5.26 Irregular fracture network having 78 fracture segments over an area of 108 × 96 (m^2). P1 and P2 are measure points.
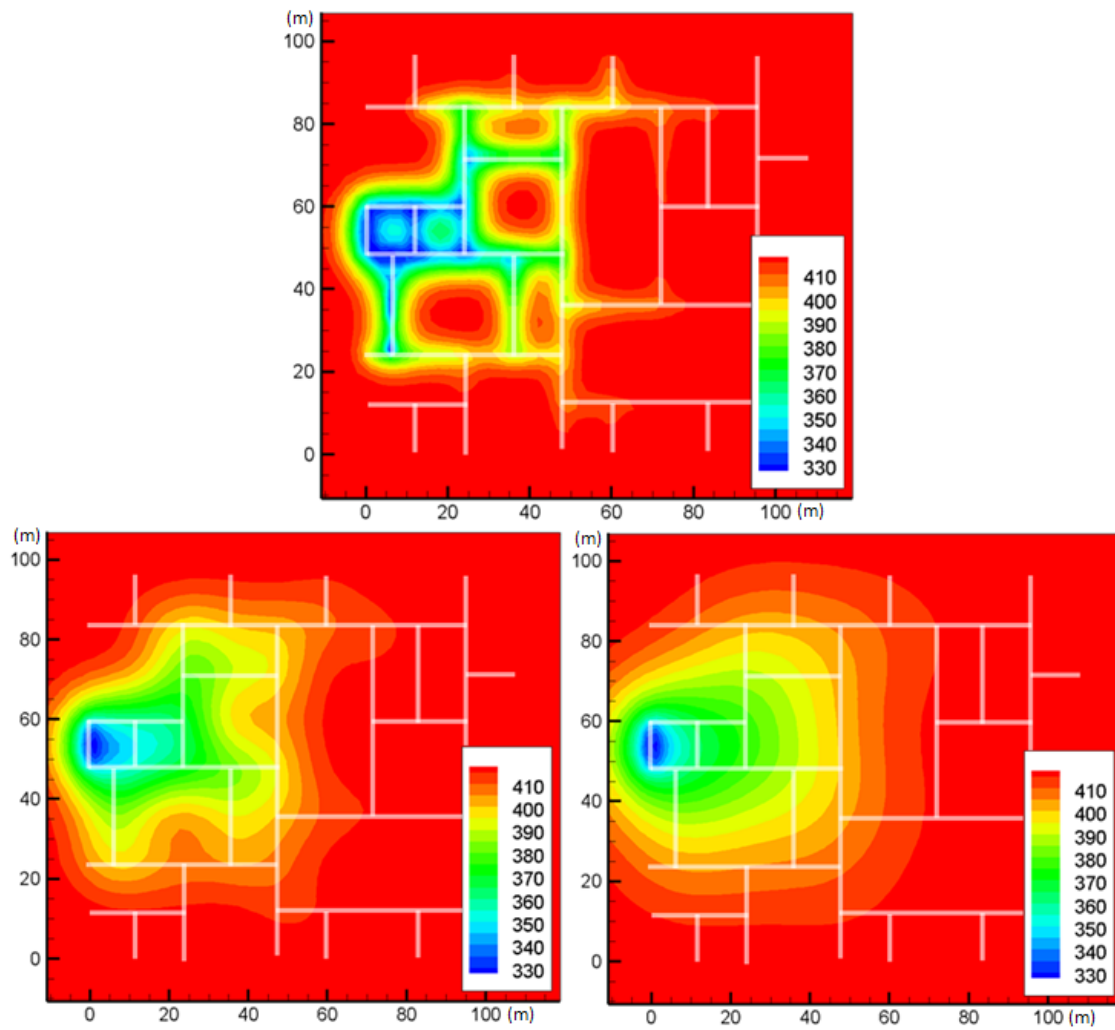
Fig. 5.27 Temperature (K) distribution in the rock after 160 days of cooling injection/production (upper), 240 days (lower left) and 840 days (lower right) days of cooling injection after shut in the production well.

According to Fig. 5.27, we can see that until 160 days, the cold fluid flows through the fracture network so it spread out quickly from injection well towards the production well in several fracture channels. However after 240 days from shutting the extraction well, the temperature spreads out from fractures to field in the opposite direction, and the temperature inside of the fractures which are located in the middle of

fracture network increase again by spreading of warm temperatures from the extraction side.
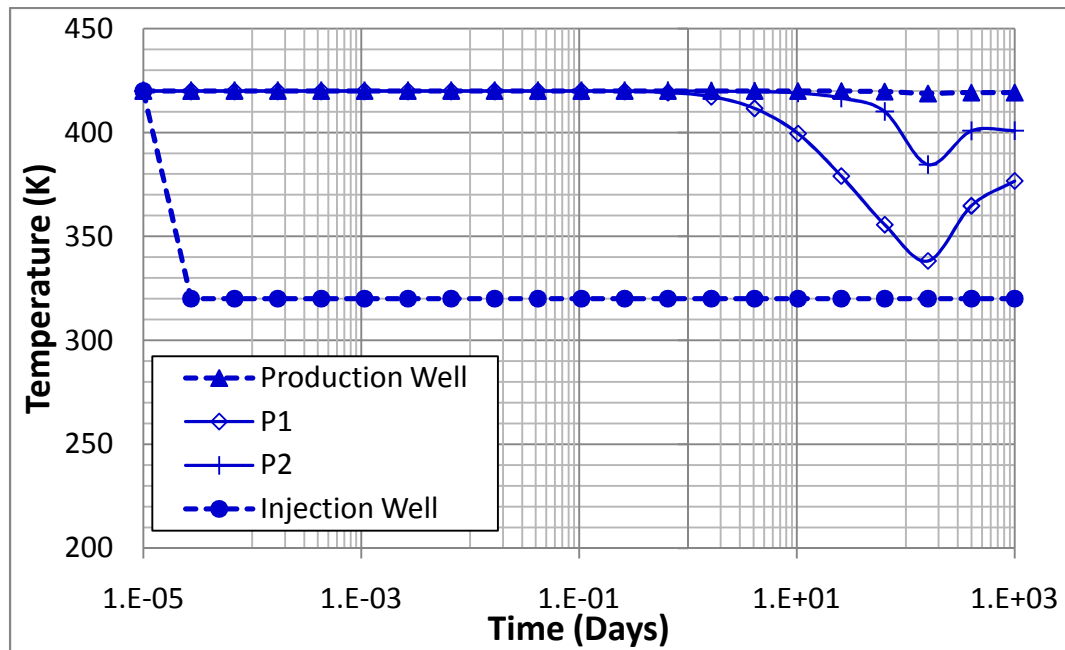
Fig. 5.28 Variation of temperature (K) at P1, P2, injection and production wells with time under stopped production with reducing injection rate.

In Fig. 5.28, the temperature in the fracture at P2 decreases to about 385 K after 160 days of operation, but after production well shut-in, the temperature is increased again because the cold fluid does not flow through the fracture network anymore. So, the water is heated up by the matrix. Also, note the cold front movement behind the production well. After 1000 days, this temperature starts to decrease again as the volume of cold water injection becomes sufficient to have an impact. However, at P1, the temperature reaches the lowest about 340 K so that it keeps increasing at the end.
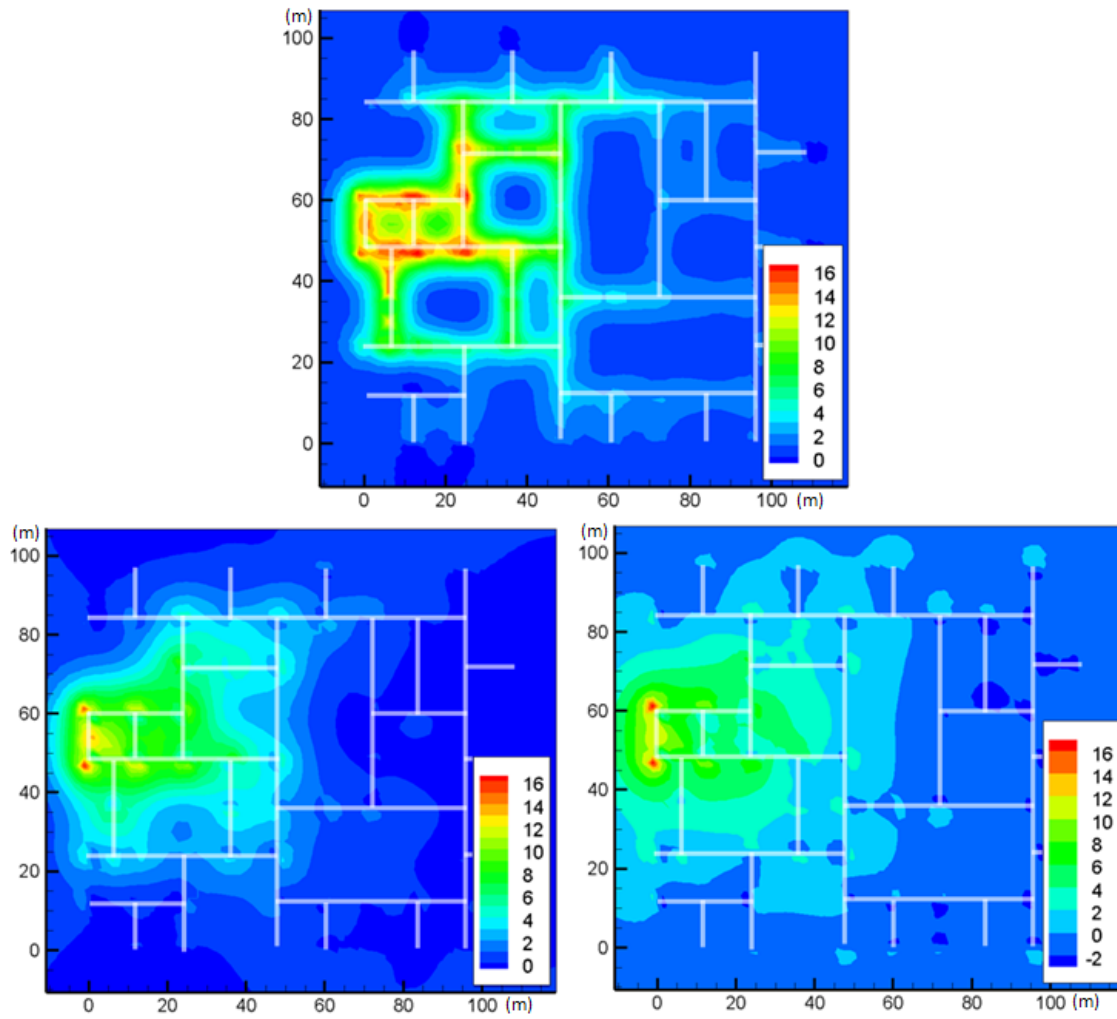
Fig. 5.29 Induced mean, $(\Delta\sigma'_{xx}+\Delta\sigma'_{yy})/2$, stress (MPa) distribution in the rock after 160 days of cooling injection/production (upper), 240 days (lower left) and 840 days (lower right) days of cooling injection after shut in the production well.

In Fig. 5.29, until 160 days of operation, there are higher tensile stresses about 16 MPa near the injection zone. After stopping extraction, the cold fluid spreads out just near the injection well. But after 240 days injection, the fractures connected with the injection well and used as flow channels has higher tensile stress. Due to absence of

production well, the tensile stresses in the vicinity of injection well are decreasing until

the cold effect appears again.
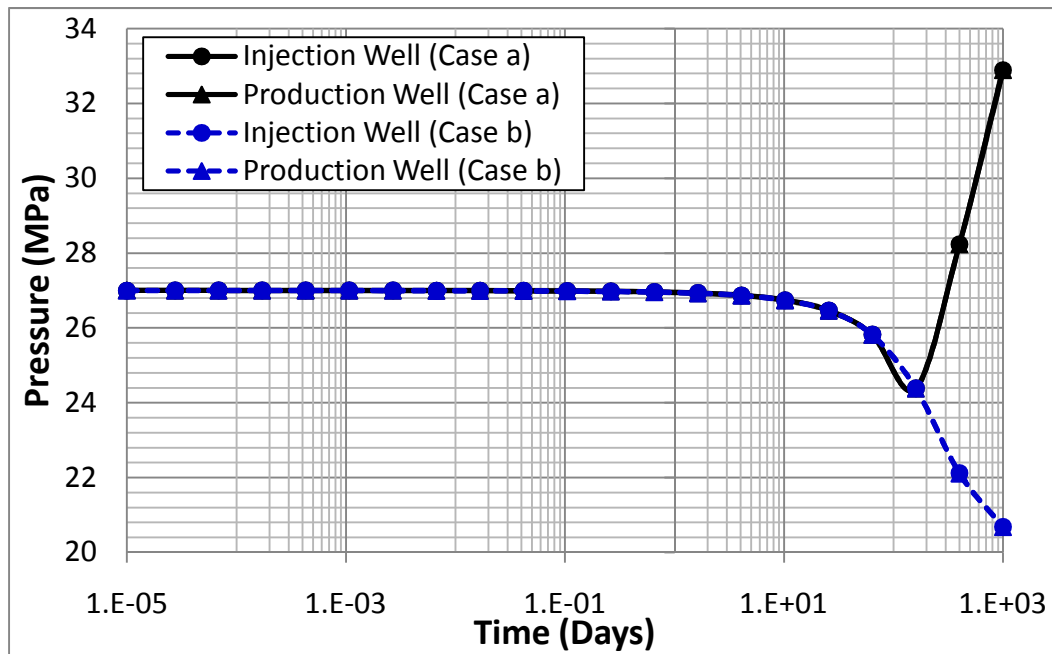
Fig. 5.30 Fracture pressure change with time at injection/production wells under constant injection/production and stopped production with reducing injection rate (Case a: shut-in production well, Case b: continuous injection/production).

In Fig. 5.30, when there is constant injection and production in cooling operation,

the pressures in both wells keep decreasing with time. After shutting in the production

well, the pressure in the fracture network starts to increase with smaller injection rate

from 3.5×10^{-4} m^3/sec to 7×10^{-7} m^3/sec. In both cases, there is no significant pressure

difference in both wells.
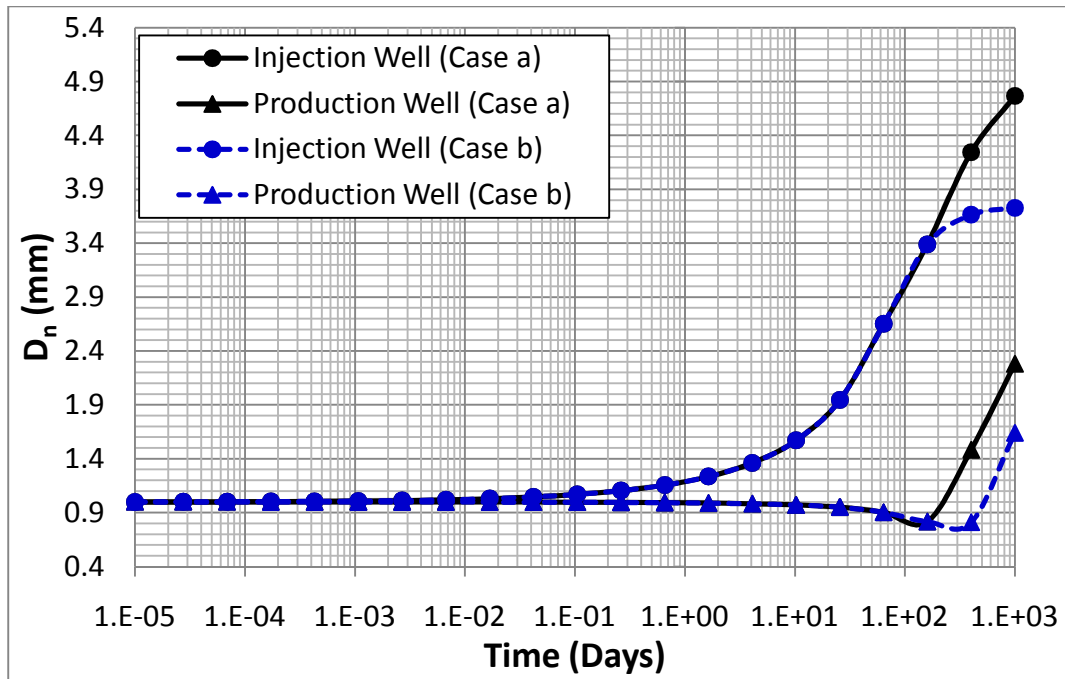
Fig. 5.31 Fracture aperture change with time at injection/production wells under constant injection/production and stopped production with reducing injection rate (Case a: shut-in production well, Case b: continuous injection/production).

According to Fig. 5.31, in constant injection and production operation, the fracture aperture in injection well is drastically increased and stabilized after 400 days and in production well, the fracture aperture is decreased due to production. But after 400 days of operation, the cold fluid reaches the production well, increasing the fracture aperture. However, when the production well is shut at 18th time step, the pressure at the injection well increases more than the constant production case and the pressure at production well starts to increase right after shutting the well.
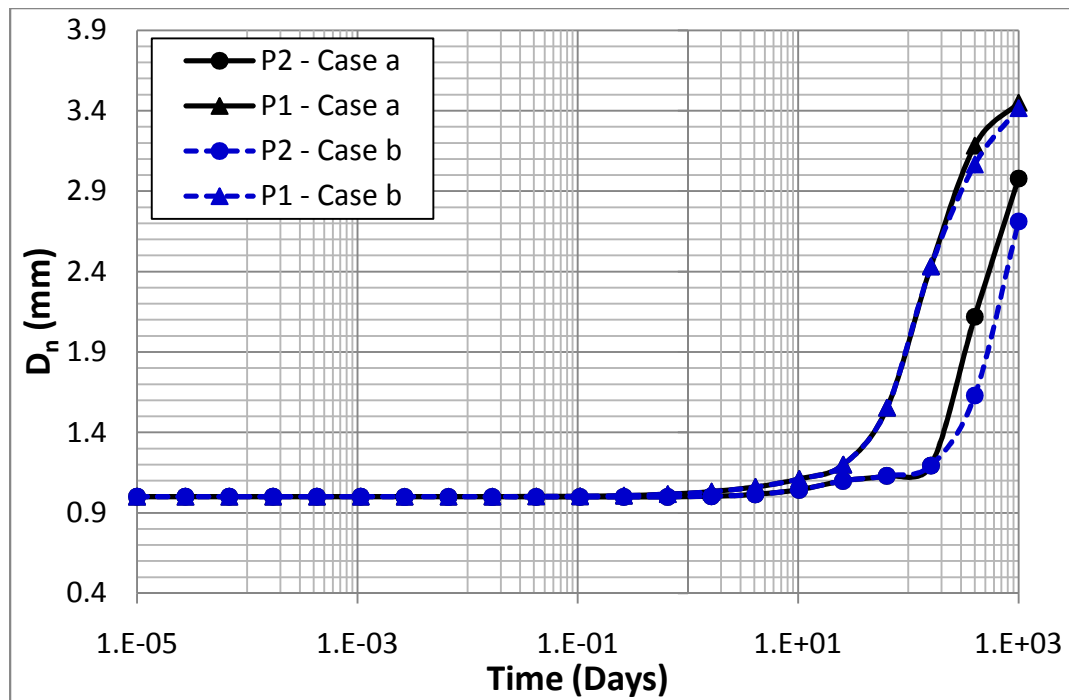
Fig. 5.32 Variation of fracture aperture at P1 and P2 with time under stopped production with reducing injection rate (Case a: shut-in production well, Case b: continuous injection/production).

Comparing Fig. 5.28 and Fig. 5.32, shows that there are temperature increases at P1 and P2 when shutting the production well, and the fracture apertures increase continuously. Even though the production well is shut and the fracture temperatures are increased, the matrix is still cold so the heating is not sufficient to cause fracture apertures decrease.

5.3 Regular Fracture Network

Tao and Ghassemi (2010) already investigate the pressure, temperature and normal displacement change for and injection/production operation. However, it was assumed that the joint are in equilibrium under the initial stress state. In this work, non-equilibrium under the initial far-field stress is considered an example simulations are provided using the same regular fracture condition and input data. The fractured domain is 2000×2000 (m^2) and has a unit thickness (1 m). The initial fracture pressure is 27 MPa, the flow rates in both wells is set to 1×10^{-4} m^3/sec. The injection water has a temperature of 300 K while the reservoir rock is initially at 420 K. Other parameters are all same with Tao and Ghassemi (2010).
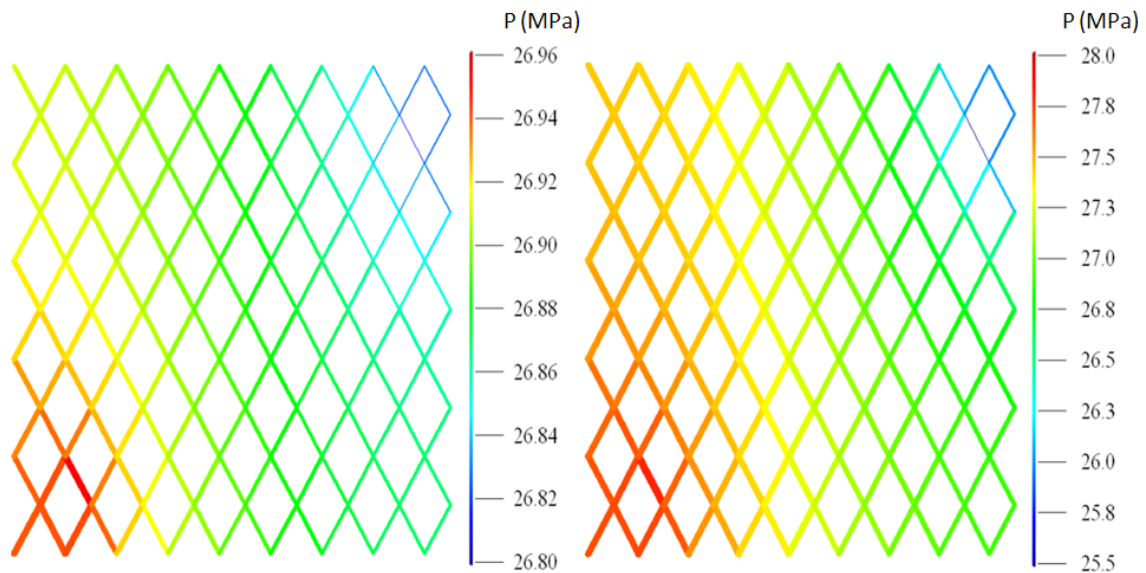
Fig. 5.33 Pressure distribution after a year injection/production (left: without initial far-field stress, right: with initial far-field stress).

According to Fig. 5.33, this pressure distribution has a range of 25.5 ~ 28.0 MPa which is broader than 26.8 ~ 26.92 MPa obtained by Tao and Ghassemi (2010) and reflects the impact of fracture deformation under the initial far-field stress.
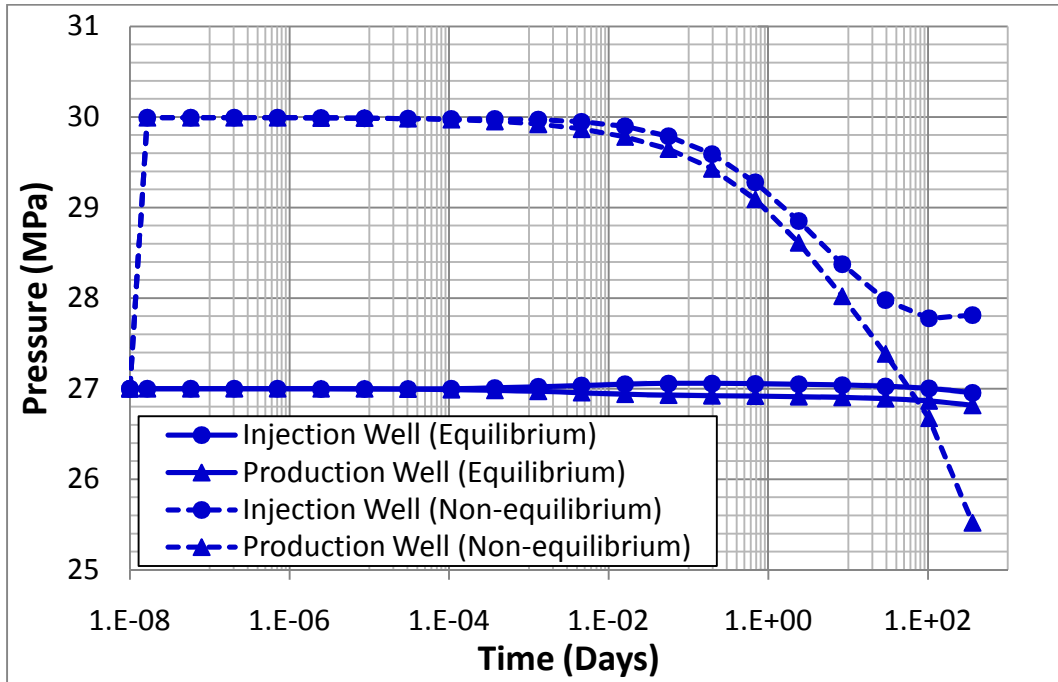
Fig. 5.34 Pressure variation in time at injection/extraction wells with and without initial fracture deformation.

When comparing the injection/extraction well pressure profile in time, large differences are observed in Fig. 5.34. The initial pore pressure is 27 MPa, but it is increased to 30 MPa because of compression and fracture closure. This effect is not noticeable for high fluid bulk modulus. The aperture increases at the production well after initially closing to some extent, but in the production well, the fracture pressure keeps decreasing.
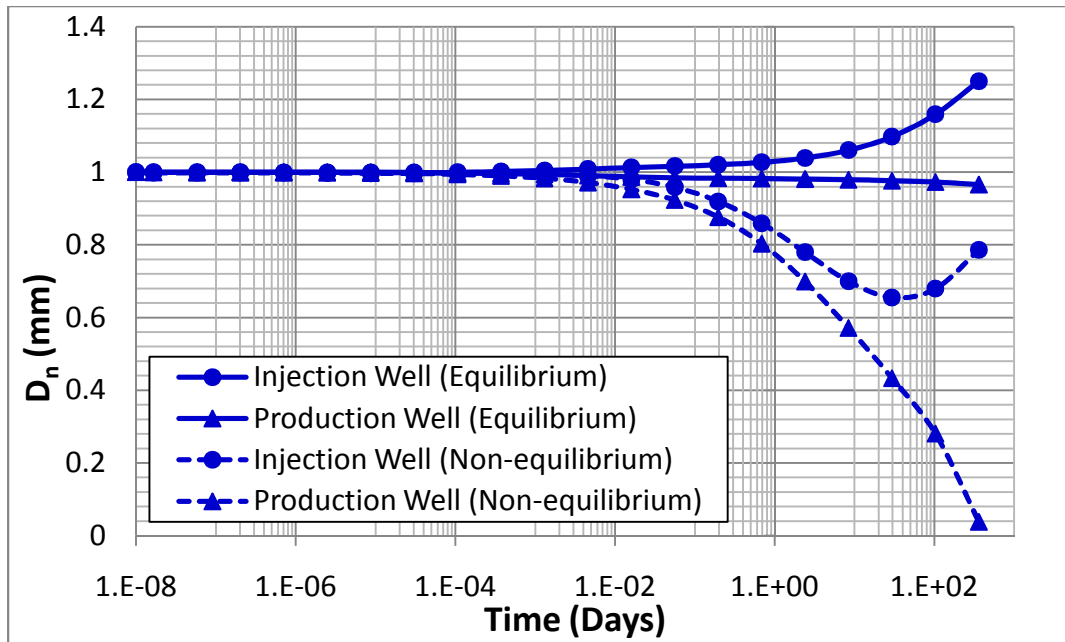
Fig. 5.35 Fracture aperture (D_n) change with time at the wells (with and without the initial deformation).
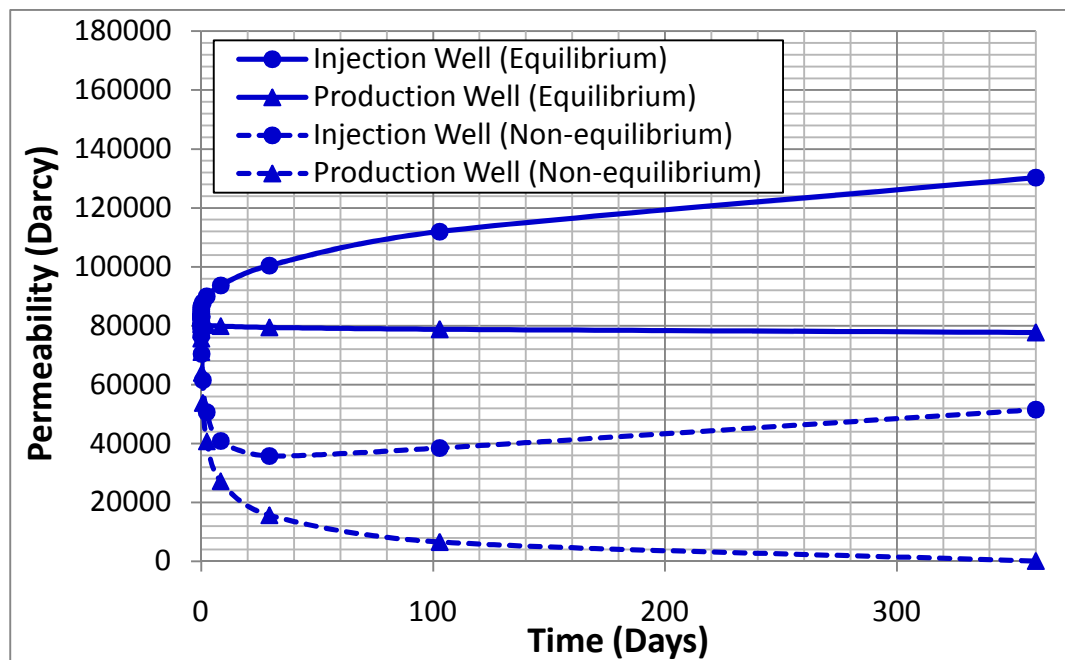
Fig. 5.36 Permeability (Darcy) change with time at the wells (with and without the initial deformation).

According to Fig. 5.35, the normal displacement (D_n) starts from 1 mm. But in reality, D_n under initial far-field stress condition is slightly smaller than when the response to initial stress condition is not included. Because of fluid compressibility, the fluid in the fracture is compressed and closes the fracture aperture slightly. After that, the D_n is decrease by pressure drop and at injection well, after several time steps, the D_n starts to increase with pressure increase by injection. When the D_n is larger, the fracture permeability is larger by Cubic Law. Therefore, Fig. 5.36 follows the results of Fig. 5.35.
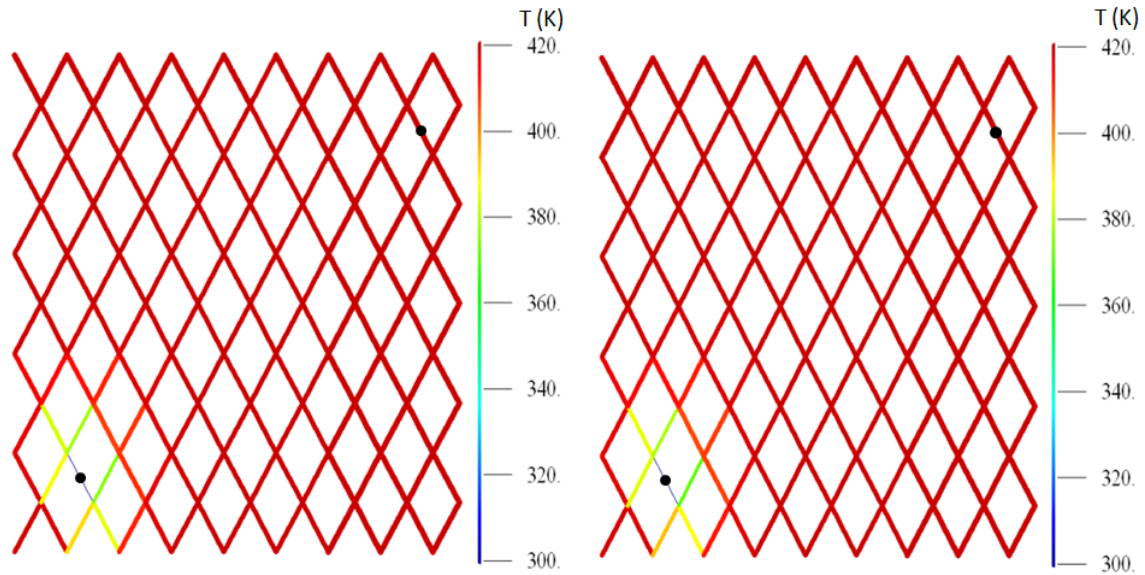
Fig. 5.37 Temperature (K) distribution after a year injection/production (left: without initial far-field stress, right: with initial far-field stress).

In Fig. 5.37, comparing the temperature distribution figures between the simulation without initial far-field stress and with initial far-field stress, these are almost same. It means that the in this particular case, lack of equilibrium under the initial far-field stress has no effect on the temperature distribution.

6. CONCLUSIONS AND RECOMMENDATIONS

In this thesis, a poro-thermoelastic model for injection and extraction in a fractured rock is developed by combining the DDM, and the finite difference method. The fracture deformation is modeled by considering the nonlinear joint deformation and non-equilibrium under the initial in-situ stress. The mode has been applied to investigate pressure, temperature, fracture aperture and shear displacement for single and multiple fractures. Also, using the model, the distribution figure of pressure, temperature, normal and shear stresses in a reservoir are studied for different injection/extraction cases and fracture networks.

6.1 Conclusions

1. The fracture pressure and aperture increase by injection resulting in decreased amount of effective stress in the vicinity of injection point. In contrast, the fracture pressure and aperture decrease by extraction resulting in increased amount of effective stress in the vicinity of extraction point.

2. Since the thermoelastic effects cause significant tensile stress on the surfaces of fracture (rock shrinkage), it leads to large aperture and low fracture pressure compared to the isothermal condition.

3. Under equilibrium condition, the mechanical interaction of individual fractures in the network has a key role in causing shear displacements within the network. Normal displacement caused by injection or extraction generates shear

displacements on connected fracture segments. However, when the fracture segments are only parallel, this normal displacement cannot create any shear displacement. Therefore, the fracture geometry plays an important role in permeability evolution under injection/extraction.

4. A single fracture (divided in several elements) under non-equilibrium condition with an anisotropic in-situ stresses, there is a permanent shear slip due to the reduced amount of effective stress caused by constant injection under isothermal conditions. In cooling, the joint fully opens and this opening causes shear slip on all fracture elements at the same time. The failure modes are decided by Mohr-Coulomb failure criterion.

5. Under non-equilibrium condition, there is a quick pressure increase in the fracture because of the fluid compressibility (C_f). When the in-situ stresses compress the fracture, the pressure is increased and the fracture aperture is decreased. Also, the in-situ stress causes a significant pressure drop with decreasing fracture aperture in early time of simulation.

6. For cooling operations, if there is only flow into a single short fracture, the temperature spreads out evenly from the injection point (as a circle) because there is no convective transport in the matrix. However, with production, the temperature spreads out through the fracture channels by the flowing fluid.

6.2 Recommendations

In this thesis, single phase water injection or production is for two-dimensional case (unit height of 1 m). So, for future studies, the following topics are recommended.

- Hydraulic fracturing or propagation to naturally fractured reservoirs which have regular/irregular fracture network

- Two phases flow simulation (water and steam, water and gas or water and oil)

- 3-Dimensional simulation

NOMENCLATURE

$\Delta h \ (= 1\text{m})$	Unit height of fracture
$\Delta L \ (= 2\text{a})$	Length of fracture
c^T	Thermal diffusivity of intact porous rock
c_w	Heat capacity of fluid
$e \ (e_{kk})$	Strain (volumetric strain)
k_f	Fracture permeability
k_T	Thermal conductivity of fluid
p	Pore pressure
q_f	Flow rate in fracture
$q_{int} \ (= v_{int})$	Interface (leakoff) flow rate
$q_{h\text{-}int}$	Heat interface flow rate
$q_s \ (= q)$	Injection/production rate
r_w	Radius of well
t	Time
w_f	Fracture aperture
$A_{nn}^{ij}, A_{ns}^{ij}, A_{sn}^{ij}, A_{ss}^{ij}$	Boundary influencing coefficient in Section 2
A^{ij}, B^{ij}, C^{ij}	Influence coefficient for normal stress by normal and shear displacement discontinuity and fluid/interface flow rate
C_f	Fluid compressibility

$\overset{ij}{C_{ht}}, \overset{ij}{C_p}$	Fluid and heat coefficient matrix
D_n	Normal fracture displacement
$D_{n\,max}$	Maximum closure
D_s	Shear fracture displacement
$\overset{ij}{E}, \overset{ij}{F}, \overset{ij}{K}$	Influence coefficient for shear stress by normal and shear displacement discontinuity and fluid/interface flow rate
$F(x,y)$	A function with global coordinate positions
$\overline{F}(x,y)$	A function with local coordinate positions
G	Shear modulus
K_n	Normal stiffness
K_{ni}	Initial normal stiffness
K_s	Shear stiffness
$\overset{ij}{L}, \overset{ij}{H}, \overset{ij}{M}$	Influence coefficient for pore pressure by normal and shear displacement discontinuity and fluid/interface flow rate in Section 2.2
T	Temperature
α	Biot's coefficient
α_a	Angle of linear fracture from x-axis
α_f	Thermal expansion coefficient of pore fluid
α_s	Thermal expansion coefficient of solid
β	Angle from the x-axis segment (Counterclockwise)

ε_{ij}	Change of strain of the rock
$\overset{ij}{\gamma}$	$\overset{ij}{\gamma} = \dfrac{\pi}{2} + \beta_i - \beta_j$
ϕ	Matrix porosity
ϕ_f	Friction angle
ϕ_d	Dilation angle
$\rho_f \ (= \ \rho_w)$	Density of fluid
σ_n	Normal stress
$\sigma_s \ (= \tau)$	Shear stress
$\sigma_{xx}, \sigma_{yy}, \sigma_{xy}$	Stress
$\Delta\sigma'_{xx}$	Induced stress in x-direction
$\Delta\sigma'_{yy}$	Induced stress in y-direction
σ'_n	Effective normal stress
$\overset{i}{\sigma}_n, \overset{i}{\sigma}_s$	Total stress
$(\overset{i}{\sigma}_n)_0, (\overset{i}{\sigma}_s)_0$	Initial stress
$\overset{i}{\sigma'}_n, \overset{i}{\sigma'}_s$	Induced stress
$(\overset{i}{\sigma}_n)_0^\infty, (\overset{i}{\sigma}_s)_0^\infty$	Far-field stress
$(\overset{i}{\sigma'}_n)_0, (\overset{i}{\sigma'}_s)_0$	Initial induced stress
τ_ξ, τ_h	Time step

τ_p	Peak shear stress
τ_r	Residual shear stress
μ	Viscosity of fluid
υ	Poisson's ratio
υ_u	Undrained Poisson's ratio
δ_{ij}	Kronecker delta
ζ	Change of pore volume
$\overset{ij}{\sigma_n^{dn}}(t), \overset{ij}{\sigma_n^{ds}}(t), \overset{ij}{\sigma_n^{q}}(t), \overset{ij}{\sigma_n^{T}}(t)$	Influence coefficient for normal stress by normal and shear displacement discontinuity, fluid/interface flow rate and temperature in given time t in Section 2
$\overset{ij}{\sigma_s^{dn}}(t), \overset{ij}{\sigma_s^{ds}}(t), \overset{ij}{\sigma_s^{q}}(t), \overset{ij}{\sigma_s^{T}}(t)$	Influence coefficient for shear stress by normal and shear displacement discontinuity, fluid/interface flow rate and temperature in given time t in Section 2
$\overset{ij}{p^{dn}}(t), \overset{ij}{p^{ds}}(t), \overset{ij}{p^{q}}(t), \overset{ij}{p^{T}}(t)$	Influence coefficient for pore pressure by normal and shear displacement discontinuity, fluid/interface flow rate and temperature in given time t in Section 2
$\overset{ij}{T^{T}}(t)$	Influence coefficient for temperature by heat flux in Section 2

Over scripts

i, j	Index of fracture segment
ξ	Index of current time step
h	Index of time step

Super scripts

q	Fluid injection source and interface flow rate between fracture and matrix
d_n	Normal displacement discontinuity source
d_s	Shear displacement discontinuity source
T	Temperature source

REFERENCES

Asgian, M., 1988. A numerical study of fluid flow in deformable naturally fractured reservoirs. Ph.D. Dissertation, University of Minnesota, Minneapolis, MN.

Asgian, M., 1989. A numerical-model of fluid-flow in deformable naturally fractured rock masses. Int. J. Rock Mech. & Min. Sci. 26, 317-328.

Bandis, S.C., Lumsden, A.C., Barton, N.R., 1981. Experimental studies of scale effects on the shear behavior of rock joints. Int. J. Rock Mech. Miner. Sci. Geomech. Abstr. 18, 1-21.

Bandis, S.C., Lumsden, A.C., Barton, N.R., 1983. Fundamentals of rock joint deformation. Int. J. Rock Mech. Miner. Sci. Geomech. Abstr. 20, 249-268.

Biot, M.A., 1941. General theory of three-dimensional consolidation. J. Appl. Phys. 12, 155-164.

Carvalho, J.L., 1990. Poroelastic effects and influence of material interfaces on hydraulic fracturing. Ph.D. Dissertation, University of Toronto, Toronto.

Crouch, S.L., Starfield, A. M., 1983. Boundary Element Methods in Solid Mechanics. Unwin, New York, NY, USA.

Curran, J.H., Carvalho, J.L., 1987. A displacement discontinuity model for fluid-saturated porous media. In: Proceedings of the Sixth Congress of the ISRM, Montreal, Canada, pp. 73–78.

Ghassemi, A., Zhang, Q., 2004. A transient fictitious stress boundary element method for porothermoelastic media. J. Eng. Anal. Boundary Elements 28, 1363–1373.

Ghassemi, A., Zhang, Q., 2006. Poro-thermoelastic response of a stationary crack using the displacement discontinuity method. ASCE J. Eng. Mech. 132, 26-33.

Ghassemi, A., Tao, Q., 2010. Poro-thermoelastic borehole stress analysis for determination of the in-situ stress and rock strength. Geothermics 39, 250-259.

Goodman, R.E., 1976. Methods of Geological Engineering in Discontinuous Rocks. West Group, St. Paul, MN, USA.

Goodman, R.E., 1989. Introduction to Rock Mechanics, 2nd ed. John Wiley & Sons, New York, NY, USA.

Jaeger, J.C., Cook, N.G.W., Zimmerman, R.W., 2007. Fundamentals of Rock Mechanics, 4th ed. Blackwell Publishing, Malden, MA, USA.

Lee, J., Rollins, J., Spivey, J., 2003. Pressure Transient Testing. SPE Textbook Series Vol. 9, Richardson, TX, USA.

McTigue, D.F., 1986. Thermoelastic response of fluid-saturated porous rock. J. Geophys. Res. 91, 9533–9542.

McTigue, D.F., 1990. Flow to a heated borehole in porous, thermoelastic rock: Analysis. Water Resour. Res. 26, 1763-1774.

Rice, J.R., Cleary, M.P., 1976. Some basic stress diffusion solutions for fluid-saturated elastic porous media with compressible constituents. Rev. Geophys. 14, 227–241.

Swenson, D., Hardeman, B., 1997. The effects of thermal deformation on flow in a jointed geothermal reservoir. Int. J. Rock Mech. & Min. Sci. 34, 308-327

Tao, Q., 2010. Numerical modeling of fracture permeability change in naturally fractured reservoirs using a fully coupled displacement discontinuity method. Ph.D. Dissertation, Texas A&M University, College Station, TX.

Tao, Q., Ghassemi, A., 2010. Simulation of fluid flow in naturally fractured poro-thermoelastic reservoirs. In: Proceedings of the Thirty-fifth Stanford Workshop on Geothermal Reservoir Engineering, Stanford University, Stanford, CA, USA.

Tao, Q., Ghassemi, A., Ehlig-Economides, C.A., 2011. A fully coupled method to model fracture permeability change in naturally fractured reservoirs. Int. J. Rock Mech. & Min. Sci. 48, 259-268.

Van Golf-Racht, T.D., 1982. Fundamentals of Fractured Reservoir Engineering. Elsevier, Amsterdam, The Netherlands.

Warren, R.E., Root, P.J., 1963. The behavior of naturally fractured reservoirs. SPEJ 3, 245-255.

Witherspoon, P.A., Wang, J.S.Y., Iwai, K., Gale, J. E., 1980. Validity of cubic law for fluid flow in a deformable rock fracture. Water Resour. Res. 16, 1016-1024.

Zhou, X.X., Ghassemi, A., 2011. Three-dimensional poroelastic analysis of pressurized natural fracture. Int. J. Rock Mech. & Min. Sci. 48, 527-534.

APPENDIX A

MATRIX FOR FULLY COUPLED PORO-THERMOELASTICITY DDM

1. Matrix for pressure, leakoff flow rate, normal and shear displacement

$$
\begin{pmatrix}
1 & \overset{1,1}{\sigma_n^{dn}}+\overset{1}{K_n} & \overset{1,1}{\sigma_n^{ds}}+\overset{1}{K_n}\tan\phi_d & \overset{1,1}{\sigma_n^{q}} & \cdots & 0 & \overset{1,i}{\sigma_n^{dn}} & \overset{1,i}{\sigma_n^{ds}} & \overset{1,i}{\sigma_n^{q}} \\
0 & \overset{1,1}{\sigma_s^{dn}} & \overset{1,1}{\sigma_s^{ds}}-\overset{1}{K_s} & \overset{1,1}{\sigma_s^{q}} & \cdots & 0 & \overset{1,i}{\sigma_s^{dn}} & \overset{1,i}{\sigma_s^{ds}} & \overset{1,i}{\sigma_s^{q}} \\
-1 & \overset{1,1}{p^{dn}} & \overset{1,1}{p^{ds}} & \overset{1,1}{p^{q}} & \cdots & 0 & \overset{1,i}{p^{dn}} & \overset{1,i}{p^{ds}} & \overset{1,i}{p^{q}} \\
\overset{1,1}{C_p} & -2a & 0 & 2a & \cdots & \overset{1,i}{C_p} & 0 & 0 & 0 \\
\vdots & \vdots & \vdots & \vdots & \ddots & \vdots & \vdots & \vdots & \vdots \\
0 & \overset{i,1}{\sigma_n^{dn}} & \overset{i,1}{\sigma_n^{ds}} & \overset{i,1}{\sigma_n^{q}} & \cdots & 1 & \overset{i,i}{\sigma_n^{dn}}+\overset{i}{K_n} & \overset{i,i}{\sigma_n^{ds}}+\overset{i}{K_n}\tan\phi_d & \overset{i,i}{\sigma_n^{q}} \\
0 & \overset{i,1}{\sigma_s^{dn}} & \overset{i,1}{\sigma_s^{ds}} & \overset{i,1}{\sigma_s^{q}} & \cdots & 0 & \overset{i,i}{\sigma_s^{dn}} & \overset{i,i}{\sigma_s^{ds}}-\overset{i}{K_s} & \overset{i,i}{\sigma_s^{q}} \\
0 & \overset{i,1}{p^{dn}} & \overset{i,1}{p^{ds}} & \overset{i,1}{p^{q}} & \cdots & -1 & \overset{i,i}{p^{dn}} & \overset{i,i}{p^{ds}} & \overset{i,i}{p^{q}} \\
\overset{i,1}{C_p} & 0 & 0 & 0 & \cdots & \overset{i,i}{C_p} & -2a & 0 & 2a
\end{pmatrix}
\times
\begin{pmatrix}
\overset{1}{p(t)} \\
\Delta\overset{1\xi}{D_n} \\
\Delta\overset{1\xi}{D_s} \\
\Delta\overset{1\xi}{q}_{int} \\
\vdots \\
\\
\overset{i}{p(t)} \\
\Delta\overset{i\xi}{D_n} \\
\Delta\overset{i\xi}{D_s} \\
\Delta\overset{i\xi}{q}_{int}
\end{pmatrix}
=
\begin{pmatrix}
b\overset{1}{D_n} \\
b\overset{1}{D_s} \\
b\overset{1}{q}_{int} \\
b\overset{1}{p} \\
\vdots \\
\\
b\overset{i}{D_n} \\
b\overset{i}{D_s} \\
b\overset{i}{q}_{int} \\
b\overset{i}{p}
\end{pmatrix}
$$

$$
b\overset{i}{D_n} = -\sum_{h=0}^{\xi-1}\sum_{j=1}^{m}\overset{ij}{\sigma_n^{dn}}(t-\tau_h)\Delta\overset{jh}{D_n} - \sum_{h=0}^{\xi-1}\sum_{j=1}^{m}\overset{ij}{\sigma_n^{ds}}(t-\tau_h)\Delta\overset{jh}{D_s} - \sum_{h=0}^{\xi-1}\sum_{j=1}^{m}\overset{ij}{\sigma_n^{q}}(t-\tau_h)\Delta\overset{jh}{q}_{int}
$$

$$
-\sum_{h=0}^{\xi-1}\sum_{j=1}^{m}\overset{ij}{\sigma_n^{T}}(t-\tau_h)\Delta\overset{jh}{q}_{h-int} - \sum_{j=1}^{m}\overset{ij}{\sigma_n^{T}}(t-\tau_\xi)\Delta\overset{j\xi}{q}_{h-int}
$$

$$
b\overset{i}{D_s} = -\sum_{h=0}^{\xi-1}\sum_{j=1}^{m}\overset{ij}{\sigma_s^{dn}}(t-\tau_h)\Delta\overset{jh}{D_n} - \sum_{h=0}^{\xi-1}\sum_{j=1}^{m}\overset{ij}{\sigma_s^{ds}}(t-\tau_h)\Delta\overset{jh}{D_s} - \sum_{h=0}^{\xi-1}\sum_{j=1}^{m}\overset{ij}{\sigma_s^{q}}(t-\tau_h)\Delta\overset{jh}{q}_{int}
$$

$$
-\sum_{h=0}^{\xi-1}\sum_{j=1}^{m}\overset{ij}{\sigma_s^{T}}(t-\tau_h)\Delta\overset{jh}{q}_{h-int} - \sum_{j=1}^{m}\overset{ij}{\sigma_s^{T}}(t-\tau_\xi)\Delta\overset{j\xi}{q}_{h-int}
$$

$$
b\overset{i}{q}_{int} = -\sum_{h=0}^{\xi-1}\sum_{j=1}^{m}\overset{ij}{p^{dn}}(t-\tau_h)\Delta\overset{jh}{D_n} - \sum_{h=0}^{\xi-1}\sum_{j=1}^{m}\overset{ij}{p^{ds}}(t-\tau_h)\Delta\overset{jh}{D_s} - \sum_{h=0}^{\xi-1}\sum_{j=1}^{m}\overset{ij}{p^{q}}(t-\tau_h)\Delta\overset{jh}{q}_{int}
$$

$$
-\sum_{h=0}^{\xi-1}\sum_{j=1}^{m}\overset{ij}{p^{T}}(t-\tau_h)\Delta\overset{jh}{q}_{h-int} - \sum_{j=1}^{m}\overset{ij}{p^{T}}(t-\tau_\xi)\Delta\overset{j\xi}{q}_{h-int}
$$

$$
b\overset{i}{p} = 2w_f\overset{i}{a}c_f p(\tau_\xi) - 2a\sum_{h=0}^{\xi-1}\Delta\overset{ih}{q}_{int} - \sum_{h=0}^{\xi}\overset{ih}{q}_s
$$

2. Matrix for temperature and interface heat flow rate

$$
\begin{pmatrix}
-1 & \overset{1,1}{T^T} & \cdots & 0 & \overset{1,i}{T^T} \\
\overset{1,1}{C_{ht}} & \overset{1}{2a} & \cdots & \overset{1,i}{C_{ht}} & 0 \\
\vdots & \vdots & \ddots & \vdots & \vdots \\
0 & \overset{i,1}{T^T} & \cdots & -1 & \overset{i,i}{T^T} \\
\overset{i,1}{C_{ht}} & 0 & \cdots & \overset{i,i}{C_{ht}} & \overset{i}{2a}
\end{pmatrix}
\times
\begin{pmatrix}
\overset{1}{T}(t) \\
\overset{1\xi}{\Delta q}_{h-\text{int}} \\
\vdots \\
\overset{i}{T}(t) \\
\overset{i\xi}{\Delta q}_{h-\text{int}}
\end{pmatrix}
=
\begin{pmatrix}
\overset{1}{b\,T} \\
\overset{1}{b\,q}_{h-\text{int}} \\
\vdots \\
\overset{i}{b\,T} \\
\overset{i}{b\,q}_{h-\text{int}}
\end{pmatrix}
$$

$$
\overset{1}{b\,T} = -\overset{i}{T}_0 - \sum_{h=0}^{\xi-1}\sum_{j=1}^{m}\overset{ij}{T^T}\left(t-\tau_h\right)\overset{jh}{\Delta q}_{h-\text{int}}
$$

$$
\overset{i}{b\,q}_{h-\text{int}} = 2a\,w_f\,\rho_w c_w\,\overset{i}{T}(\tau_\xi) - 2a\sum_{h=0}^{\xi-1}\overset{ih}{\Delta q}_{h-\text{int}} + \sum_{h=0}^{\xi}\overset{ih}{q}_s
$$

APPENDIX B

FIELD POINTS MAP

1. Circle Fracture

- Circular fracture has 40 segments.
- Wells are locatied in the center of each segments.
- 100 Field points are located from 2R m to 1000R m.
- There are 40 far field lines in 360 °
- So, there are total 4000 field points.
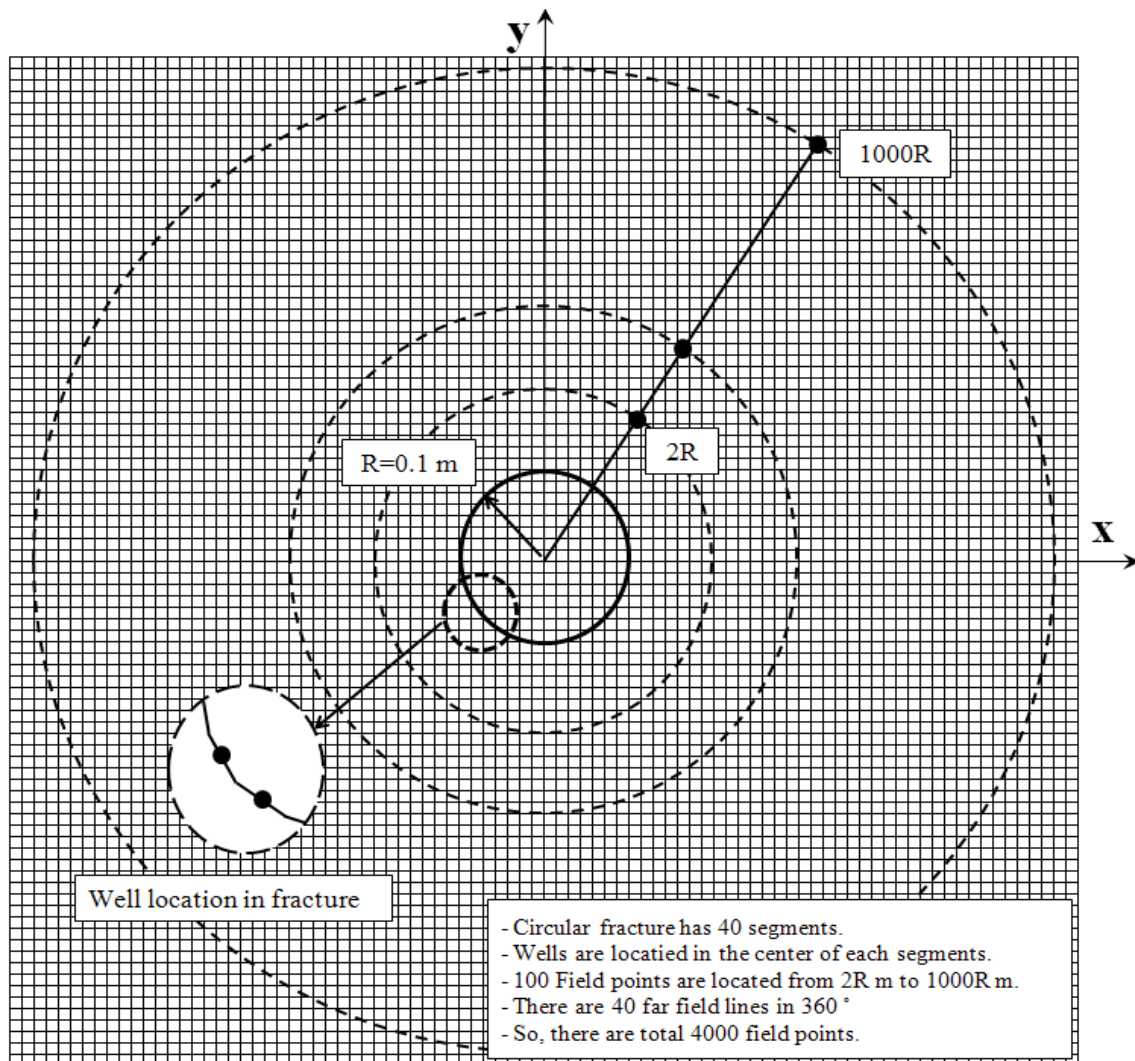
2. Angled Single Fracture

- Linear fracture has 40 segments.
- Injection wells are located at the center.
- Field points are located the center of every horizontal line.
- So, there are total 6241 (=79 × 79) points.

σ_{yy}

σ_{xx}

σ_{xx}

Injection Well

39m fracture

45°

0

σ_{yy}

Field Points
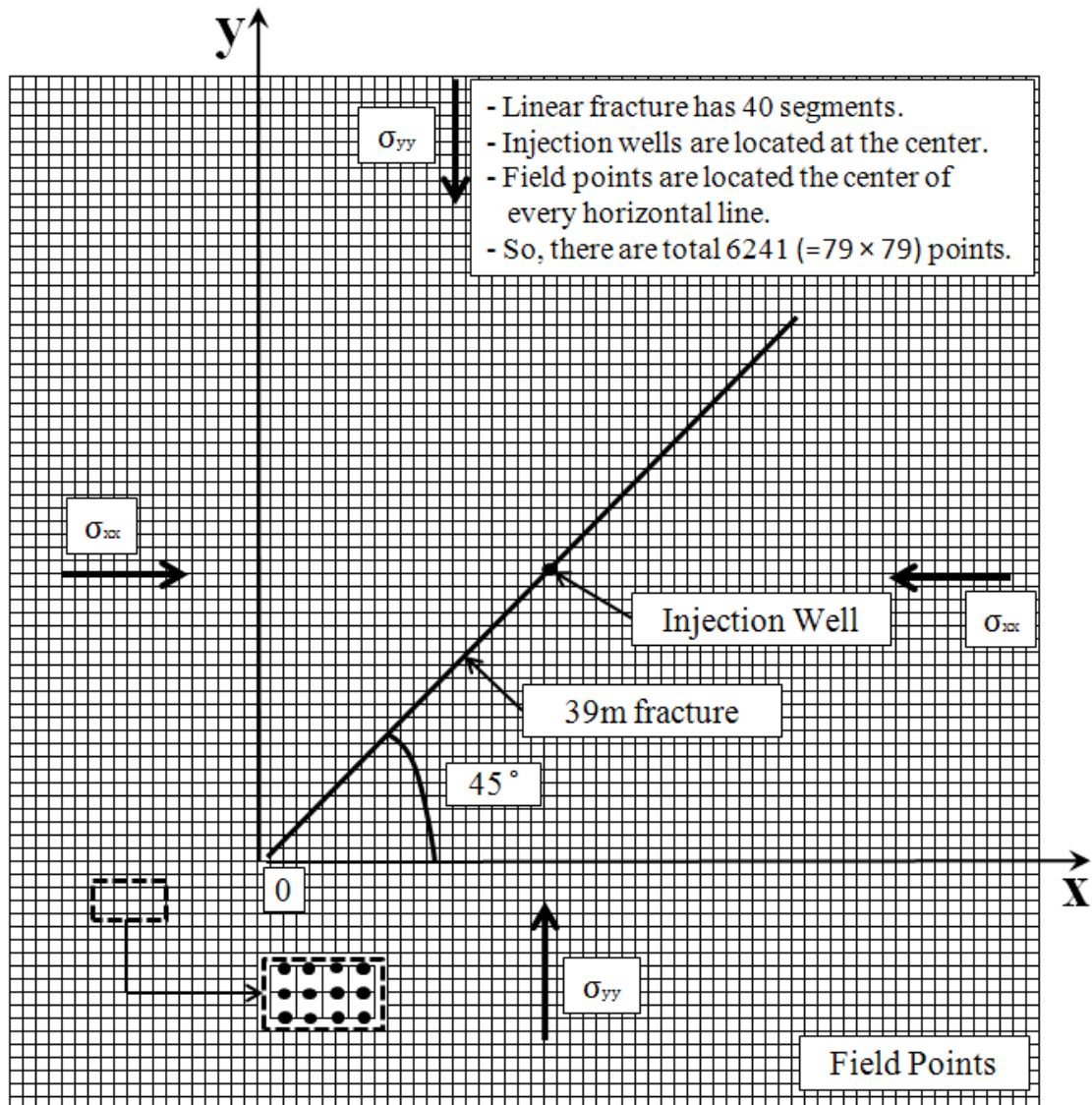
3. Horizontal Single Fracture

- Linear fracture has 30 segments.
- Injection well is located 1st segment and production well is located 30th segment.
- Field points are located the center of every horizontal line.
- So, there are total 2400 (=60 × 40) points.

4. Irregular Fracture Network

- Linear fracture has 111 segments.
- There are injection well and production well
- Field points are located the center of every horizontal line.
- So, there are total 3575(=65× 55) points.
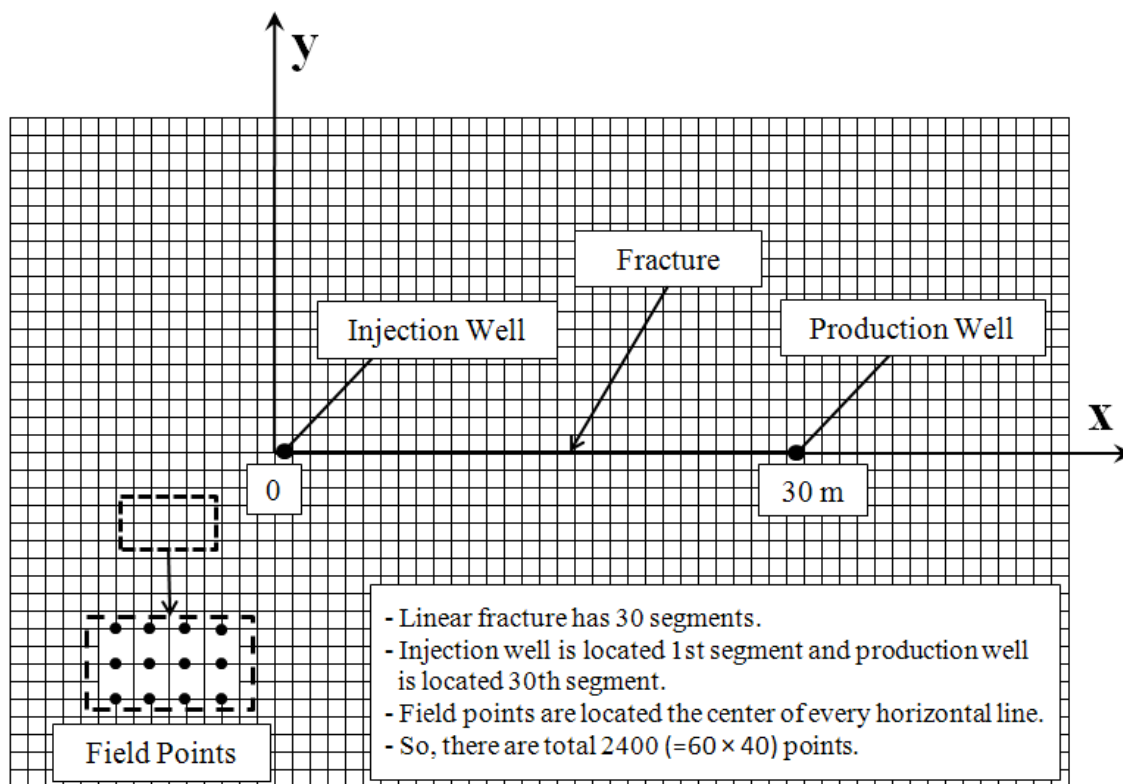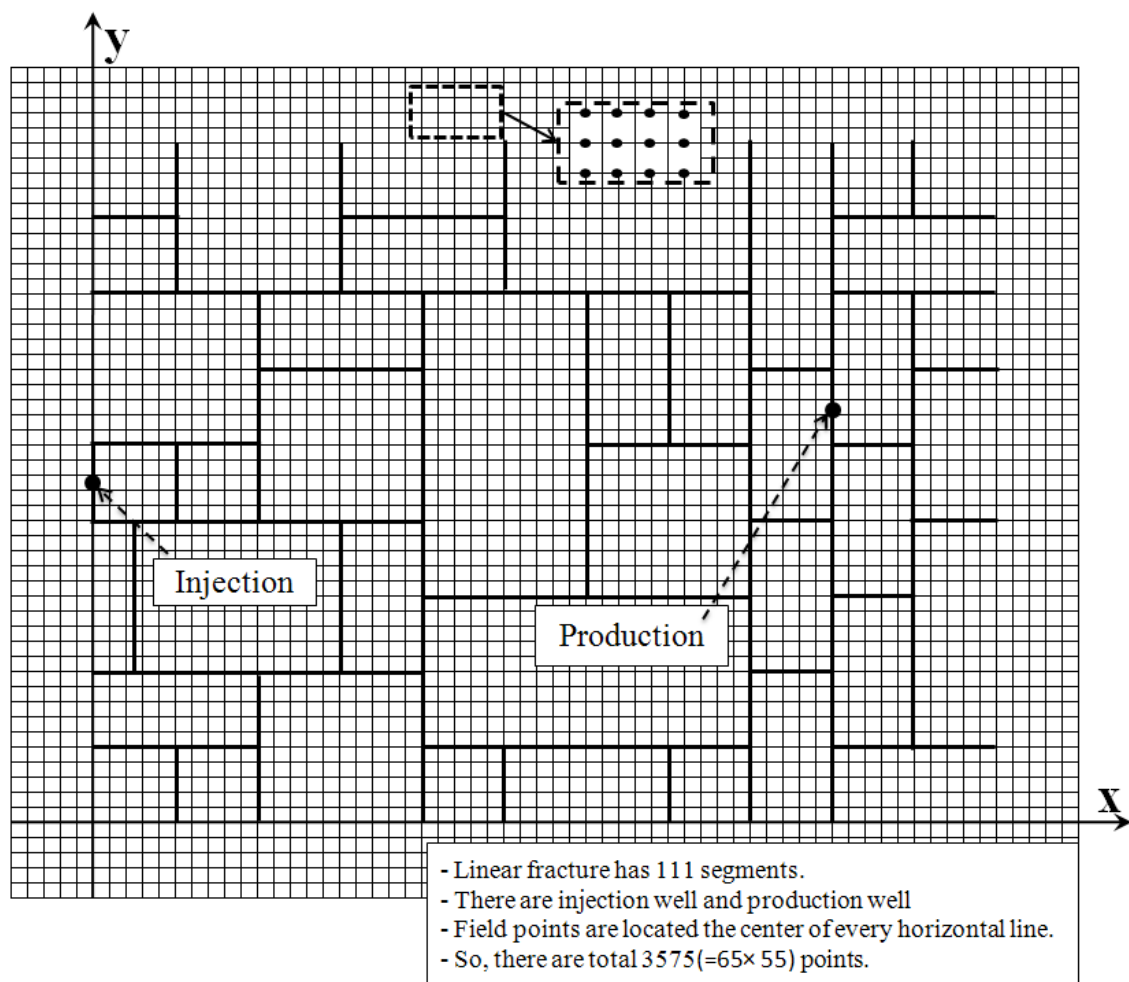
APPENDIX C

INDUCED PORE PRESSURE AND STRESS AROUND BOREHOLE
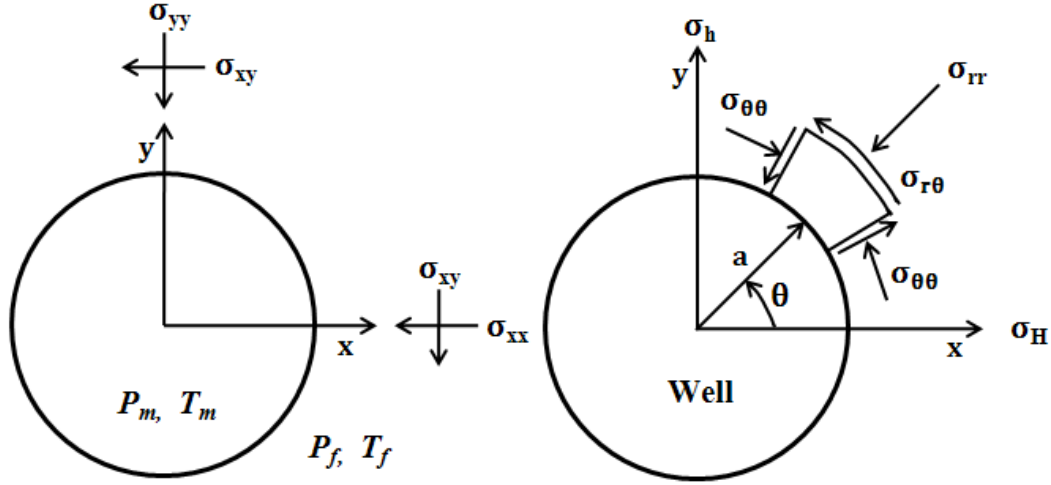
Pore Pressure

$$s\tilde{p} = p_f + \frac{c_{fT}}{1-c/c_T}(T_m - T_f)\left[\frac{K_0(\xi)}{K_0(\beta)} - \frac{K_0(\xi_T)}{K_0(\beta_T)}\right] + (p_m - p_f)\frac{K_0(\xi)}{K_0(\beta)}$$

$$+ \frac{C_1 B^2 (1-\upsilon)(1+\upsilon_u)^2 S_0 \cos 2\theta}{9(1-\upsilon_u)(\upsilon_u-\upsilon)} K_2(\xi) + \frac{C_2 B(1+\upsilon_u)S_0 \cos 2\theta}{3(1-\upsilon_u)}\frac{a^2}{r^2}$$

Radial Stress

$$s\tilde{\sigma}_{rr} = P_0 + 2\eta\left[(p_m - p_f) + \frac{c_{fT}}{1-c/c_T}(T_m - T_f)\right] \times \left[\frac{a^2}{r^2}\frac{K_1(\beta)}{\beta K_0(\beta)} - \frac{a}{r}\frac{K_0(\xi)}{\beta K_0(\beta)}\right]$$

$$+ 2\eta(T_m - T_f) \times \left[\frac{c_{fT}}{1-c/c_T} + \frac{K\alpha_m}{\alpha}\right]\left[\frac{a^2}{r^2}\frac{K_1(\beta_T)}{\beta_T K_0(\beta_T)} - \frac{a}{r}\frac{K_0(\xi_T)}{\beta_T K_0(\beta_T)}\right]$$

$$+ \frac{C_1 B(1+\upsilon_u)S_0 \cos 2\theta}{3(1-\upsilon_u)}\left[\frac{1}{\xi}K_1(\xi) + \frac{6}{\xi^2}K_2(\xi)\right] - \frac{C_2 S_0 \cos 2\theta}{1-\upsilon_u}\left(\frac{a}{r}\right)^2 - 3C_3 S_0 \cos 2\theta\left(\frac{a}{r}\right)^4$$

Tangential Stress

$$s\tilde{\sigma}_{\theta\theta} = -P_0\left(\frac{a}{r}\right)^2 + 2\eta\left[(p_m - p_f) + \frac{c_{fT}}{1 - c/c_T}(T_m - T_f)\right] \times \left[\frac{K_1(\beta)}{\beta K_0(\beta)}\left(\frac{a}{r}\right)^2 - \frac{K_1(\xi)}{\beta K_0(\beta)}\frac{a}{r} - \frac{K_0(\xi)}{K_0(\beta)}\right]$$

$$+ 2\eta(T_m - T_f) \times \left[\frac{c_{fT}}{1 - c/c_T} + \frac{K\alpha_m}{\alpha}\right]\left[-\frac{K_1(\beta_T)}{\beta_T K_0(\beta_T)}\left(\frac{a}{r}\right)^2 + \frac{K_1(\xi_T)}{\beta_T K_0(\beta_T)}\frac{a}{r} + \frac{K_0(\xi_T)}{K_0(\beta_T)}\right]$$

$$- \frac{C_1 B(1+\upsilon_u)S_0\cos 2\theta}{3(1-\upsilon_u)}\left[\frac{1}{\xi}K_1(\xi) + (1 + \frac{6}{\xi^2})K_2(\xi)\right] + 3C_3 S_0\cos 2\theta\left(\frac{a}{r}\right)^4$$

Shear Stress

$$s\tilde{\sigma}_{r\theta} = \frac{2C_1 B(1+\upsilon_u)S_0\cos 2\theta}{3(1-\upsilon_u)}\left[\frac{1}{\xi}K_1(\xi) + \frac{3K_2(\xi)}{\xi^2}\right] - \frac{C_2 S_0\cos 2\theta}{2(1-\upsilon_u)}\left(\frac{a}{r}\right)^2 - 3C_3 S_0\cos 2\theta\left(\frac{a}{r}\right)^4$$

K_0, K_1, K_2 are the second kind of Bessel functions with zero, one and two orders,

respectively.

$$\eta = \frac{\alpha(1-2\upsilon)}{2(1-\upsilon_u)}, \quad P_0 = \frac{\sigma_{xx} + \sigma_{yy}}{2}$$

$$S_0 = \frac{1}{2}\sqrt{(\sigma_{xx} - \sigma_{yy})^2 + 4\alpha_{xy}^2}, \quad \theta = \frac{1}{2}\tan^{-1}\left(\frac{2\sigma_{xy}}{\sigma_{xx} - \sigma_{yy}}\right)$$

$$\xi = r\sqrt{\frac{s}{c}}, \quad \beta = a\sqrt{\frac{s}{c}}, \quad \xi_T = r\sqrt{\frac{s}{c_T}}, \quad \beta_T = a\sqrt{\frac{s}{c_T}}$$

$$C_1 = -\frac{12\beta(1-\upsilon_u)(\upsilon_u-\upsilon)}{B(1+\upsilon_u)(D_2 - D_1)}, \quad C_2 = -\frac{4(1-\upsilon_u)D_2}{(D_2 - D_1)}, \quad C_3 = -\frac{\beta(D_2 + D_1) + 8(\upsilon_u-\upsilon)K_2(\beta)}{\beta(D_2 - D_1)}$$

$$D_1 = 2(\upsilon_u-\upsilon)K_1(\beta), \quad D_2 = \beta(1-\upsilon)K_2(\beta)$$

To prevent nomenclature confusion with main article, the nomenclatures listed

below in this Appendix C are only for this appendix and Section 4.1.

s is Laplace variable, over script '~' is Laplace space, a is borehole radius, r is the radial distance to the center of borehole, c_{fT} is the coupled thermal-fluid pressure coefficient, c is cohesion, c_T is the thermal diffusivity, c_f is the fluid diffusivity, T_m, T_f are the temperature of mud and formation, p_m, p_f are the pressure of mud and formation, B is the Skempton pore pressure coefficient, S_0 is the deviatoric stress, υ, υ_u are Poisson's ratio in drained and undrained, α is the Biot's coefficient. All equations and figures are from Ghassemi and Tao (2010).

APPENDIX D

FLOW CHART

Start

1. Import Input
Parameters
(Rock Properties
/ Initial values)

2. Set up the shape of the fracture
(If there were field points, set field points)

3. Set in situ stress σ_{xx}, σ_{yy} and σ_{xy}
4. Initialize the pore pressure and set stresses
   (σ_n and σ_s caused by in situ stresses)

5. Set normal stiffness (K_n) and normal displacement (D_n) by two options

5.1. Using initial normal stiffness (K_{ni}), maximum closure ($D_{n\,max}$),
   and effective stress (σ'_n), set above values using below equation
   ($K_n = \dfrac{K_{ni}}{[1-\frac{\sigma'_n}{K_{ni}D_{n\,max}+\sigma'_n}]^2}$) (Nonlinear)
5.2. Set K_n, D_n by inputs (Linear)

6. Set injection/ extraction rate
(The flow rates could be set differently by time step)

7. Find temperature (T) and heat flux ($q_{h\text{-}int}$) using DDM

8. Solving Part: Find ΔD_n, pressure (p), shear displacement (ΔD_s) and leakoff rate (Δv_{int}) using DDM

Iteration>100
& Temperature
difference $<10^{-4}$

No

Yes

9. Update D_n, σ'_n and σ_s

10. Check failure mode in single fracture case: Find $\sigma_{s\,max}$ and if $\sigma_s > \sigma_{s\,max}$, σ_s is same with the σ_s in previous time step (It means K_s is '0'. $\sigma_{s\,max} = \sigma'_n \times \tan(\emptyset_f + \emptyset_d) + C$, where $\emptyset_f$: Frictional angle, $\emptyset_d$: Dilation angle and C: Cohesive)

11. Update p, T, D_s, v_{int}, fracture permeability (K) and other relative values

Is there field point calculation?   (III: Number of field points)

Yes

No

Iteratin $= \sqrt{III}$?

Yes

No

End

VITA

Name: Byungtark Lee

Address: Harold Vance Department of Petroleum Engineering, 3116 TAMU,
College Station, TX 77843-3116

Email Address: kfclbt@gmail.com

Education: Korea Aerospace University,
Goyang, South Korea
B.S., Mechanical Engineering,
February 2004

Texas A&M University,
College Station, Texas,
M.S., Petroleum Engineering,
June 2011

Affiliation: Society of Petroleum Engineers
American Rock Mechanics Association